STUDY OF BIT-PATTERNED FePt MEDIA FOR HIGH DENSITY MAGNETIC RECORDING

SHREYA KUNDU

NATIONAL UNIVERSITY OF SINGAPORE

2014

STUDY OF BIT-PATTERNED FePt MEDIA FOR HIGH DENSITY MAGNETIC RECORDING

SHREYA KUNDU
B.Sc Electronics (Hons), University of Delhi, India

A THESIS SUBMITTED FOR THE DEGREE OF DOCTOR OF PHILOSOPHY

DEPARTMENT OF ELECTRICAL AND COMPUTER ENGINEERING

NATIONAL UNIVERSITY OF SINGAPORE

JANUARY 2014

Declaration

I hereby declare that this thesis is my original work and it has been written by me in its entirety. I have duly acknowledged all the sources of information which have been used in the thesis.

This thesis has also not been submitted for any degree in any university previously.

Shreya Kundu

Shreya Kundu

17 January 2014

Acknowledgements

First of all, I would like to express my sincere gratitude to my advisors and mentors Prof. Charanjit. S. Bhatia, Dr. M. S. M Saifullah and Assoc. Prof. Hyunsoo Yang for their guidance and encouragement during these four years of the Ph. D. program. I was very fortunate to have this opportunity to carry out my PhD research under their supervision at National University of Singapore (NUS). I learnt a lot in every aspect of my academic life from their comments during our fruitful discussions.

I would like to express my gratitude to all my past and present colleagues and friends in the Spin and Energy laboratory (SEL) of NUS for their valuable help and friendship. I wouldn’t have cherished research so much if it had not been for this cheerful group of people. A token of thanks is due to Mr. Jung Yoon Yong Robert, our previous laboratory officer, for all his help with the experimental facilities at SEL. I would also like to share this moment with my batch mates – Mridul and Siddharth – with whom I began this journey.

This work was supported by National Research Foundation Grant NRF-CRP 4-2008-06 and the NUS research scholarship offered in collaboration with the Nanocore programme (WBS No. C-003-263-222-532). Thanks are due to the academic and research staff at the Department of Electrical and Computer Engineering, NUS and Institute of Materials Research and Engineering (IMRE), Singapore, for their valuable discussions and support. The experimental facilities provided by IMRE to carry out the research work is greatly appreciated. To Dr. Ramakrishnan Ganesan at IMRE, thank you for those long hours of discussion over tea and snacks.

Lastly, I would like to thank all my friends in Singapore, especially Rishita, Divya, Prachi and Shilpi, for being there for me through thick and thin. To my parents, grandparents and my angelic younger sister, Shirsha, thank you for the constant support, patience and love during the last four years. Above all, I thank God for giving me the strength to fulfil this mammoth goal of carrying out research and presenting it as ‘my thesis’ in the area of my interest.

The Ph.D. thesis would not have been possible without the contribution and support of many others during the last four years. I will like to take this opportunity to thank all of them wholeheartedly.

Cheers!

Shreya Kundu

Abstract

With the magnetic media in hard disk drives (HDDs) moving towards its next goal of >1 Tb/in^2, the material requirements and implementation of new recording schemes to achieve such high densities are undoubtedly challenging. Heat-assisted magnetic recording (HAMR) – a potential contender to extend the areal density further – necessitates the use of high anisotropy materials such as $L1_0$ FePt to fabricate thermally stable grains of dimensions ~3-4 nm. On the other hand, in bit patterned media (BPM), the conventional granular recording layer used in current HDDs is replaced by an array of well-isolated magnetic islands. In this thesis, novel techniques to achieve thermally stable grains for HAMR and to fabricate BPM are presented and investigated.

Spacer materials are often used to fabricate granular $L1_0$ FePt media and reduce the grain size, though at the expense of reduced out-of-plane coercivity. We demonstrate and examine a spacer-less method in which adding a small amount of helium (0.5-1% by volume) to argon sputtering gas leads to a substantial improvement in the chemical ordering, as well as in the magnetic and microstructural properties of FePt. This change is attributed to the modification in the ion current density of the plasma caused by the excited metastable helium species. Helium plays a pivotal role in providing the Fe and Pt atoms with optimal adatom mobility, thereby producing well-ordered $L1_0$ FePt media. Enhancements of up to ~46% in the out-of-plane coercivity and exchange decoupled grains exhibiting a twofold reduction in their size are achieved.

One of the challenges associated with BPM technology is the fly height modulation. As a result, an additional process step of surface planarization after BPM fabrication is essential. Irradiating the recording layer with energetic ion species to destroy its magnetic properties at selected locations is a promising way to circumvent planarization. Previously, high energy implantation with ion energies reaching up to several keV was used in $L1_0$ FePt to create an array of alternate magnetic (bits) and non-magnetic regions. Although magnetic isolation between the bits was achieved, a phase transformation from $L1_0$ to $A1$ was observed in the magnetic regions. Lateral straggle of the ions into the bit region was accountable for this outcome. Here, a careful study of C^+ ion embedment in $L1_0$ FePt media was carried out to demonstrate that the magnetic properties of FePt can be damaged by using ion energy values of a few hundred eV. This is a significant result since the use of lower ion energies ensures reduced lateral straggle. Basic facets of ion beam mixing such as the relative size of the incident C^+ ions with regard to the media's lattice constant and the presence of channeling in $L1_0$ FePt enabled the realization of $L1_0$ FePt-based BPM at lower ion energies.

The thesis also focuses on the patterning of high density nanostructures atop media surfaces to act as masks for BPM fabrication. Self-assembly of block copolymers has been identified as a potential candidate to achieve this goal. However, the factors affecting its reliability and reproducibility as a patterning technique on various kinds of surfaces are not well-established. Studies pertaining to block copolymer self-assembly have been confined to ultra-flat substrates, without taking into consideration the effect of surface roughness. Here, we showed that a slight change in the angstrom-scale roughness arising from the microstructure at the media surface created a profound effect on the self-assembly of the polystyrene-polydimethylsiloxane (PS-*b*-PDMS) block copolymer. Its self-assembly was found to be dependent on both the root mean square roughness (R_{rms}) of the surface as well as the type of solvent annealing system used. It was observed that surfaces with R_{rms} <5.0 Å showed self-assembly. The surface roughness posed a kinetic barrier to the movement of the block copolymer. The blocks ceased to phase separate, leading to their conformation to the surface.

Properties of the magnetic media crucial for data storage at recording densities beyond 1Tb/in^2 have been studied. This enabled the envisaging of a novel scheme to achieve FePt-based BPM by creating alternate magnetic and non-magnetic regions using large area self-assembly and low energy ion bombardment.

Table of Contents

List of Figures

List of Tables

List of Symbols and Abbreviations

A	Area
AFC	Anti-ferromagnetically coupled
AFM	Atomic force microscopy
$\vec{\mathbf{B}}$	Magnetic flux density
BPM	Bit patterned magnetic media
cm	Centimeters
D	Dose (charge per unit area)
d	Spacing between two crystal planes
$\mathbf{E_d}$	Threshold displacement energy of the host atom
$\widehat{\mathbf{E_e}}$	average energy lost due to electron excitation during collision cascade
$\mathbf{E_{ex}}$	Exchange interaction
$\mathbf{E_i}$	Energy from the incident atoms transferred as translatory motion to the host atoms in the lattice
$\mathbf{E_t}$	Maximum energy transferred to the host atom
EA	Easy axis
EAMR	Energy assisted magnetic recording
EBL	Electron beam lithography
ECC	Exchange coupled composite media
EELS	Electron energy loss spectroscopy
emu	Electromagnetic unit
EUV	Extreme ultra-violet lithography
eV	Electron volt

fcc	Face centered cubic
fct	Face centered tetragonal
FCVA	Filtered cathodic vacuum arc
FE-SEM	Field emission-scanning electron microscopy
FHM	Fly height modulation
Gb	Gigabyte
$\vec{\mathbf{H}}$	Magnetic field strength
h	Planck’s constant
$\mathbf{H_c}$	Coercivity
$\vec{\mathbf{H}}_\mathbf{d}$	Demagnetization field
$\mathbf{H_k}$	Anisotropy field
$\mathbf{H_n}$	Nucleation field
HA	Hard axis
HAADF−STEM	High angle angular dark field−scanning transmission electron microscopy
HAMR	Heat assisted magnetic recording
HDD	Hard disk drive
HSQ	Hydrogen silsesquioxane
in	Inch
$\vec{\mathbf{J}}$	Total angular momentum
$\mathbf{J_{ij}}$	Exchange constant
$\vec{\mathbf{J}}(\vec{\mathbf{r}}')$	Current density at a location $\mathbf{r}'$
$\mathbf{K_b}$	Boltzmann constant
$\mathbf{K_u}$	Magnetocrystalline anisotropy constant

kb	Kilobyte
kg/mol	Kilogram per mole
$\vec{\mathbf{L}}$	Orbital angular momentum
LMR	Longitudinal magnetic recording
$\vec{\mathbf{M}}$	Magnetization
M	Mass of the atom/embedding ion species
$\vec{\mathbf{m}}$	Magnetic moment
$\mathbf{M_r}$	Remanent Magnetization
$\mathbf{M_s}$	Saturation Magnetization
Mb	Megabyte
MAMR	Microwave assisted magnetic recording
MFM	Magnetic force microscopy
MPa	Mega Pascal
N	Demagnetization tensor
$\mathbf{N_d}$	Number of host atoms displaced
nm	Nanometers
NIL	Nanoimprint lithography
PMR	Perpendicular magnetic recording
PS-*b*-PDMS	polystyrene-polydimethylsiloxane
R	Universal gas constant
r	Rate of reaction in Van’t Hoff-Arrhenius-Eyring equation
$\mathbf{R_{element}}$	Atomic radius of the element
$\mathbf{R_{rms}}$	Root mean square surface roughness
$\mathbf{R_t}$	Peak-to-peak mean roughness depth

$\mathbf{r_{element}}$	Probability of a particular lattice site being occupied by the correct atom
$\mathbf{r_{int}}$	Radius of the interstitial site
RAMAC	Random access method of accounting and control
rpm	Revolutions per minute
$\vec{\mathbf{S}}$	Spin angular momentum
S	Ordering parameter
$\mathbf{S^r}$	Remanance squareness
$\mathbf{S^*}$	Coercivity squareness
SAED	Selected area electron diffraction
sccm	Standard cubic centimeters per minute
SNR	Signal to noise ratio
SRIM	Stopping range of ion in matter
SUL	Soft underlayer
SRIM	Stopping range of ion in matter
T	Temperature in Kelvin
Tb	Terabyte
TEM	Transmission electron microscopy
THF	Tetrahydrofuran
ToF-SIMS	Time of flight secondary ion mass spectroscopy
TRIM	Transport of ion in matter
UHV	Ultra-high vacuum
V	Volume
VSM	Vibrating sample magnetometer

W	Watts
$\mathbf{X_{element}}$	Mole fraction of an element
XRD	X-ray diffraction
$\mathbf{\Delta A}$	Change in area
$\mathbf{\Delta E_R}$	Activation energy required by the polymer chains to diffuse over rough surface
$\mathbf{\Delta G_{SA}}$	Gibbs free energy
$\mathbf{\Delta H_{SA}}$	Enthalpy change
$\mathbf{\Delta S_{SA}}$	Entropy change
$\mathbf{\Delta t}$	Time duration
$\boldsymbol{\kappa}$	Displacement efficiency factor of an atom from its lattice site
$\boldsymbol{\lambda}$	wavelength
$\boldsymbol{\mu_0}$	Permeability of free space
µm	Micron
$\boldsymbol{\vartheta_0}$	Pre-exponential factor in Van’t Hoff-Arrhenius-Eyring equation
Å	Angstroms

List of Publications, Conferences and Patents

Publications in Peer-reviewed journals

(A) Related to thesis

1. **S. Kundu**, E. Rismani-Yazdi, M. S. M. Saifullah, H. R. Tan, H. Yang, and C. S. Bhatia, "Low energy C^+ ion embedment induced structural disorder in $L1_0$ FePt", *Journal of Applied Physics,* **115**, 013907 (2014).

   Contribution: The experiment was designed by S. Kundu after discussion with the supervisors. The TRIM simulations, deposition of $L1_0$ FePt magnetic films, TEM sample preparation, magnetic measurements, and theoretical analysis of the experimental observations were carried out by S. Kundu. The manuscript was also written by her.

2. **S. Kundu**, N. Gaur, S. N. Piramanayagam, S. L. Maurer, H. Yang and C. S. Bhatia, "Ion Implantation Challenges for Patterned Media at Areal Densities over 5 Tbpsi" (Invited Paper), The Magnetic Recording Conference (TMRC), Aug 20-22, *IEEE Transactions on magnetics,* **50**, 3200206 (2014).

   Contribution: The TRIM simulations for lateral straggle, deposition of $L1_0$ FePt magnetic films, magnetic measurements, and analysis of the experimental data were carried out by S. Kundu. The manuscript was also written by her.

3. N. Gaur, **S. Kundu**, S. N. Piramanayagam, S. L. Maurer, H. K. Tan, S. K. Wong, S. E. Steen, H. Yang and C. S. Bhatia, "Lateral atomic movement induced order-disorder phase transition in $L1_0$ FePt thin films by ion implantation", *Scientific Reports,* **03**, 1907, (2013).

   Contribution: Deposition of the $L1_0$ FePt magnetic films, magnetic measurements, and analysis of the electron diffraction patterns obtained from TEM were carried out by S. Kundu

4. **S. Kundu**, N. Gaur, M. S. M. Saifullah, H. Yang and C.S. Bhatia, “Spacer-less, decoupled granular $L1_0$ FePt magnetic media using Ar−He sputtering gas”, *Journal of Applied Physics*, **112**, 113916, (2012).

   Contribution: The experiment was designed by S. Kundu after discussion with the supervisors. The deposition of $L1_0$ FePt magnetic films, TEM sample preparation, magnetic measurements, analysis of the experimental observations, and grain size calculations were carried out by S. Kundu. The manuscript was also written by her.

5. **S. Kundu**, R. Ganesan, N. Gaur, M. S. M. Saifullah, H. Hussain, H. Yang and C. S. Bhatia, “Effect of angstrom-scale surface roughness on the self-assembly of polystyrene-b-polydimethylsiloxane block copolymer”, *Scientific Reports* **2** (Nature), 617, (2012).

   Contribution: The experiment was designed by S. Kundu after discussion with the supervisors. Fabrication of the different magnetic media, self-assembly of PS-b-PDMS, AFM, SEM, and Fast Fourier transforms were carried out by S. Kundu. The manuscript was also written by her after detailed analysis of the experimental results.

(B) Others

6. J. Son, **S. Kundu**, L. K. Verma, M. Sakhuja, A. J. Danner, C. S. Bhatia and H. Yang, “A practical superhydrophilic self-cleaning and antireflective surface for outdoor photovoltaic applications”, *Solar Energy Materials and Solar Cells*, **98**, 46, (2012).

   Contribution: The FDTS treatment of the patterned surfaces was carried out by S. Kundu.

7. **S. Kundu**, S. H. Lim, R. Ganesan, M. S. M. Saifullah, H. Hussain, H. Yang and C. S. Bhatia, “Tunable daughter molds from a single Si master mold” (manuscript submitted to JVST B).

   Contribution: The experiment was designed by S. Kundu after discussion with supervisor in IMRE – Dr. M. S. M. Saifullah. Imprinting of substrates, dry chemical etching, and SEM were carried out by S. Kundu. The manuscript was also written by her.

Conferences

1. **S. Kundu**, E. Rismani-Yazdi, M. S. M. Saifullah, H. Yang, and C. S. Bhatia, "Low energy C^+ ion embedment in $L1_0$ FePt – for BPM fabrication at areal densities ≥2 Tb/in^2", presented at International Magnetics conference (INTERMAG), 2014. (Oral Presentation)

2. **S. Kundu**, E. Rismani-Yazdi, M. S. M. Saifullah, N. Satyanarayana, H. Yang, and C. S. Bhatia, "Influence of carbon embedding on the magnetic properties of $L1_0$ FePt magnetic media", presented at Metal multilayer conference (MML), May 19-24, 2013 in Kyoto, Japan. (Poster)

3. **S. Kundu**, R. Ganesan, N. Gaur, M. S. M. Saifullah, H. Hussain, H. Yang and C. S. Bhatia, "Effect of angstrom-scale surface roughness on the self-assembly of a block copolymer for patterned media fabrication", presented at International Conference of Young Researchers on Advanced Materials (ICYRAM), July 1-6, 2012 in Singapore. (Poster)

4. **S. Kundu**, R. Ganesan, N. Gaur, M. S. M. Saifullah, H. Hussain, H. Yang and C. S. Bhatia "Effect of angstrom-scale surface roughness on the self-assembly of polystyrene-b-polydimethylsiloxane", presented at International Magnetics conference (INTERMAG), May 7-11, 2012 in Vancouver, Canada. (Poster)

5. **S. Kundu**, S. H. Lim, R. Ganesan, C. S. Bhatia, H. Y. Low and M. S. M. Saifullah, "Direct nanoimprint lithography of Si molds", presented at International Conference on Materials for Advanced Technologies (ICMAT), June 26-July 1, 2011 in Singapore. (Poster)

Contribution in other conferences

1. C. S. Bhatia, E. Rismani-Yazdi, **S. Kundu**, "Frontiers in magnetic recording: vision for 10 Tb/in^2", presented at XVII International Workshop on the Physics of Semiconductor Devices (IWPSD), December 10-13, 2013 in Noida, India. (Invited talk)
2. C. S. Bhatia, E. Rismani-Yazdi, M. A. Samad, **S. Kundu**, R. J. Yeo and N. Satyanarayana, "Surface treatment with a few atomic layers of carbon to improve tribological properties of magnetic hard disk media", presented at International Conference on Diamond and Carbon Materials (ICDCM), September 2-5, 2013 in Riva Del Garda, Italy. (Invited talk)
3. S. N. Piramanayagam, N. Gaur, **S. Kundu**, S. L. Maurer, H. Yang and C. S. Bhatia, "Ion implantation challenges for patterned media at areal densities over 5 Tbpsi", presented at The Magnetic Recording Conference (TMRC), August 20-22, 2013 in Tokyo, Japan. (Invited talk)

Invention Disclosure

C. S. Bhatia, **S. Kundu**, M. S. M. Saifullah, H. Yang, and M. Asbahi, **Fabricating Bit Pattern Media (BPM) for areal density 1Tb/in^2 for magnetic data storage systems**, provisional application filed with US Patent & Trade Marks Office, ILO Ref: 13397N (2014).

Miscellaneous

1. Won the postgraduate oral presentation competition organized by Institute of Materials Research & Engineering (IMRE), Singapore, October 3-4, 2013. Presentation topic: "Spacer-less, decoupled granular $L1_0$ FePt magnetic media using Ar−He sputtering gas"
2. Attended the IEEE summer school in Assisi, Italy from June 9-14, 2013.
3. CAP attained in NUS examinations: 4.58/5

CHAPTER 1

Introduction

1.1 An introduction to hard disk drives (HDD)

Originally proposed by Oberlin Smith in 1878, the principles of magnetic audio recording were put together by Valdemar Poulsen in 1898 to design a hard steel wire media which could be magnetized and demagnetized continuously along its length and was termed as the ‘Telegraphone’ [1]. Since then, magnetic storage has come a long way from recording analog signals to digital data and revolutionized the non-volatile information storage technology. In 1956, a major development occurred in this field in the form of IBM’s random access method of accounting and control (RAMAC) hard disk drive [2], which stored 5 megabytes (Mb) of data at an areal density of 2 kb/in^2. Initially aimed at real time accounting, HDDs have now become a dominant medium for secondary data storage. Easy portability, high areal density, lowest cost per byte compared to other memory devices, and reasonable access times have made it widely popular for use in personal computers, video recorders and game consoles among other consumer electronics.

An important parameter in hard disk drives has been its areal density. Since its introduction, there have been numerous studies on improving the bit packing density of the magnetic storage medium. Longitudinal recording paved the way for perpendicular magnetic recording (PMR) in 2006 and, from then onwards, areal density has grown at a rate of 40% annually [3]. With perpendicular recording technology, a maximum areal density of 600 Gb/in^2

has been demonstrated [4]. As the magnetic data storage industry is now moving towards its next goal of 1 Tb/in^2 and beyond, the bit size needs to shrink further to 12 × 12 nm^2 and below [5]. A bit comprises several magnetic grains. Given that in conventional recording media, the signal to noise ratio (SNR) is proportional to the logarithm of number of grains in a bit [6], it is essential that the number of grains representing a bit should be large to ensure a high SNR. However, the scaling down of the grain size has been restricted by the onset of superparamagnetism – a phenomenon in which a magnetic particle has zero coercivity and remanence, causing loss of information. The perpendicular recording technology is on a downtrack due to the emergence of a combination of limits – the magnetic trilemma [7]. The trilemma comprises SNR, thermal stability and writability issues. To attain high thermal stability, either the size or the magneto-crystalline anisotropy of the grain should be large. For better writability, smaller anisotropy is desirable but for high signal to noise ratio, the grain size should be as small as possible. To overcome the recording trilemma, several recording techniques have been proposed and are currently being studied.

1.2 Challenges

First, among the alternative scheme of technologies, is exchange coupled composite (ECC) media. The concept of having a magnetic grain comprising low and high anisotropy regions was suggested by Victora *et al.* in 2005 [8]. The soft (low anisotropy) region switches easily under the application of the available write field and enables the reversal of the hard (high anisotropy) region through exchange interaction. Therefore, although smaller grains and reasonable write field values are used, yet the thermal stability of the storage medium is not compromised. ECC combined with the current PMR technology has been proposed to extend the areal density up to ~1 Tb/in^2 [9].

For areal density growth beyond 1 Tb/in^2, energy-assisted magnetic recording techniques, i.e., microwave-assisted magnetic recording (MAMR) and heat-assisted magnetic recording (HAMR), are being extensively investigated. In MAMR, the write field assisted by another magnetic field of a few kOe which is oscillating at a frequency in the microwave range is used for switching the easy axis of magnetization in the recording media [10]. On the other hand, in HAMR, a laser is used for localized heating of a spot in the magnetic media to Curie temperature such that the coercivity of the spot is reduced [11]. An external field is applied concurrently and the desired bit is recorded. These energy-assisted recording schemes enable the usage of high anisotropy materials like $L1_0$ phase FePt, MnAl and CoPt [12].

Another interesting approach to circumvent superparamagnetism is to eliminate the notion of representing one bit by many magnetic grains. Instead, bit patterned media (BPM), comprising lithographically designed magnetic islands each depicting a bit, has been suggested [13]. Since the volume of each magnetic bit is larger than the volume of individual grains in conventional PMR media, the issue of thermal instability can be prevented.

These methods provide attractive solutions to overcome the bottleneck posed by the magnetic trilemma in the current PMR technology. However, their implementation in HDDs is challenging. For example, in MAMR, the inclusion of a high frequency source in the write head, matching the resonant frequency of the media material (~20-40 GHz), is required [10]. Similarly, integration of the laser source with the write head is of concern in HAMR [12]. Tuning the properties of high anisotropy magnetic material for practical application in HDDs is necessary. Lithography techniques which promise to be inexpensive and provide high-throughput for patterning high density nanostructures (of dimensions <12 nm) are required in BPM.

A number of such issues associated with the next-generation, high anisotropy $L1_0$ FePt media have been identified. A recording scheme that harnesses the advantages provided by $L1_0$ FePt and self-assembly (a high density and relatively faster patterning technique) [13] for creating BPM approaching areal densities ≥4 Tb/in^2 has been visualized. This thesis presents and addresses the problem statements associated with these goals.

1.3 Research Objectives

- **Smaller $L1_0$ FePt magnetic grains without the addition of ternary elements:** It will be ideal to achieve well-ordered, granular and smaller-sized FePt grains that exhibit high out-of-plane coercivity, all simultaneously. However, literature has shown that the addition of spacer materials such as SiO_2 and TiO_2, among others, is necessary to obtain smaller grains of dimensions ~3-4 nm [14, 15]. However, the inclusion of such materials interferes with the magnetocrystalline anisotropy of FePt, leading to reduced coercivity – which is not desirable for HAMR applications. One promising method proposed in this thesis is to achieve sub-5 nm FePt grains without adversely affecting its coercivity. Instead of adding dopants to the FePt film, a small amount of helium (0.5-1% by volume) was added to the argon sputtering gas. The change in the magnetic properties of $L1_0$ FePt has been studied. Helium in the sputtering gas mixture is supposed to modify the ion current density of the plasma inside the chamber and bring about an improvement in the chemical ordering, out-of-plane coercivity and reduction in the grain size of $L1_0$ FePt. Careful characterization of these magnetic films helped in gaining a proper understanding of the mechanism underlying the decrease in grain diameter with small increments in the helium amount. This study has aided in devising an approach to attain grain diameters as small as 3-4 nm.

- **$L1_0$ FePt magnetic media for BPM application:** One of the challenges of BPM is planarization of the media surface to prevent fly height modulation. Planarization is important since the physically modified recording layer exhibits higher roughness. This further gives rise to defects, poorer contact detection and increased corrosion. There have been studies (details provided in Chapter 2) on achieving patterned media that employ the ion implantation technique since it eliminates the requirement of planarization of the disk surface. The Gaussian peak of the implantation profile in such cases lies at the center of the recording layer and requires the usage of high energy values of a few keV [16]. However, this is accompanied by the lateral straggle of ions (and host atoms) into the masked regions which deteriorate the behavior of the magnetic regions. The easy axis of magnetization is changed if the material is $L1_0$ FePt. A scheme, therefore, needs to be developed to reduce lateral straggle associated with irradiation-assisted BPM fabrication. A simple solution is the use of lower ion (embedding) energies. The crystallography of $L1_0$ phase FePt, size and direction of the incoming ion, and basic understanding of the different facets of ion beam mixing, especially channeling in crystals, can lead to the creation of magnetic and non-magnetic matrices at lower embedding energies. This has been demonstrated with the use of lighter C^+ ions embedded in FePt films at energies as low as ~350 eV.

- **Large area patterning of FePt employing self-assembly:** Being highly scalable, cost-effective and faster, self-assembly is a potential candidate to create etch masks for designing patterned media. However, most studies pertaining to self-assembly have been confined to controlling and tuning the feature size and interspacing [17]. Patterning *via* self-assembly requires physical movement of the polymer chains to arrange into features. However, there have been no reports regarding the effect of media surface on the assembly of block copolymers. FePt media surfaces exhibit large roughness values owing to grain growth during high temperature depositions. The movement of these polymer chains might be kinetically hindered by the corrugated surface. Therefore, it is essential to carry out a systematic study on the self-assembly of block copolymers with varying surface roughness in order to use this technique on FePt surfaces to achieve BPM densities ≥4 Tb/in^2.

1.4 Organization of Thesis

Chapter 1 introduces the readers to HDDs and the challenges associated with the future of magnetic data storage technologies. Research objectives, based on few of these existing challenges, have been designed and provided. Efforts have been made to fulfill these objectives in the later chapters. This is followed by Chapter 2 in which a review on the basic concepts of magnetism has been presented to understand the origin of magnetic storage medium. History of magnetic recording and current status of the field of HDDs have been discussed in detail as well. Chapter 3 briefly discusses the instruments used in investigating the FePt films (and other magnetic samples) for the applications discussed above. Chapter 4 investigates FePt media for HAMR application. Chapters 5 and 6 examine the properties of low energy ion embedded FePt media for potential application in patterned media. Chapter 7 explores the self-assembly of block copolymers on surfaces with roughness varying on the angstrom-scale to employ it as a high throughput patterning technique for BPM fabrication. Finally, Chapter 8 summarizes the thesis and presents the conclusion and possible future works.

References

[1] E. D. Daniel, C. D. Mee, and M. H. Clark, *Magnetic Recording: The First 100 Years*, Wiley-IEEE Press, New York (1999).

[2] A. Moser, K. Takano, D. T. Margulies, M. Albrecht, Y. Sonobe, Y. Ikeda, S. Sun, and E. E. Fullerton, Magnetic recording: Advancing into the future, J. Phys. D: Appl. Phys. **35**, R157 (2002).

[3] E. Grochowski and R. Halem, Technological impact of magnetic hard disk drives on storage systems, IBM Systems Journal [online] (2003). Available at: http://www.cs.princeton.edu/courses/archive/spr05/cos598E/bib/grochowski.pdf

[4] Hitachi shows technical feasibility of perpendicular magnetic recording at 610 Gbit/in^2 [online] (2008, July 28). Available at: http://www.hitachi.com/New/cnews/080728b.pdf

[5] R. Sbiaa and S. N. Piramanayagam, Patterned media towards nano-bit magnetic recording: fabrication and challenges, Recent Pat. Nanotechnol. **1**, 29 (2007).

[6] S. N. Piramanayagam, Perpendicular recording media for hard disk drives, J. Appl. Phys. **102**, 011301 (2007).

[7] H. J. Richter, The transition from longitudinal to perpendicular recording, J. Phys. D. Appl. Phys. **40**, R149 (2007).

[8] R. H. Victora and X. Shen, Composite media for perpendicular magnetic recording, IEEE Trans. Magn. **41**, 537 (2005).

[9] S. N. Piramanayagam and T. C. Chong, *Developments in Data Storage: Materials Perspective*, Wiley-IEEE Press (2011).

[10] J.-G. Zhu, X. Zhu, and Y. Tang, Microwave-assisted magnetic recording, IEEE Trans. Magn. **44**, 125 (2008).

[11] R. E. Rottmayer *et al.*, Heat-assisted magnetic recording, IEEE Trans. Magn. **42**, 2417 (2006).

[12] Mark H. Kryder *et al.*, Heat-assisted magnetic recording, Proc. IEEE, **96**, 1810 (2008).

[13] B. D. Terris, T. Thomson, and G. Hu, Patterned media for future magnetic data storage, Microsyst. Technol. **13**, 189 (2007).

[14] W. B. Byun, K. J. Lee, and T. D. Lee, Effects of SiO_2 addition in FePt on microstructures and magnetic properties on two different MgO substrates, IEEE Trans. Magn. **45**, 2705 (2009).

[15] Y. F. Ding, J. S. Chen, B. C. Lim, J. F. Hu, B. Liu, and G. Ju, Granular $L1_0$ FePt:TiO_2 (001) nanocomposite thin films with 5 nm grains for high density magnetic recording , Appl. Phys. Lett. **93**, 032506 (2008).

[16] N. Gaur *et al.*, Lateral displacement induced disorder in $L1_0$ FePt Nanostructures by ion-implantation, Sci. Rep. **3**, 1907(7) (2013).

[17] R. Ruiz *et al.*, Density multiplication and improved lithography by directed block copolymer assembly, Science, **321**, 936 (2008).

CHAPTER 2

Literature Review: Magnetism Fundamentals and Magnetic Recording

2.1 Magnetism Fundamentals

Magnetism deals with the forces exerted by a magnet on other magnets. The origin and fundamentals of magnetism which lie in electric currents and magnetic moments in elementary particles will be discussed in this section [1].

The magnetic flux density calculated using the Biot-Savart's law at a location, $\vec{\mathbf{r}}$, generated from a current (moving charges) carrying wire is:

$$\vec{\mathbf{B}} = \frac{\boldsymbol{\mu}_\mathbf{0}}{\mathbf{4\pi}}\iiint \frac{\vec{\mathbf{J}}\left(\overrightarrow{\mathbf{r}'}\right) \times \left(\vec{\mathbf{r}} - \overrightarrow{\mathbf{r}'}\right)}{\left|\vec{\mathbf{r}} - \overrightarrow{\mathbf{r}'}\right|^{\mathbf{3}}}\,\mathbf{d}^{\mathbf{3}}\overrightarrow{\mathbf{r}'} \qquad \text{Equation 2.1}$$

where $\vec{\mathbf{J}}\left(\overrightarrow{\mathbf{r}'}\right)$ is the current density at the location $\overrightarrow{\mathbf{r}'}$.

An electron in an atom possesses two degrees of freedom, i.e., spin ($\overrightarrow{\mathbf{s}_\mathbf{i}}$) and orbital ($\overrightarrow{\mathbf{l}_\mathbf{i}}$) angular momentum. Therefore, the total orbital angular momentum and the total spin angular momentum in the atom are defined as $\vec{\mathbf{L}} = \sum \overrightarrow{\mathbf{l}_\mathbf{i}}$ and $\vec{\mathbf{S}} = \sum \overrightarrow{\mathbf{s}_\mathbf{i}}$, respectively. This gives rise to a net angular momentum, $\vec{\mathbf{J}} = \vec{\mathbf{L}} + \vec{\mathbf{S}} \neq \mathbf{0}$, which is responsible for the magnetic moment in atoms. However, magnetism in most materials arises from uncompensated electron spins instead of orbital angular momentum. The quenching of the electron's orbital angular momentum is likely to occur due to the bare possibility of the electron in a certain orbital undergoing rotation to move to another orbital of the same degeneracy. The transition elements (Mn, Cr, Fe, Ni, and Co) have unfilled 3d shells and hence, the uncompensated electron spins are responsible for the magnetic moments.

The density of induced/permanent magnetic moments, $\vec{\mathbf{m}}$, within the material is magnetization, $\vec{\mathbf{M}}$, of a magnetic material.

$$\vec{\mathbf{M}} = \frac{\mathbf{1}}{\mathbf{V}}\sum \vec{\mathbf{m}_\imath} \quad \text{Equation 2.2}$$

Hence, when a magnetic material is placed in $\vec{\mathbf{B}}$, the magnetic field strength, $\vec{\mathbf{H}}$, in the material, not taking into account the magnetic response of the material, is

$$\vec{\mathbf{H}} = \frac{\vec{\mathbf{B}}}{\boldsymbol{\mu}_\mathbf{0}} - \vec{\mathbf{M}} \quad \text{Equation 2.3}$$

where $\boldsymbol{\mu}_\mathbf{0}$ is the permeability of free space.

There are materials in which atoms have magnetic moments ordered parallel to one another without the application of any external magnetic field. These solids exhibit ferromagnetism that result from the quantum mechanical exchange coupling between the electron spin moments. The exchange interaction/energy ($\mathbf{E_{ex}}$) between two nearest neighboring atoms i and j bearing spins $\vec{\mathbf{S}_\imath}$ and $\vec{\mathbf{S}_\jmath}$ has the following form:

$$\mathbf{E_{ex}} = -\sum_{\mathbf{i}<j} \mathbf{2J_{ij}}\vec{\boldsymbol{S}_\imath}.\vec{\boldsymbol{S}}_\mathbf{j} \quad \text{Equation 2.4}$$

where $\mathbf{J_{ij}}$ is the exchange constant which is dependent on electrostatic interaction between the atoms and interatomic spacing (i.e. overlap of charge distributions on the i and j atoms). For ferromagnetic materials, $\mathbf{J_{ij}}$ is greater than zero. This is in accordance with Pauli's exclusion principle which states that electrons with spin moments parallel to each other are separated by large distances, leading to reduced coulomb interaction between them. Fe, Ni, Co, and Gd are ferromagnetic elements.

Magnetization in ferromagnetic materials produces a stray field known as the demagnetization field ($\vec{\mathbf{H}}_{\mathbf{d}}$) which spreads from the material itself to the region outside. $\vec{\mathbf{H}}_{\mathbf{d}}$ as a function of $\vec{\mathbf{M}}$ is written as:

$$\overrightarrow{\mathbf{H}_{\mathbf{d}}} = -\mathbf{N}\,\vec{\mathbf{M}} \qquad \text{Equation 2.5}$$

where $\mathbf{N}$ is the demagnetization tensor and depends on the shape of the magnet.

Therefore, in order to minimize the internal energy of the material/system generated from the demagnetizing field, in the absence of any external field, magnetic domains are formed. The magnetic moments are aligned along the same direction within each domain. However, the domains themselves are oriented in random directions such that the net magnetic moment of the material is zero. Two adjacent domains are separated by a boundary called a domain wall. It is a finite width across which the gradual transition between magnetizations takes place. Domain walls reduce the effect of the stray field from neighboring domains. However, their creation costs exchange energy due to the continuous change in the direction of the magnetic moments involved.

Magnetic properties of materials can be direction-dependent, giving rise to magnetic anisotropy. This property is expressed as magneto-crystalline anisotropy if the magnetic moments in the ferromagnetic solid align along certain preferred directions due to its well-defined crystalline structure. Magneto-crystalline anisotropy originates from the crystal electric field which is produced in the material by non-uniform charge distribution arising from the partial ionization of the neutral atoms. The extent of ionization depends on the chemical bonding of the orbitals on a particular atom with its immediate environment. The orbitals of the neighboring atoms overlap and are oriented in the direction dictated by the crystal field. The interaction of the electron's spin with the magnetic field generated by its orbital motion about the nucleus eventually causes the spin to align parallel to the crystal field’s direction. Therefore, magnetization in materials possessing magneto-crystalline anisotropy saturates easily along certain preferred crystallographic directions. These are known as easy axes (EAs). In contrast, the crystallographic directions along which magnetization do not saturate easily are known as hard axes (HAs).

The discussion on domains, domain walls and magnetic anisotropy is necessary to understand the switching mechanism in ferromagnets under the application of an external magnetic field. In multi-domain particles, magnetization along the direction of the field increases with increasing field strength through domain wall propagation. As field values are incremented further, the size of the domains with magnetization parallel to the applied field’s direction expands and domain wall motion becomes irreversible. Finally, at higher fields, the moments in the domain undergo spontaneous rotation.

There is a critical radius below which a multi-domain particle becomes a single-domain particle. Single-domain particles come into existence when the exchange energy required to form domain walls is greater than the energy involved in reducing the stray fields from adjacent domains. In these particles, all the spins flip together to orient themselves along the direction of the external field. This type of switching is known as coherent rotation. The response of these single-domain magnets to the applied field can be understood through mathematical equations developed by E. D. C. Stoner and E. P. Wohlfarth, and is presented in the Stoner-Wohlfarth model. The model assumes the particles to be ellipsoidal and having uniaxial anisotropy.

Ferromagnetic material, placed in an alternating cycle of an external magnetic field, traces out a hysteresis curve as shown in Figure 2.1. The hysteresis is a plot of magnetization versus external field.

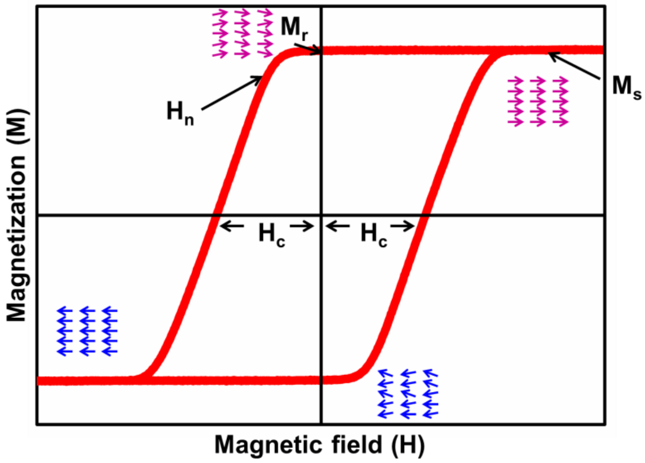

Figure 2.1: Hysteresis loop of a ferromagnet.

From the figure, when the field is incremented from zero to positive field values, the magnetization increases in a non-linear fashion. At large field values, all the moments are aligned in the direction of the field (**saturation magnetization**, **M_s**). However, when the field is reversed to zero the material is able to retain its magnetization (**remanent magnetization, M_r**). The field is then driven to negative values and at a certain value, the magnetization is reduced to zero. This is known as **coercivity** (**H_c**) and is an extrinsic property that is dependent on the microstructure of the ferromagnet. Materials with high coercivity (~5 kOe) are called hard magnets. They retain their magnetization even after the removal of the external magnetic field. On the other hand, soft magnets possess low coercivity (~100 Oe) and demagnetize easily upon removal of the magnetic field. At large negative field values, the magnetization switches and starts to saturate in the opposite direction.

For hard magnets used in data recording applications, coercivity, coercivity squareness, and remanance squareness form the figures of merit. **Remanance squareness** ($\mathbf{S^r}$), shown in Equation 2.6, is the ratio of remanent to saturation magnetization. The strength of read signal from the magnetic material is dependent on this ratio. **Coercivity squareness** ($\mathbf{S^*}$) is the measure of the field distribution at which the magnetization of the ferromagnet rotates from one direction to the other (Equation 2.7).

$$\mathbf{S^r = \frac{M_r}{M_s}, 0 \leq S^r \leq 1} \qquad \text{Equation 2.6}$$

$$\mathbf{S^* = 1 - \frac{M_r}{\chi_0 H_c}, \chi_0 = \left(\frac{\partial M}{\partial H}\right)_H, 0 \leq S^* \leq 1} \qquad \text{Equation 2.7}$$

If $\mathbf{S^r}$ and $\mathbf{S^*}$are equal to one, the hysteresis loops are square and that implies that all the magnetic moments switch at the same field value. Usually, $\mathbf{S^r}$ and $\mathbf{S^*}$are less than one. The demagnetization field from neighboring domains in a ferromagnetic material causes the moments to switch at different field intervals. This gives rise to **nucleation field** ($\mathbf{H_n}$), which is the initial field value at which 10% of the net magnetization has switched to the opposite direction. To summarize, the property of a magnet to exhibit two polarities which can be used for denoting bits ‘1’ and ‘0’ has paved the way for magnetic data storage revolution.

2.2 History of Magnetic Recording

The fundamentals of magnetic data storage for audio recording were first suggested by Oberlin Smith in 1878 and were published in an article for Electrical World in September 1888. In 1898, Valdemar Poulsen was the first to put the principles of magnetic recording in use to design a hard steel wire media which could be magnetized and demagnetized continuously along its length and called it the 'Telegraphone'. Further improvements were made in this field by Austrian inventor Fritz Pfleumer who produced the first magnetic tape recorder comprising pulverized iron particles adhered to a paper strip of width 16 mm. Since paper was not a suitable choice for a commercial product, it was substituted by a 30 µm thick and 6.5 mm wide cellulose acetate strip coated with a mixture of carbonyl iron and more cellulose acetate to create the magnetic tape. This led to the invention of 'Magneto phone' in 1934, which was the first reel to reel recorder. A tape length of 1500 m resulted in a playing time of 25 minutes. After World War II, magnetic tape recording was heavily used in radio broadcasting, music and video recording [2]. The usage of magnetic recording principles in digital information storage began from 1950 onwards. Magnetic core memory for non-volatile data storage used many arrays of small doughnut-shaped ferric toroids, which were magnetized along the clockwise and anti-clockwise directions to represent '1' and '0' [3]. However, it was in 1956 that a major breakthrough occurred in this field in the form of IBM's random access method of accounting and control (RAMAC) hard disk drive (HDD). It consisted of 50 disks, each 24 inch in diameter, providing a storage capacity of 5 Mb at an areal density of 2 kb/in^2 [4]. The initial disk drives contained particulate storage media which were similar to those used in tape recording. Barium ferrite ($BaFe_2O_4$) and iron oxide (Fe_2O_3) magnetic particles of dimensions ~0.5 μm were synthesized via chemical reactions and then embedded into an organic matrix to form a volume fraction of 20-45%. These were then coated on disks rotating at high speed. In 1980, thin film technology was introduced and applied in hard disk drives, restricting the use of particulate media to floppy drives [5]. These films were grown using the sputtering process. An ideal thin film recording layer was composed of uniform and exchange decoupled magnetic grains with high anisotropy and coercivity. The size of these grains was lower than the bit size such that many grains represented a bit. An important measurement in HDDs has been its areal density. Continuous advancement in the field of magnetic recording in HDDs over a span of 50 years has resulted in a striking areal density growth of the order of 10^8 times [6]. Present-day HDDs which are 2.5 inches in diameter have an areal density of 600 Gb/in^2.

The recording mode in earlier HDDs used to be longitudinal, i.e., magnetizations were oriented parallel to the disk surface. However, with the aim of increasing the areal density further, longitudinal recording was replaced by perpendicular recording in 2006. The magnetizations were aligned along a direction perpendicular to the disk surface. Recording media based on these two technologies are discussed in detail in the following section.

2.3 Conventional Recording Schemes

2.3.1 Longitudinal Magnetic Recording (LMR)

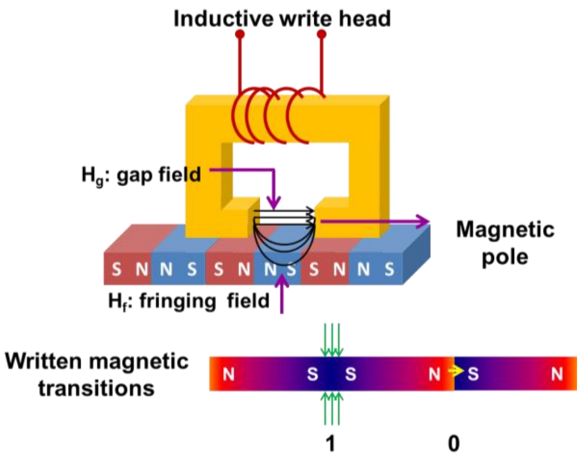

Figure 2.2 Schematic of LMR.

The longitudinal mode of recording was used for both particulate and thin film media. Co-based alloys such as CoPt were employed for producing magnetic media using thin film technology. These alloys exhibit a hexagonal close packed structure (hcp) with the easy axis of magnetization lying along the *c*-axis. Pt helps in improving the anisotropy of the media and, therefore, provides high coercivity. Additive elements like Ta, B and Cr were used to segregate the magnetic grains and prevent exchange coupling between them [7, 8]. In order to orient the *c*-axis parallel to the substrate surface, a Cr-based underlayer [9-11] was used which developed a (200) texture upon deposition at 250 ºC. This led to the epitaxial growth of the Co alloy along the (1120) crystallographic direction. Figure 2.2 demonstrates longitudinal recording. An inductive write head was used and the fringing field from the magnetic poles was employed for writing the bits. The presence and absence of a magnetic transition implied recording bits ‘1’ and ‘0’ respectively.

An areal density slightly higher than 100 Gb/in^2 was reached with LMR [12]. The signal-to-noise ratio (SNR) achieved from a conventional storage media, which includes LMR media, is dependent on the number of grains defining a bit. Therefore, it is essential that the number of grains comprising a bit should be large enough to ensure a high SNR. However, the scaling down of the grain size in LMR was restricted by the onset of superparamagnetism [13] − a phenomenon in which the magnetic anisotropy energy of the particle is comparable to the ambient thermal energy. As a result, thermal fluctuations randomly flip the magnetization between parallel and antiparallel orientations. To prolong longitudinal recording further, anti-ferromagnetically coupled (AFC−LMR) media was introduced [14-16]. A Ru layer of a specific thickness was introduced between two magnetic layers to couple them in anti-parallel directions [17]. This constituted antiferromagnetic coupling and provided additional anisotropy energy to stabilize the magnetization in one direction and prevent superparamagnetism.

Beyond ~130 Gb/in^2, LMR faced other issues such as a higher demagnetizing field from the densely packed bits, high media jitter arising from the zigzag nature of the recorded magnetic transitions, and lower head fields. This paved the way for perpendicular magnetic recording.

2.3.2 Perpendicular Magnetic Recording (PMR)

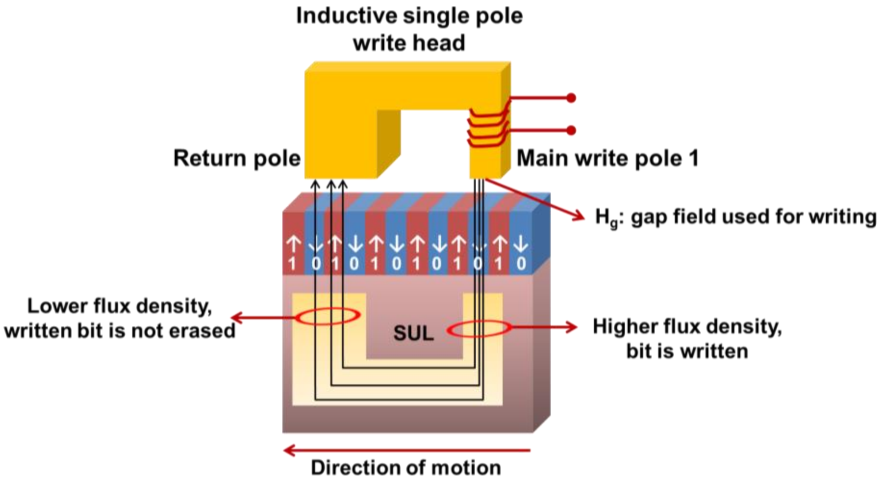

Figure 2.3 Schematic of PMR.

The issues associated with LMR had been foreseen and research on PMR began as early as 1975. Iwasaki and Takemura demonstrated that at higher linear densities, demagnetizing fields induced circular magnetization in the LMR media which, in turn, affected the output voltage adversely. They proposed PMR which, on the other hand, showed reduced demagnetization field with increasing linear densities [18-20]. As shown in Figure 2.3, the PMR media is used in conjunction with a single pole head. An additional layer known as the soft magnetic underlayer (SUL) is introduced into the media stack to act as the second magnetic pole. Therefore, unlike LMR, the gap field instead of the smaller fringing field between the poles is employed for writing the bits. Properties of the SUL include high saturation magnetization, high permeability along the circumferential direction and low permeability along the radial direction to avoid adjacent track erasure. The SUL forms an imaging layer which increases the write field gradient of the single pole head. Higher write fields enable the usage of materials possessing higher magneto-crystalline anisotropy and smaller grain sizes [21, 22].

Amongst many potential candidates for PMR such as Co/Pd multilayers [23], CoCrPt alloys [24] and CoCrPt-oxide based alloys [25, 26], CoCrPt-oxide based magnetic layers are currently being used in PMR. The oxide material introduced into the recording layer for grain segregation is usually in the form of SiO_2, TiO_2 or Ta_2O_5 [27-29]. A (00.2) textured hcp Ru underlayer is commonly used for inducing perpendicular orientation of the *c*-axis of the CoPt alloy. In addition, magnetic grain size is also controlled by depositing another intermediate layer of Ru at high pressure [30, 31]. For SULs, amorphous materials such as CoTaZr or FeCoB are suitable choices. These are antiferromagnetically coupled through a spacer layer to minimize the spike noise arising from the domain walls of the SUL [32-34].

Continuous improvement in the design of SULs, intermediate layers, underlayers as well as the magnetic layer in PMR has resulted in the denser packing of bits and pushed the areal density growth to ~600 Gb/in^2 [35]. The storage density growth rate has been augmented to 40% annually since 2007 [36].

2.4 Magnetic Trilemma: Limitation posed on PMR for areal densities >1 Tb/in^2

The PMR technology is believed to prolong the areal density limit to 1 Tb/in^2. Beyond 1 Tb/in^2, it is expected to be on a downtrack due to the emergence of a set of limits known as the magnetic trilemma [37]. The trilemma comprises of thermal stability, SNR and writability issues and has been displayed in Figure 2.4.

The issue of thermal instability arises due to the phenomenon of superparamagnetism. It was originally suggested by Néel in 1949 and later demonstrated by Bean and Livingston that single domain ferromagnetic particles behave as paramagnets at elevated temperatures [38]. Unlike the paramagnets, these ferromagnets have large saturation magnetization and hence are termed 'superparamagnetic'. An energy barrier, referred to as magneto-crystalline anisotropy energy, prevents the moments present in each magnetic grain of the recording media from switching its alignment along one easy axis to the opposite. The energy product is expressed as $\mathbf{K_u V}$, where $\mathbf{K_u}$ is the magneto-crystalline anisotropy constant and $\mathbf{V}$ is the volume of the magnetic grain. The thermal energy product is given as $\mathbf{K_b T}$, where $\mathbf{K_b}$ is the Boltzmann constant and $\mathbf{T}$ is the absolute temperature. When this thermal energy becomes comparable to the magnetic anisotropy energy of the ferromagnetic particle, spontaneous reversal of the magnetic moment occurs, eventually leading to the erasure of bits recorded in the magnetic media [39]. Therefore for sufficient data retention in HDDs, the inequality shown in Equation 2.8 should be followed [40].

$$\frac{\mathbf{K_u V}}{\mathbf{K_b T}} \geq \mathbf{60} \qquad \text{Equation 2.8}$$

The other parameter in the magnetic trilemma is the SNR of the magnetic media. The larger the number of magnetic grains in a bit, the higher is the SNR. It is used as a measure of reliability with which bits at a particular linear density can be read from a storage media [21]. It is defined as:

$$\mathbf{SNR = 10logN} \qquad \text{Equation 2.9}$$

where $\mathbf{N}$ is the number of grains in a bit.

To understand the magnetic trilemma, it should be noted that the grain size require to reach an areal density of 600 Gb/in^2 using the PMR recording scheme is ~6 nm [21, 35]. To attain areal densities ≥1 Tb/in^2, denser packing of bits is required and this in turn means the shrinkage of grain sizes to less than 6 nm. Each bit can then accommodate a larger number of grains in order to maintain the high SNR. However, the inequality presented in Equation 2.8 may not be valid if the grain volume is reduced below a critical value. In other words, the magnetic media becomes thermally instable. In this case, high anisotropy-magnetic material as the recording layer comes across as a suitable alternative to the Co-based alloys to prevent data erasure. High anisotropy values will cause the grains to exhibit higher coercivity. This will affect the writability on the magnetic media since the write head field required to record the bits needs to be increased as well. However, at present, the available head field is restricted by the maximum magnetic flux density of the materials (~2.4 T) [37], thereby posing an uncertainty over the usage of storage materials possessing large magneto-crystalline anisotropy. The magnetic trilemma has necessitated the development of unconventional recording schemes which will be discussed in detail in the forthcoming sections.

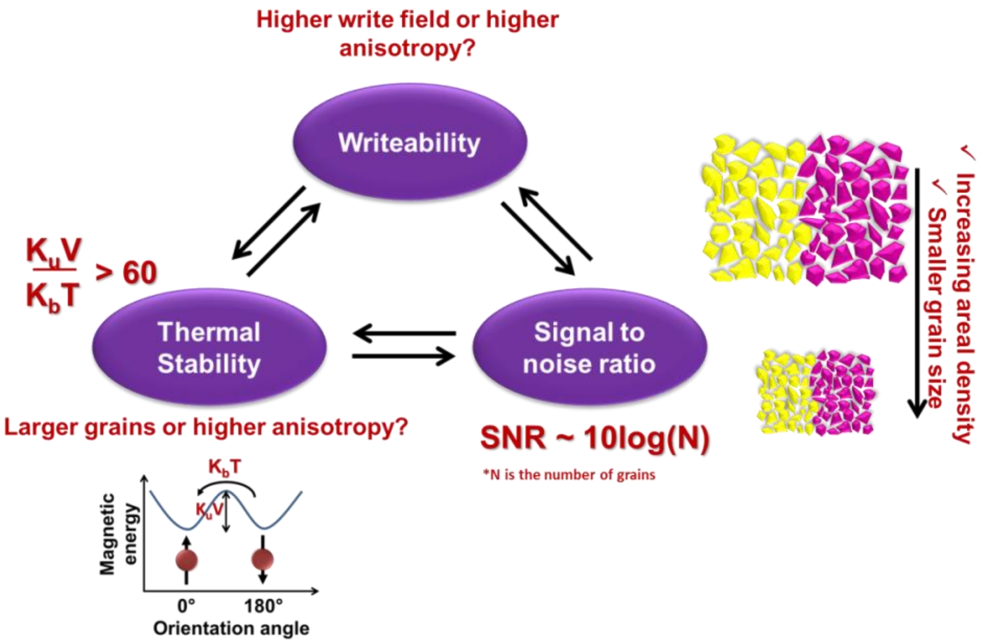

Figure 2.4 Representation of magnetic recording trilemma.

2.5 Advanced recording schemes for areal densities >1Tb/in^2

2.5.1 Exchange Coupled Composite Media (ECC)

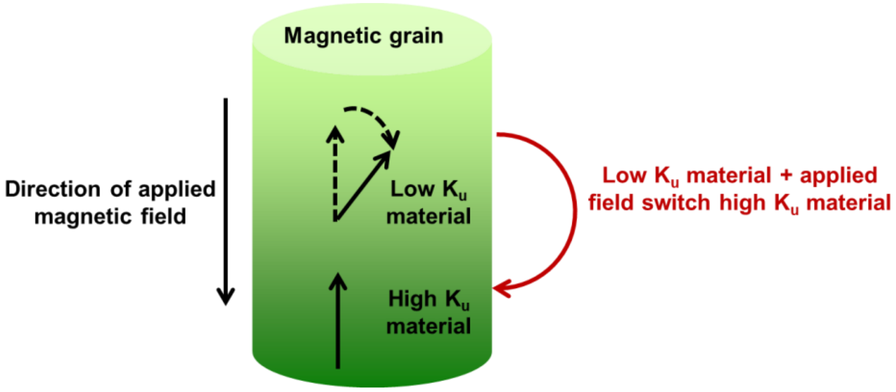

Figure 2.5 A grain with hard and soft magnetic regions in an ECC media.

First among the competing technologies is exchange coupled composite media (ECC). Proposed by Victora *et al.* [41], ECC media comprise of high and low anisotropy (also called magnetically hard and soft, respectively) regions within the same grain. The easy axis of magnetization for both layers is oriented in the direction perpendicular to the recording layer surface. The switching of the magnetization of the soft layer exerts a torque on the hard layer through the exchange coupling present between the two layers, and thus reduces the magnitude of the write field which needs to be applied to switch the high anisotropy layer. Hence, neither writability nor thermal stability is compromised [42]. In the two spin model assumed by Victora *et al.*, the field applied to the soft layer tilts the easy axis of magnetization by an angle of 45°. Therefore, the effective field acting on the hard layer is at 45°, which eventually results in coherent rotation of the magnetization of the hard layer at a reduced switching field in accordance with the Stoner-Wohlfarth model. In a similar but independent work, Suess *et al*. demonstrated the exchange spring media (ESM) which, too, consists of strongly exchange coupled magnetically soft and hard layers [43]. The concept of ESM is explained in terms of domain wall pinning, which occurs at the soft/hard layer interface on the application of an external field. The domain wall propagates through the interface into the hard layer, thus reducing the field required to switch the bilayer. A schematic of a typical magnetic grain in an ECC media has been displayed in Figure 2.5.

The incorporation of non-magnetic spacer layers, with thicknesses in the angstrom range, between the hard and soft magnetic layers has been shown to control the extent of interlayer coupling between them and, thus, helped in tuning the switching field accordingly [44]. Instead of having two layers with two distinct anisotropy values, the use of multilayers, in which the anisotropy constant varies gradually from the magnetically softest to the hardest layer, has also been suggested. It has been suggested and experimentally demonstrated that the implementation of this type of anisotropy graded media structure can provide a more effective reduction of the write field, eventually leading to improved recording performance [45, 46]. Therefore, ECC media has the ability to prolong the use of perpendicular magnetic recording beyond 1Tb/in^2 in HDDs, prior to the introduction of other recording techniques which require major changes in the storage media and the read/write head configuration.

2.5.2 Energy Assisted Magnetic Recording (EAMR)

An alternative route to achieve improved writability without sacrificing thermal stability is the use of energy-assisted recording such as microwave-assisted magnetic recording (MAMR) and heat-assisted magnetic recording (HAMR) [47]. These techniques, similar to ECC magnetic media, also support the use of magnetic materials with high magneto-crystalline anisotropy (K_u) in HDDs to store data in smaller sized (<5 nm) thermally stable grains. In MAMR, a write field is applied in the direction parallel to the magnetic layer's easy axis of magnetization. In addition, an alternating magnetic field, of few kilo oersteds (kOe) *only* and frequency in the microwave range, is applied along the axis orthogonal to the write field. This causes the precessional motion of the magnetization through the ferromagnetic resonance effect. The excitation of the precessional motion by the alternating field can assist magnetization reversal in the media at a reduced magnitude of write field [48]. MAMR is still in its initial stages of development. The switching field and switching dynamics as well as damping and dissipative processes in media are not well-known and are currently being studied. HAMR, on the other hand, utilizes the inverse relationship existing between temperature and magnetic properties including anisotropy, saturation magnetization and coercivity.

2.5.2.1 Heat Assisted Magnetic Recording (HAMR)

The principle of HAMR is similar to the derivative of magneto-optical recording proposed by Katayama and Saga separately in 1999 [49, 50]. The magnetic media is heated to an elevated temperature which is near to the Curie temperature of the material. The coercivity of the media then drops to a value less than the magnitude of the writing field. After the bit has been written, the heated region is then rapidly cooled down to ambient temperature in the presence of the head field. Provided that the head field is large compared to the local demagnetization field, the magnetization of the media grains will remain oriented in the direction of the externally applied field. The schematic and principle of HAMR are provided in Figures 2.6 and 2.7, respectively.

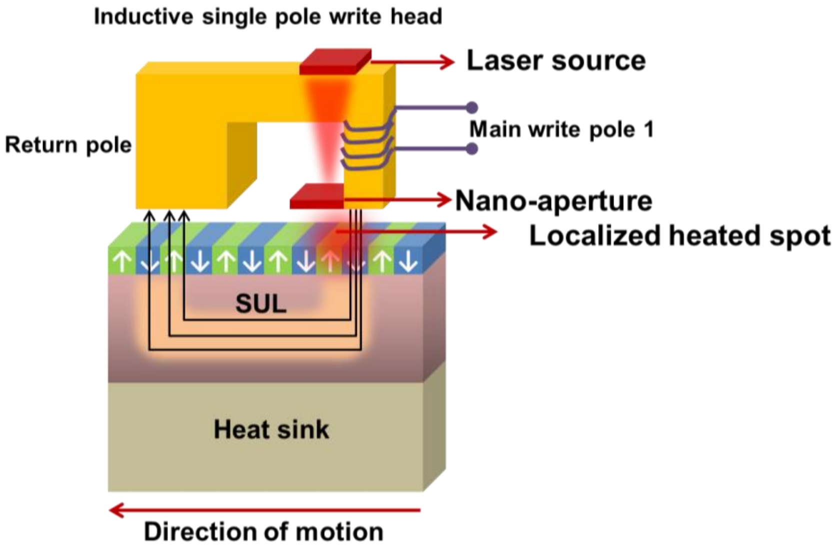

Figure 2.6 Schematic of HAMR.

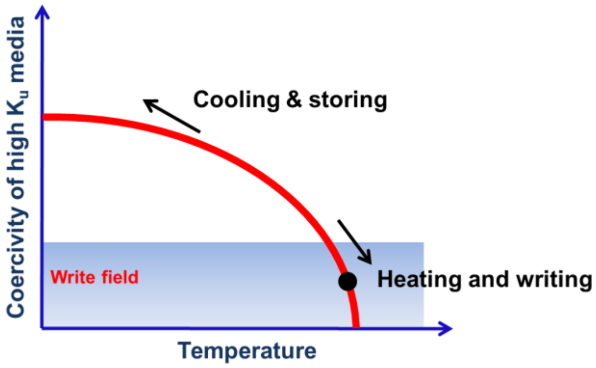

Figure 2.7 Principle of HAMR.

Besides overcoming the problems posed by the magnetic trilemma, HAMR provides a very high effective writing field gradient which requires no contribution from the magnetic character of the recording head. This gradient is comparatively higher than that obtained in conventional PMR. This can be easily explained using the relationship shown below:

$$\frac{\mathbf{dH_{write}}}{\mathbf{dx}} = \frac{\mathbf{dH_k}}{\mathbf{dT}} \times \frac{\mathbf{dT}}{\mathbf{dx}} \qquad \text{Equation 2.10}$$

where $\mathbf{H_{write}}$ is the total write field gradient and $\mathbf{H_k}$ is the anisotropy field.

The first term on the right hand side, i.e.$\frac{\mathbf{dH_k}}{\mathbf{dT}}$, is the anisotropy field gradient as a function of temperature slightly below the Curie temperature. Since the anisotropy of the material vanishes at Curie's temperature, the gradient is, therefore, extremely high near this temperature. The other term on the right hand side which is $\frac{\mathbf{dT}}{\mathbf{dx}}$ represents the temperature gradient at a cooled down temperature. In addition, the localized heating of the medium results in a high thermal gradient as well. Hence, higher write field gradients are expected when HAMR is integrated to the current inductive head design [51, 52].

Two types of recording schemes have been suggested for HAMR. One method uses a beam size spot much larger than the track width so the bit size is determined by the write core width (magnetic dominant way). The other method requires a small beam size spot of ~ 50 nm which is much smaller than the track width. Hence the bit size is determined by this spot size (optical dominant way). For such a small beam diameter, near field optics needs to be applied since ordinary optics cannot produce an optical beam smaller than the diffraction limit [53].

However, a series of challenges lie ahead in this field, which need to be taken into consideration and addressed.

- **Integration of the laser with an efficient light delivery system and effective coupling to the recording media is essential.** To concentrate heat energy on a particular spot on the media, waveguides can be used as they have the ability to confine light in one dimension. In addition, near field transducers can be used in conjunction with the waveguide to enhance the optical field, a few nanometers away from the localized region in the media to be written, by many magnitudes more than the incident field [54, 55].

- **Laser required to locally heat the media needs to be integrated with the writing head.** The magnetic pole material will need to remain far from the waveguide to avoid optical losses in the core and undesirable increase in the write pole temperature. At the same time, it should be brought into close proximity to the waveguide such that the optical spot and the write field are on the verge of coinciding. The possibility of adjacent bits being overwritten would hence lessen [48, 56].

- **Designing a recording media with specific thermal properties to control thermal diffusion within the structure.** The heat flow in the media stack is dependent on the stack geometry and thermal properties of the various materials in the medium. Lateral heat flow can be minimized by placing a relatively thick, highly thermally conductive film (heat sink) below the memory film [52, 57].

- **Degradation of carbon overcoat and lubricant with increase in temperature.** With increasing temperature, the carbon overcoat is graphitized. Degradation\desorption of the lubricant occurs due to thermo-capillary stress produced in it by laser heating under HAMR conditions. Therefore, there is a requirement for lubricants and overcoats to withstand high temperatures, thermal cycling for reliable head/media interface. In addition the coupling of the antenna to the media should not be affected [58, 59].

2.5.2.2 HAMR media candidate: $L1_0$ ordered FePt

As stated previously, harnessing the advanced recording schemes can enable the use of alloys with high magneto-crystalline anisotropy. Alloys exhibiting the $L1_0$ phase such as CoPt, FePd, MnAl and FePt display very high magnetic anisotropy energy and, therefore, are of potential interest [60, 61]. Among these, $L1_0$ FePt displays the highest anisotropy constant of ~7×10^7 erg/cm^3 and its properties have been exploited to achieve the necessary objectives of this thesis [62, 63]. This alloy has an ordered phase due to the alternating arrangement of Fe and Pt atoms in the (002) planes. The modification in the electronic structure of the FePt alloy brought about by the hybridization between the magnetic 3d element (Fe) and the non-magnetic 5d element (Pt), as well as the presence of large spin-orbit coupling in the 5d electrons enhance the magneto-crystalline anisotropy of this material [64]. Due to the alternate stacking of Fe and Pt atoms along the [001] axis, the cubic symmetry changes to face centered tetragonal (fct) with lattice constants, a = 3.852 Å and c = 3.716 Å. Figure 2.8 shows the crystal structures of fcc-disordered FePt and fct-$L1_0$ FePt [6].

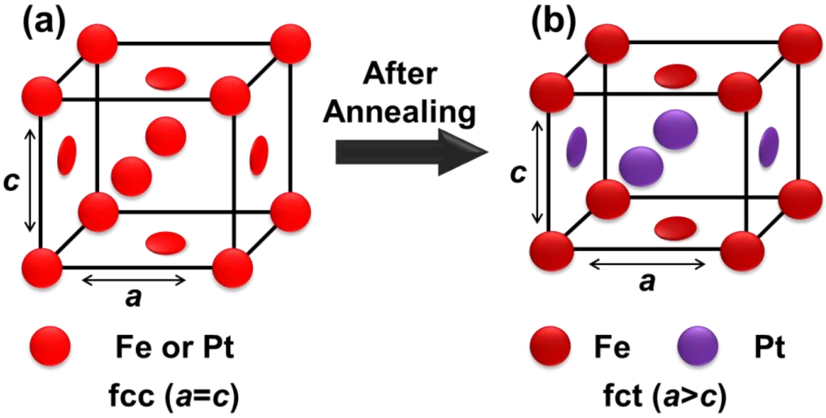

Figure 2.8 Unit cells of (a) fcc disordered FePt and (b) fct-ordered (or $L1_0$ phase) FePt.

From the binary phase diagram of the FePt alloy shown in Figure 2.9, it is inferred that these alloys, with the Pt atomic concentration lying between 35-55%, exhibit the $L1_0$ ordered phase in the temperature range of 600-1300° C. A disorder-order transformation of the alloy from A1-fcc to the $L1_0$ phase is obtained by annealing the FePt alloy at a temperature ≥600° C. However, the degree of ordering of these $L1_0$ FePt films may vary depending on the growth and annealing conditions. The ordering parameter (**S**) is given by:

$$\mathbf{S} = \frac{\mathbf{r_{Fe} - X_{Fe}}}{\mathbf{1 - X_{Fe}}} = \frac{\mathbf{r_{Pt} - X_{Pt}}}{\mathbf{1 - X_{Pt}}} \qquad \text{Equation 2.11}$$

The variable **X** represents the mole fraction of Fe (or Pt). The probability that a Fe (or Pt) sublattice site is occupied by a Fe (or Pt) atom is denoted by **r**. Ideally, **S** should be unity for an entire chemically-ordered FePt film. However, this can only be achieved for a stoichiometric composition free of any crystallographic defects. Therefore, **S** is generally less than unity. On the other hand, for FePt films comprising a random arrangement of atoms throughout [Figure 2.8(a)], **S** is zero [6].

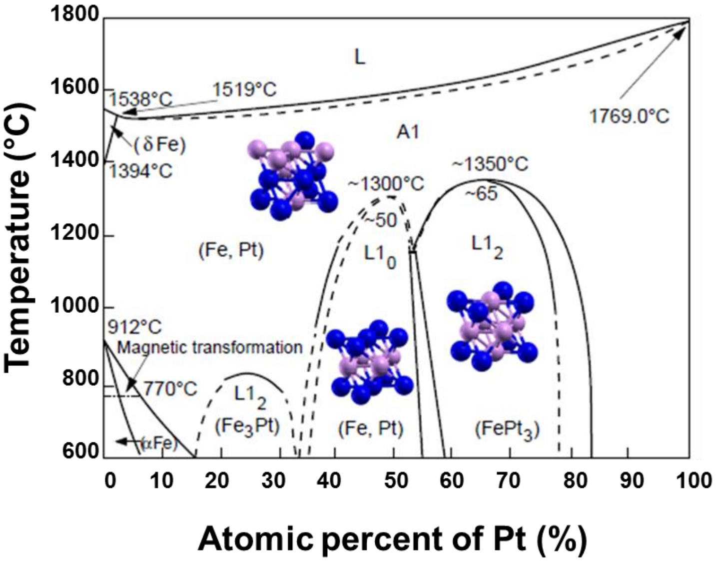

Figure 2.9 Binary phase diagram of FePt [65].

To implement *L1₀* FePt thin films in HDDs for realizing areal densities >1 Tb/in^2, many technical challenges need to be addressed. These include reducing the annealing temperature for phase transformation of the films, enhancing the ordering parameter, perpendicular orientation of the *c*-axis with respect to the film plane to ensure higher out-of-plane coercivity and least in-plane variants, and achieving smaller grain sizes in the range of ~5 nm. Doping of the FePt films with elements such as Au, Ag and Cu have been proven to be effective in promoting higher $L1_0$ ordering at lower temperatures

[66]. Chemical ordering has also been achieved through better lattice mismatch between the FePt film and various underlayers such as MgO, Ag, and CrRu amongst others [67-69], and by sputtering the FePt films at very high pressures (~100 Pa) [70]. While the former approach is used to cause expansion of the *a*-axis and shrinkage of the *c*-axis, the latter favors the $L1_0$ phase creation due to the compressive stress induced along the *c*-axis to bring about an improvement in the degree of ordering of the FePt layer. In order to control the grain size and minimize the exchange interaction between them, insulating materials such as SiO_2, TiO_2, MgO, Al_2O_3 and C have been co-sputtered with Fe and Pt [71-75]. However, the addition of such spacer materials into the magnetic layer generally deteriorates the chemical ordering of the grains. Hence, in this thesis, efforts have been directed towards achieving smaller grain sizes but not at the cost of damaged magnetics of the $L1_0$ phase FePt media.

2.5.3 Bit Patterned Media (BPM)

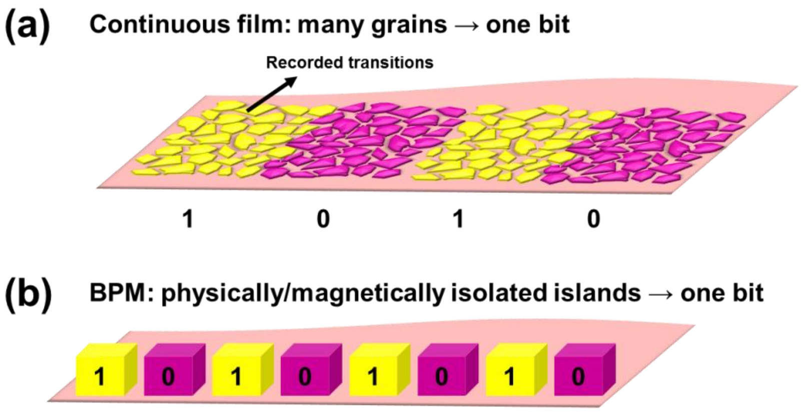

Figure 2.10 (a) Conventional media and (b) bit patterned media.

A different concept to delay the onset of superparamagnetism is BPM. Continuous magnetic film is patterned into islands, and each magnetic island represents one bit. The volume of each bit is larger than the size of an individual grain in the conventional media. Therefore, the large volume of the bit ensures that the thermal stability is retained even if materials with low magneto crystalline anisotropy are used to avoid writability issues. The magnetic entities are physically and magnetically isolated from one another. Since the zigzag grain boundaries between the bits no longer exist, transition noise is reduced. The SNR equation for conventional media can no longer be applied to patterned media [76-79]. The difference between conventional media and BPM has been pictorially presented in Figure 2.10.

Another distinguishing feature of BPM lies in the fact that it can be used in combination with the aforementioned techniques discussed under Section 2.5. There are reports which have demonstrated that HAMR implemented with BPM shows a reduction in thermal diffusion in the nanostructures, thus lessening the problem of adjacent track erasure [80]. On the other hand, exchange coupling between adjacent magnetic grains is eliminated when the concept of ECC media is established in BPM. Bits are magnetically isolated from each other. It is predicted that the combination of BPM with HAMR or ECC could extend the areal density beyond 4Tb/in^2 in future [81].

There are two main challenges in implementing BPM in HDD. The first challenge concerns the fabrication of densely packed patterns to act as masks for the media underneath. The second challenge requires the use of different techniques to transfer these patterns into the magnetic film and create well-isolated magnetic islands/bits. These issues are discussed in the following sections.

2.5.3.1 High density patterning methods

Several methods can be employed to create BPM. However, each of them has its pros and cons. They are discussed briefly below.

- **Deep ultraviolet (UV) lithography** can be used for patterning features below 100 nm. Attainment of densely packed patterns with sizes in the sub-20 nm range may be a challenge. An extension of UV lithography − **extreme UV lithography (EUV)** with a wavelength of ~13.5 nm – can also be considered to fabricate patterned media. However, it comes with a disadvantage, i.e., EUV light is absorbed strongly by solid state materials. As a result, the light does not reach the bottom layer of the spin-coated resist and hence, accurate exposure to obtain the required resist patterns is affected considerably [82].

- The most common and highly preferred lithography technique for patterning a magnetic film is **electron beam lithography (EBL)**. It can be used for creating sub-10 nm nanostructures. However, it is a serial writing process and hence, issues like cost-effectiveness and high-throughput act as bottlenecks for its application in BPM fabrication. Also, the fact that the disks need to be patterned in a circular fashion and not along the X-Y direction requires careful attention [82, 83].

- Chou *et al*. proposed the use of a new type of lithography called **nanoimprint lithography (NIL)** which is based on the mechanical deformation of the resist to make patterned media. A mold with nano-scale features is used for deforming the resist. A high resolution lithography tool like EBL can be used for patterning molds containing closely packed features over a large area. This mold can then be used repeatedly to pattern magnetic films, thereby increasing the throughput and making the technique inexpensive. Research efforts have been directed towards the fabrication of defect-free molds and preventing shearing of the resist when feature densities exceed 1 Tb/in^2 [84, 85].

- Another interesting approach is using **self-organized particles** to form masks to create patterned media. One approach is the anodization of aluminum in an acid electrolyte. This results in the formation of a porous alumina film comprising of hexagonally packed cylindrical pores. The diameter of these pores can be varied from a few hundred nanometers to sub-10 nm by fine-tuning the anodization conditions [86, 87]. A different approach was suggested by Sun *et al*. Solution phase decomposition of iron pentacarbonyl and reduction of platinum acetylacetonate at high temperatures, in the presence of stabilizers oleic acid and oleyl amine, were employed to produce 4 nm diameter FePt nanoparticles. Structural analysis showed the presence of a highly ordered fct-phase in these nanostructures [88]. However, size homogeneity and uniformity in pitch values over a large area of these self-organized particles need to be explored.

- Syntheses of arrays of closely spaced nanostructures have been made possible by the **self-assembly of di- and tri-block copolymers**. The morphology of these self-assembled domains can be spherical or cylindrical depending on the volume fraction of the blocks and is attainable on the sub-20 nm scale [89-92]. The versatility of self-assembly technique has drawn the attention of the high density data storage industry to use it as a scalable, high-throughput and low-cost nanofabrication method to fabricate BPM [89, 93, 94]. Long range ordering and strict position control of these features over large areas have also been realized through directed self-assembly which includes the use of chemically pre-patterned templates [89], graphoepitaxy [90, 91], topographical patterns [92] or by introducing nanoscopic facets on the surface [95]. However, there are other factors which adversely affect the reliability and reproducibility of self-assembly on different substrate surfaces. It should be noted that almost all the self-assembly studies so far reported are on ultra-flat silicon or single crystal substrates [89-92, 95, 96]. There has hardly been any emphasis on the effect of surface roughness of the magnetic media on the self-assembly of block copolymers. This is pivotal if self-assembled masks are to be attained over large areas on media surfaces and has been investigated in an elaborate manner within the scope of this thesis.

2.5.3.2 Pattern transfer to magnetic films to create well-isolated bits

- **Physical etching of the magnetic film not protected by the resist masks**

The nano-patterns can be transferred on to the magnetic film underneath by removing the material not protected by the masks. The surface topography of the magnetic media is then modified into land and grooves. Hence, an additional step – planarization − involving flattening of the media surface, to prevent fly height modulation (FHM) of the read/write head at the head-media interface leading to reduced SNR, is essential [Figure 2.11(a)] [97, 98].

- **High energy ion implantation-assisted BPM fabrication**

An alternative technique, which has drawn the attention of researchers due to its ability to eliminate the requirement of planarization after BPM fabrication, is **ion implantation** [99]. In this technique, magnetic media with pre-formed resist masks on top are exposed to energetic ion irradiation. Damage to the magnetic properties in the unprotected regions of the recording layer, induced by implantation, gives rise to alternate magnetic and non-magnetic regions without significant change in the surface topography [Figure 2.11(b)]. Controlling the coercivity and the anisotropy of the irradiated regions by monitoring the ion fluence was initially demonstrated by Chappert *et al* on Co/Pt multilayers masked with 1 µm line/space features [100]. This has been followed by several studies investigating the magnetic properties of the areas in the continuous films implanted by different ion species such as N^+, Al^+, Si^+, and Ar^+ [101-105]. Reactive ion implantation has also been carried out in Co/Pd multilayers using P^+ and As^+ ions to form covalent (non-magnetic) Co−P and Co−As bonds in the irradiated regions [106].

Despite the exclusion of planarization, the implementation of ion implantation for fabricating high density BPM remains a challenge. For example, in order to reach areal densities ≥ 4 Tbpsi, the magnetic bit size as well as the spacing between the bits is reduced to ≤ 11 nm. In order to implant the species over film thicknesses of ~10 nm, high energy in the range of a few keV is required [101-106]. Lateral straggle arising from such high energy implantation at such nano-dimensions may deteriorate the magnetic behavior of the islands acting as bits. Studies pertaining to lateral straggle in magnetic recording media, in particular at dense pitch, have been limited. Hinoue *et al.* have studied the lateral straggle in the case of N^+ ions in CoCrPt-based media [105]. However, in this study, the mask patterns were fabricated at a pitch of about 160 nm, 20 times larger than the pitch required for 10 Tb/in^2.

In a recent yet innovative study, the conventional CoCrPt-based media with ~2 nm thin oxide grain boundaries have been used as an ideal system to investigate the changes in crystallography and exchange interaction at the sub-10 nm scale brought about by the lateral straggle of the implanted species and the subsequent lateral diffusion of the host atoms into the non-magnetic boundaries. It was shown that the lateral diffusion of the Co and Pt atoms affected the media composition in an adverse manner, thereby increasing the exchange interaction between the grains and deteriorating the necessary magnetic recording properties. Fine-tuning of the alloy composition, accordingly, during deposition could lead to the attainment of requisite magneto-crystalline anisotropy after implantation [107, 108].

Based on the understanding gained from CoCrPt-SiO_2 media, an in-depth examination of implantation in the next generation-high anisotropy $L1_0$ FePt media (inclusive of thin films coated without and with patterned resists) was also carried out. Lateral straggle of the host and the implanted ions into the masked regions resulted in an order-disorder transformation of the FePt alloy. Prior optimization of the FePt alloy composition would then not serve the purpose of achieving the desired chemically ordered phase after ion implantation [109].

- **Low energy ion embedment-assisted BPM fabrication**

It is possible to reduce the lateral straggle in patterned media by using lower ion energies. 20 nm wide $Co_{80}Pt_{20}$ magnetic nano-islands have previously been patterned by using the ion irradiation effect accompanying the oblique-angled Ar^+ ion milling process [110]. While isolated magnetic islands were achieved, the out-of-plane coercivity was very low (~1 kOe). This was attributed to the ions etching away the sidewalls and top portion of the magnetic bit. In another study, low-energy proton irradiation (~0.3 keV) was used for patterning single ferromagnetic domains [111]. The resist masks comprised holes instead of pillars, thereby enabling selective reduction of paramagnetic oxides like $[Co_3O_4/Pd]_{10}$ and $CoFe_2O_4$ to ferromagnetic alloys $[Co/Pd]_{10}$ and CoFe, respectively. However, the domains were 100 nm in diameter. Therefore, the effect of lateral straggle induced reduction of the non-magnetic oxide regions to magnetic regions, with decreasing bit size and increasing areal density, could not be comprehended.

The next-generation $L1_0$ FePt exhibits a crystallography which enables the lighter ion species such as C^+, N^+, and He^+, which have atomic radii less than the lattice constant along the *a*-axis, to traverse through the entire length of the magnetic film when embedded at energies of a few hundred eV *only*. In this thesis, the impact of low energy embedment of C^+ ions on the magnetics of $L1_0$ FePt is investigated. It was observed that bombardment of C^+ ions at an energy of 350 eV in the 5 nm thick FePt films produced a monumental reduction of ~86% in the out-of-plane coercivity value. Apart from the media's crystallography with respect to the size of the incoming ions, its direction also played a significant role in the deeper distribution of the C^+ ions and the associated widespread cascade damages within the magnetic layer. In other words, an order-disorder transformation of the fct FePt alloy occurs. However, unlike ion implantation, the bombardment of the C^+ ions into the magnetic media involves the usage of very low energies (<1 keV), thereby ensuring reduced lateral straggle. The consequences of low energy-lighter ion (C^+ ions) embedding in high anisotropy $L1_0$ FePt to attain high storage densities in BPM have been discussed.

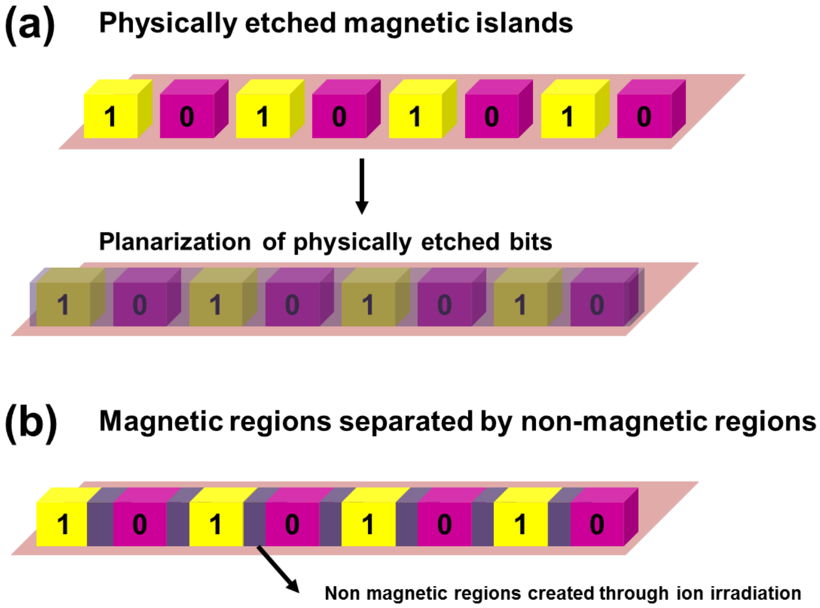

Figure 2.11 Two different approaches of creating patterned media – (a) physically etching of bits and (b) ion irradiation.

References

[1] E. du Trémolet de Lacheisserie, *Magnetism: Fundamentals*, Springer (2004).

[2] E. D. Daniel, C. D. Mee, and M. H. Clark, *Magnetic Recording: The First 100 Years*, Wiley-IEEE Press, New York (1999).

[3] The History of Magnetic Recording, [online] (August 25, 2011) http://h2g2.com/approved_entry/A3224936

[4] A. Moser, K. Takano, D. T. Margulies, M. Albrecht, Y. Sonobe, Y. Ikeda, S. Sun, and E. E. Fullerton, Magnetic recording: Advancing into the future, J. Phys. D: Appl. Phys. **35**, R157 (2002).

[5] S. X. Wang and A. M. Taratorin, *Magnetic Information Storage Technology*, Academic Press (1999).

[6] S. N. Piramanayagam and T. C. Chong, *Developments in Data Storage: Materials Perspective*, Wiley-IEEE Press (2011).

[7] N. Inaba and M. Futamoto, Effects of Pt and Ta addition on compositional microstructure of CoCr-alloy thin film media, J. Appl. Phys. **87**, 6863 (2000).

[8] C.R. Paik, I. Suzuki, N. Tani, M. Ishikawa, Y. Ota, and K. Nakamura, Magnetic properties and noise characteristics of high coercivity CoCrPtB/Cr Media, IEEE Trans. Magn. **28**, 3084 (1992).

[9] D. E. Laughlin, Y. C. Feng, D. N. Lambeth, L. L. Lee, and L. Tang, Design and crystallography of multilayered media, J. Magn. Magn. Mater. **155**, 146 (1996).

[10] L. L. Lee, D. E. Laughlin, L. Fang, and D. N. Lambeth, Effects of Cr intermediate layers on CoCrPt thin film media on NiAl underlayers, IEEE Trans. Magn. **31**, 2728 (1995).

[11] B. B. Lal, M. Tobise, and T. Shinohara, Effect of very thin Cr-underlayer on the magnetic and recording properties of CoCrTa thin-film media, IEEE Trans. Magn. **30**, 3954 (1994).

[12] G. Choe, J. N. Zhou, B. Demczyk, M. Yu, M. Zheng, R. Weng, A. Chekanov, K. E. Johnson, F. Liu, and K. Stoev, Highly in-plane oriented CoCrPtB longitudinal media for 130-Gb/in^2 recording, IEEE Trans. Magn. **39**, 633 (2003).

[13] D. Weller and A. Moser, Thermal effect limits in ultrahigh-density magnetic recording, IEEE Trans. Magn. **35**, 4423 (1999).

[14] B. R. Acharya, A. Inomata, E. N. Abarra, A. Ajan, D. Hasegawa, and I. Okamoto, Synthetic ferrimagnetic media for over 100 Gb/in^2 longitudinal magnetic recording, J. Magn. Magn. Mater. **260**, 261 (2003).

[15] E. N. Abarra, B. R. Acharya, A. Inomata, and I. Okamoto, Synthetic ferrimagnetic media, IEEE Trans. Magn. **37**, 1426 (2001).

[16] J. Lohau, A. Moser, D. T. Margulies, E. E. Fullerton, and M. E. Schabes, Dynamic coercivity measurements of antiferromagnetically coupled magnetic media layers, Appl. Phys. Lett. **78**, 2748 (2002).

[17] S. P. Parkin, N. More, and K. P. Roche, Oscillations in exchange coupling and magnetoresistance in metallic superlattice structures: Co/Ru, Co/Cr, and Fe/Cr, Phys. Rev. Lett. **64**, 2304 (1990).

[18] S. Iwasaki and K. Takemura, An analysis for the circular mode of magnetization in short wavelength recording, IEEE Trans. Magn. 11, **1173** (1975).

[19] S. Iwasaki and Y. Nakamura, The magnetic field distribution of a perpendicular recording head, IEEE Trans. Magn. 14, 436 (1978).

[20] S. Iwasaki, Y. Nakamura, and K. Ouchi, Perpendicular magnetic recording with a composite anisotropy film, IEEE Trans. Magn. **MAG - 61**, 1456 (1979).

[21] S. N. Piramanayagam, Perpendicular recording media for hard disk drives, J. Appl. Phys. **102**, 011301 (2007).

[22] S. Khizroev and D. Litvinov, Perpendicular magnetic recording: Writing process, J. Appl. Phys. **95**, 4521 (2004).

[23] L. Wu, T. Kita, N. Honda, and K. Ouchi, Medium noise properties of Co/Pd multilayer films for perpendicular magnetic recording. J. Magn. Magn. Mater. **193**, 89 (1999).

[24] H. Uwazumi, T. Shimatsu, Y. Sakai, Y. A. Otsuki, I. Watanabe, H. Muraoka, Y. Nakamura, Recording performance of CoCrPt-(Ta, B)/TiCr perpendicular recording media, IEEE Trans. Magn. **37**, 1595 (2001).

[25] T. Oikawa, M. Nakamura, H. Uwazumi, T. Shimatsu, H. Muraoka, and Y. Nakamura, Microstructure and magnetic properties of CoPtCr–SiO_2 perpendicular recording media, IEEE Trans. Magn. **38**, 1976 (2002).

[26] G. A. Bertero, et al. Optimization of granular double-layer perpendicular media, IEEE Trans. Magn. 38, 1627 (2002).

[27] I. Tamai, R. Araki, and K. Tanahashi, Magnetic and recording characteristics of CoCrPt-oxide media with a mixture of SiO_2 and TiO_2, IEEE Trans. Magn. **44**, 3492 (2008).

[28] T. Chiba, J. Ariake, and N. Honda, Structure and magnetic properties of Co-Pt-Ta_2O_5 film for perpendicular magnetic recording media, J. Magn. Magn. Mater. **287**, 167 (2005).

[29] R. Araki, Y. Takahashi, I. Takekuma, and S. Narishige, High-resolution TEM analysis of perpendicular CoCrPt-SiO_2 media, IEEE Trans. Magn. **44**, 3496 (2008).

[30] J. Z. Shi, S. N. Piramanayagam, C. S. Mah, H. B. Zhao, J. M. Zhao, and Y. S. Kay, Influence of dual-Ru intermediate layers on magnetic properties and recording performance of CoCrPt -SiO_2 perpendicular recording media . Appl. Phys. Lett. **87**, 222503 (2005).

[31] S. H. Park, S. O. Kim, T. D. Lee, H. S. Oh, Y. S. Kim, N. Y. Par, and D. H. Hong, Effect of top Ru deposition pressure on magnetic and microstructural properties of CoCrPt-SiO_2 media in two-step Ru layer. J. Appl. Phys. **99**, 08E701 (2006).

[32] B. R. Acharya, J. N. Zhou, M. Zheng, G. Choe, E. N. Abarra, and K. E. Johnson, Anti-parallel coupled soft under layers for high-density perpendicular recording. IEEE Trans. Magn. **40**, 2383 (2004).

[33] S. C. Byeon, A. Misra, and W. D. Doyle, Synthetic antiferromagnetic soft underlayers for perpendicular recording media. IEEE Trans. Magn. **40**, 2386 (2004).

[34] A. Hashimoto, S. Saito, H. Takashima, T. Ueno, and M. Takahashi, Enhancement of interlayer exchange coupling for antiparallel coupled soft magnetic underlayers using FeCoB amorphous material, Magnetics Conference, INTERMAG, IEEE International, 17 (2006).

[35] Hitachi shows technical feasibility of perpendicular magnetic recording at 610 Gbit/in^2 [online] (2008, July 28). Available at: http://www.hitachi.com/New/cnews/080728b.pdf

[36] [36] E. Grochowski and R. Halem, Technological impact of magnetic hard disk drives on storage systems, IBM systems journal, 42, **338** (2003).

[37] H. J. Richter, The transition from longitudinal to perpendicular recording, J. Phys. D. Appl. Phys. **40**, R149 (2007).

[38] C. P. Bean and J. D. Livingston, Superparamagnetism, J. Appl. Phys. **30**, S120 (1959).

[39] J. Eisenmenger and I. K. Scheller, Magnetic nanostructures: Overcoming thermal fluctuations, Nat. Mater. **2**, 437 (2003).

[40] S. H. Charap, P-L Lu, and Y. He, Thermal stability of recorded information at high densities, IEEE Trans. Magn. **33**, 978 (1997).

[41] R. H. Victora and X. Shen, Composite media for perpendicular magnetic recording, IEEE Trans. Magn. **41**, 537 (2005).

[42] J.-P. Wang, W. Shen, and J. Bai, Exchange coupled composite media for perpendicular magnetic recording, IEEE Trans. Magn. **41**, 3181 (2005).

[43] D. Suess *et al.*, Exchange spring media for perpendicular recording, Appl. Phys. Lett. **87**, 012504 (2005).

[44] A. Berger, N. Supper, Y. Ikeda, B. Lengsfield, A. Moser, and E. E. Fullerton, Improved media performance in optimally coupled exchange spring layer media, Appl. Phys. Lett. **93**, 122502 (2008).

[45] C. Abraham and A. Aharoni, Linear decrease in magnetocrystalline anisotropy, Phys. Rev. **120**, 1576 (1960).

[46] D. Suess, Multilayer exchange spring media for magnetic recording, Appl. Phys. Lett. **89**, 113105 (2006).

[47] Y. Shiroishi *et al.*, Future options for HDD storage, IEEE Trans. Magn. **45**, 3816 (2009).

[48] J.-G. Zhu, X. Zhu, and Y. Tang, Microwave assisted magnetic recording, IEEE Trans. Magn. **44**, 125 (2008).

[49] H. Katayama, S. Sawamura, Y. Ogimoto, J. Nakajima, K. Kojima, and K. Ohta, New magnetic recording method using laser assisted read/write technologies, J. Magn. Soc. Jpn. **23**, 233 (1999).

[50] H. Saga, H. Nemoto, H. Sukeda, and M. Takahashi, New recording method combining thermo-magnetic writing and flux detection, Jpn. J. Appl. Phys. **38**, 1839 (1999).

[51] R. E. Rottmayer *et al.*, Heat-assisted magnetic recording, IEEE Trans. Magn. **42**, 2417 (2006).

[52] Mark H. Kryder *et al*., Heat assisted magnetic recording, Proc. IEEE, **96**, 1810 (2008).

[53] K. Matsumoto, A. Inomata, and S. Hasegawa, Thermally assisted magnetic recording, FUJITSU Sci. Tech. J. **42**, 158 (2006).

[54] Ikkawi *et al*., Near field optical transducers for HAMR recording for beyond 10 Tb/in^2 densities, J. Nanoelectron. Optoe. **3**, 44 (2008).

[55] W. A. Challener *et al*., Heat-assisted magnetic recording by a near-field transducer with efficient optical energy transfer, Nature Photon. **3**, 220 (2009).

[56] Y. Wang and J-G. Zhu, Understanding field angle for heat assisted magnetic recording via dynamic modeling, J. Appl. Phys. **109**, 07B706 (2011).

[57] D. Karns *et al*., Design and characterization of a media thermal stack for confining lateral thermal heat flow, Proc. Intermag (2008).

[58] W. Peng, Y.-T. Hsia, S. Kursat, and T. McDaniel, Thermo-magneto-mechanical analysis of head-disk interface in heat assisted magnetic recording, Tribology Int. **38**, 588, (2005).

[59] L. Li, P. M. Jones, and Y. T. Hsia, Effect of chemical structure and molecular weight on high-temperature stability of some Fomblin Z-type lubricants, Tribology Lett. **16**, 21 (2004).

[60] D. Weller and A. Moser, Thermal effect limits in ultrahigh-density magnetic recording, IEEE Trans. Magn. **35**, 4423 (1999).

[61] D. Weller *et al*., High K_u materials approach to 100 Gbits/in^2, IEEE Trans. Magn. **36**, 10 (2000).

[62] J.-U. Thiele, L. Folks, M. F. Toney, and D. K. Weller, Perpendicular magnetic anisotropy and magnetic domain structure in sputtered epitaxial FePt (001) $L1_0$ films, J. Appl. Phys. **84**, 5686 (1998).

[63] O. A. Ivanov, L. V. Solina, V. A. Demshina, and L. M. Magat, Determination of the anisotropy constant and saturation magnetization, and magnetic properties of powers of an iron-platinum alloy, Phys. Met. Metallog. **35**, 81 (1973).

[64] P. Ravindran, A. Kjekshus, H. Fjellva, P. James, L. Nordstrom, B. Johansson, and O. Eriksson, Large magnetocrystalline anisotropy in bilayer transition metal phases from first-principles full-potential calculations, Phys. Rev. B. **63**, 144409 (2001).

[65] T.B. Massalski, H. Okamoto, P.R. Subramanian, and L. Kacprzak, *Binary Alloy Phase Diagrams*, ASM International, Ohio (1990).

[66] C. L. Platt, K. W. Wierman, E. B. Svedberg, R. van de Veerdonk, and J. K. Howard, A. G. Roy, and D. E. Laughlin, $L1_0$ ordering and microstructure of FePt thin films with Cu, Ag, and Au additive, J. Appl. Phys. **92**, 6104 (2002).

[67] B. C. Lim, J. S. Chen, and G. M. Chow, Interfacial effects of MgO buffer layer on perpendicular anisotropy of $L1_0$ FePt Films, IEEE Trans. Magn. **42**, 3017 (2006).

[68] S. C. Chen, P. C. Kuo, C. Y. Chou, and A. C. Sun, Effects of Ag buffer layer on the microstructure and magnetic properties of nanocomposite FePt/Ag multilayer films, J. Appl. Phys. **97**, 10N107 (2005).

[69] Y. Xu, J. S. Chen, and J. P. Wang, In situ ordering of FePt thin films with face-centered-tetragonal (001) texture on $Cr_{100-x}Ru_x$ underlayer at low substrate temperature, Appl. Phys. Lett. **80**, 3325 (2002).

[70] J. Chen, C. Sun, and G. M. Chow, A review of $L1_0$ FePt films for high-density magnetic recording, Int. J. Product Development **5**, 238 (2005).

[71] W. B. Byun, K. J. Lee, and T. D. Lee, Effects of SiO_2 addition in FePt on microstructures and magnetic properties on two different MgO substrates, IEEE Trans. Magn. **45**, 2705 (2009).

[72] Y. F. Ding, J. S. Chen, B. C. Lim, J. F. Hu, B. Liu, and G. Ju, Granular $L1_0$ FePt:TiO_2 (001) nanocomposite thin films with 5nm grains for high density magnetic recording, Appl. Phys. Lett. **93**, 032506 (2008).

[73] Y. Peng, J.-G. Zhu, and D. E. Laughlin, $L1_0$ FePt–MgO perpendicular thin film deposited by alternating sputtering at elevated temperature, J. Appl. Phys. **99**, 08F907 (2006).

[74] B. Bian, D. E. Laughlin, K. Sato, and Y. Hirotsu, Fabrication and nanostructure of oriented FePt particles, J. Appl. Phys. **87**, 6962 (2000).

[75] A. Perumal, Y. K. Takahashi, and K. Hono, $L1_0$ FePt–C nanogranular perpendicular anisotropy films with narrow size distribution, Appl. Phys. Express **1**, 101301 (2008).

[76] C. A. Ross, Patterned magnetic recording media, Annu. Rev. Mater. Res. **31**, 203 (2001)

[77] B. D. Terris and T. Thomson, Nanofabricated and self-assembled magnetic structures as data storage media, J. Phys. D: Appl. Phys. **38**, R199 (2005).

[78] B. D. Terris, T. Thomson, and G. Hu, Patterned media for future magnetic data storage, Microsyst. Technol. **13**, 189 (2007).

[79] H. J. Richter, A. Y. Dobin, O. Heinonen, K. Z. Gao, R. J. M. Veerdonk, R. T. Lynch1, J. Xue, D. Weller, P. Asselin, M. F. Erden, and R. M. Brockie, Recording on bit-patterned media at densities of 1 Tb/in^2 and beyond, IEEE Trans. Magn. **42**, 2255 (2006).

[80] K. Sendur and W. Challener, Patterned medium for heat assisted magnetic recording, Appl. Phys. Lett. **94**, 032503 (2009).

[81] Chris Mellor, Toshiba gets bit-patterning between its teeth; HAMR may come too, [online] (July 14, 2011). Available at: http://www.theregister.co.uk/2011/07/14/toshiba_yamamoto_san/

[82] R. Sbiaa and S. N. Piramanayagam, Patterned media towards nano-bit magnetic recording: Fabrication and challenges, Recent Pat. Nanotechnol. **1**, 29 (2007).

[83] J. K. W. Yang and K. K. Berggren, Using high-contrast salty development of hydrogen silsesquioxane for sub-10-nm half-pitch lithography, J. Vac. Sci. Technol. B. **25**, 2025 (2007).

[84] S. Y. Chou, P. R. Krauss, and P. J. Renstrom, Imprint lithography with 25-nanometer resolution, Science, **272**, 85 (1996).

[85] G. M. Schmid *et al*., Step and flash imprint lithography for manufacturing patterned media, J. Vac. Sci. Technol. B, **27**, 573 (2009).

[86] R. M. Metzger *et al*., Magnetic nanowires in hexagonally ordered pores. IEEE Trans. Magn. **36**, 30 (2000).

[87] T. Xu, G. Zangari, and R. M. Metzger, Periodic holes with 10 nm diameter produced by grazing Ar$^+$ milling of the barrier layer in hexagonally ordered nanoporous alumina, Nano Lett. **2**, 37 (2002).

[88] S. Sun, E. E. Fullerton, D. Weller, and C. B. Murray, Compositionally controlled FePt nanoparticle materials, IEEE Trans. Magn. **37**, 1239 (2001).

[89] R. Ruiz, E. Dobisz, and T. R. Albrecht, Rectangular patterns using block copolymer directed assembly for high bit aspect ratio patterned media, ACS Nano **5**, 79 (2011).

[90] I. Bita *et al.*, Graphoepitaxy of self-assembled block copolymers on two dimensional periodic patterned templates. Science, **321**, 939 (2008).

[91] T. Chuanbing, E. M. Lennon, G. H. Fredrickson, E. J. Kramer, and C. J. Hawker, Evolution of block copolymer lithography to highly ordered square arrays, Science, **322**, 429 (2008).

[92] C. A. Ross *et al.*, Si containing block copolymers for self-assembled nanolithography. J. Vac. Sci. Technol. B **26**, 2489 (2008).

[93] B. C. Stipe *et al.*, Magnetic recording at 1.5 Pb m^{-2} using an integrated plasmonic antenna, Nature Photon. **4**, 484 (2010).

[94] R. A. Griffiths, A. Williams, C. Oakland, J. Roberts, A. Vijayaraghavan, and T. Thomson, Directed self-assembly of block copolymers for use in bit patterned media fabrication, J. Phys. D: Appl. Phys. **46**, 503001 (2013).

[95] S. Park *et al.*, Macroscopic 10-terabit-per-square-inch arrays from block copolymers with lateral order. Science, **323**, 1030 (2009).

[96] D. Sundrani, S. B. Darling, and S. J. Sibener, Guiding polymers to perfection: Macroscopic alignment of nanoscale domains. Nano Lett. **4**, 273 (2004).

[97] M. Duwensee, S. Suzuki, J. Lin, D. Wachenschwanz, and F. E. Talke, Simulation of the head disk interface for discrete track media, Microsyst. Technol. **13**, 1023 (2007).

[98] S. N. Piramanayagam *et al.*, Planarization of patterned recording media, IEEE Trans. Magn. **46**, 758 (2010).

[99] G. S. Was, Ion beam modification of metals: Compositional and microstructural changes, Prog. Surf. Sci **32**, 211 (1989).

[100] C. Chappert *et al.*, Planar patterned magnetic media obtained by ion irradiation, Science, **280**, 1919 (1998).

[101] J. Yasumori, Y. Sonobe, S. J. Greaves, and H.Muraoka, Servo-pattern and guard-band formation in perpendicular discrete-track media by ion irradiation, IEEE Trans. Magn. **45**, 3703 (2009).

[102] K. Sato *et al.*, Magnetization suppression in Co/Pd and CoCrPt by nitrogen ion implantation for bit patterned media fabrication, J. Appl. Phys. **107**, 123910 (2010).

[103] C. Choi *et al*., Fabrication and magnetic properties of nonmagnetic ion implanted magnetic recording films for bit-patterned media, IEEE Trans. Magn. **47**, 2532 (2011).

[104] T. Hinoue *et al*., Fabrication of discrete track media by Cr ion implantation, IEEE Trans. Magn. **46**, 1584 (2010).

[105] T. Hinoue, K. Ito, Y. Hirayama, T. Ono, and H. Inaba, Magnetic properties and recording performances of patterned media fabricated by nitrogen ion implantation, J. Appl. Phys. **109**, 07B907(3) (2011).

[107] N. Gaur *et al.*, Ion implantation induced modification of structural and magnetic properties of perpendicular media, J. Phys. D: Appl. Phys. **44**, 365001(9) (2011).

[106] M. S. Martín- González *et al*., Nano-patterning of perpendicular magnetic recording media by low-energy implantation of chemically reactive ions, J. Magn. Magn. Mater. **322**, 2762 (2010).

[108] N. Gaur *et al.*, First-Order reversal curve investigations on the effects of ion implantation in magnetic media, IEEE Trans. Magn. **48**, 2753 (2012).

[109] N. Gaur *et al.*, Lateral displacement induced disorder in $L1_0$ FePt Nanostructures by ion-implantation, Sci. Rep. **3**, 1907(7) (2013).

[110] Z. Sun, D. Li, A. Natarajarathinam, H. Su, and S. Gupta, Large area patterning of single magnetic domains with assistance of ion irradiation in ion milling, J. Vac. Sci. Technol. B **30**, 031803-1 (2012).

[111] S. Kim, S. Lee, J. Ko, J. Son, M, Kim, S. Kang, and J. Hong, Nanoscale patterning of complex magnetic nanostructures by reduction with low-energy protons, Nature Nanotech. **7**, 567 (2012).

CHAPTER 3

Experimental and Computational Techniques

In this chapter, various deposition methods for fabricating samples, lithography techniques and the experimental setup of self-assembly employed for patterning the magnetic samples will be outlined. This will be followed by a brief discussion on the characterization tools used for analyzing the fabricated samples. A section has also been dedicated to the Stopping and Range of Ions in Matter (SRIM) software used for simulating the Gaussian profile of the implanted/embedded ions in the magnetic media.

3.1 Deposition Methods

3.1.1 Sputtering

Sputtering is a discharge process whereby atoms of inert gases, generally argon, are ionized and accelerated towards the target. Momentum transfer between the ions and the target material cause the ejection of neutral target atoms, which then travel to the substrate to form a thin film. The ions necessary for dislodging the target atoms are generated by applying a suitable potential between the substrate (anode) and the target (cathode). Upon ionization, the region between the anode and the cathode comprises a few Ar neutrals, ions, and electrons, which collectively give rise to a weakly charged gas called plasma.

In this project, AJA ATC ORION 5 UHV − an ultra-high vacuum (UHV) magnetron sputtering system employing cryogenic pumps has been used. The targets are arranged in a circular fashion to point towards a common focal point, i.e., the substrate. The magnetron uses a static magnetic field configured parallel to the cathode surface. Secondary electrons, which are released from the cathode due to the bombardment of the ions, are confined by this magnetic field to move in a direction perpendicular to both the electric field (generated between the target and the substrate) and the magnetic field. Therefore, the path of electrons becomes curved and denser plasma is generated closer to the cathode surface. In other words, more ionization of the inert gas atoms occur which enables the possibility of having a high deposition rate at lower gas pressures. Magnetron sputtering is pictorially represented in Figure 3.1.

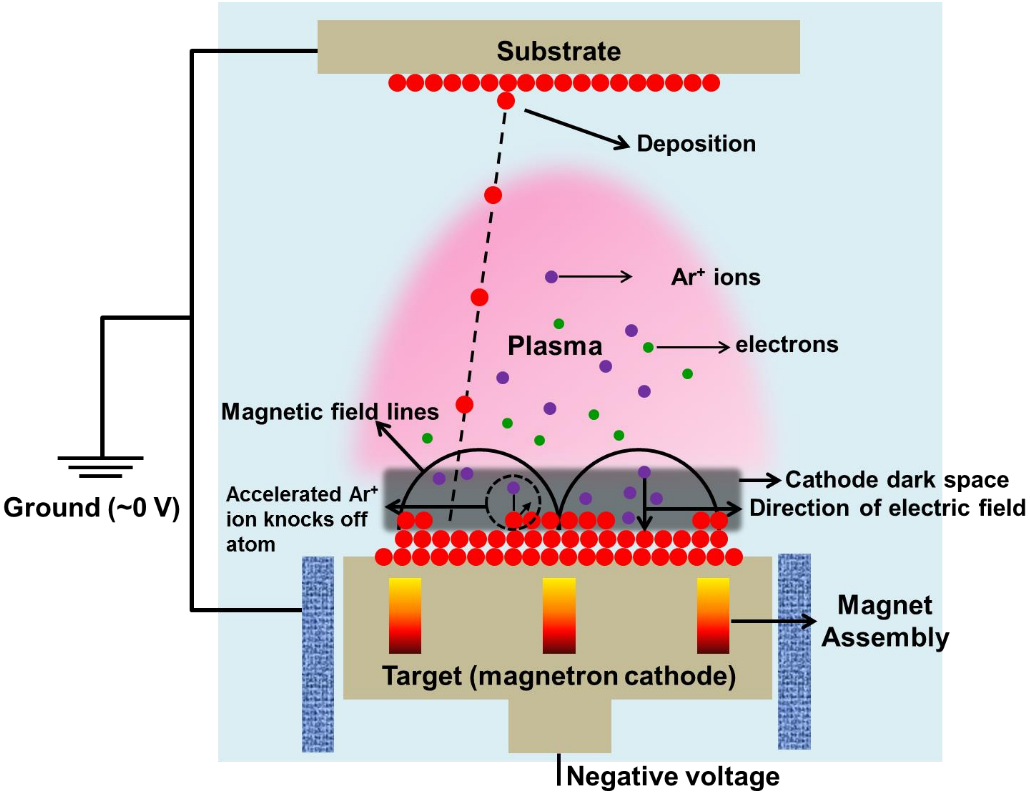

Figure 3.1 Schematic of magnetron sputtering.

The magnetron sputtering tool also provides RF (RF: radio frequency) and DC sputtering (DC: direct current). As the name suggests, in DC sputtering, simple DC power is applied between two electrodes. It is generally used for the deposition of metals. In contrast, RF sputtering in which RF power is applied between two electrodes, is usually used for the deposition of insulating materials. Metals can also be deposited using RF bias. However, the deposition rate will be slower than that obtained using DC power. RF sputtering is also different from DC sputtering due to the fact that the electron with higher mobility than the ions will respond faster to the cyclic changes of the electric field values. Therefore, a negative potential (DC self-bias) arises close to the target electrode which alters the plasma condition in comparison to DC sputtering. A RF generator operating at a frequency of 13.56 MHz is typically used in the sputtering tools. For more details on the sputtering mechanism and the associated physics, one can refer to textbooks on thin film deposition processes [1, 2].

Parameters such as bias applied to the substrate and the target, working pressure, gas flow, and substrate temperature have been adjusted to achieve the desired crystallography of the underlayers (MgO, CrRu) and the $L1_0$ phase of the FePt films investigated in this thesis.

3.1.2 Filtered Cathodic Vacuum Arc (FCVA) Technique

Graphitic and diamond-like properties of carbon films can be tuned by energy of C^+ ions in FCVA system [3]. The plasma is produced in a vacuum chamber by applying a high voltage and high current electric arc on the surface of a graphite target (cathode). The generated plasma consists mostly of carbon ions and the arc current can either be DC or pulse biased.

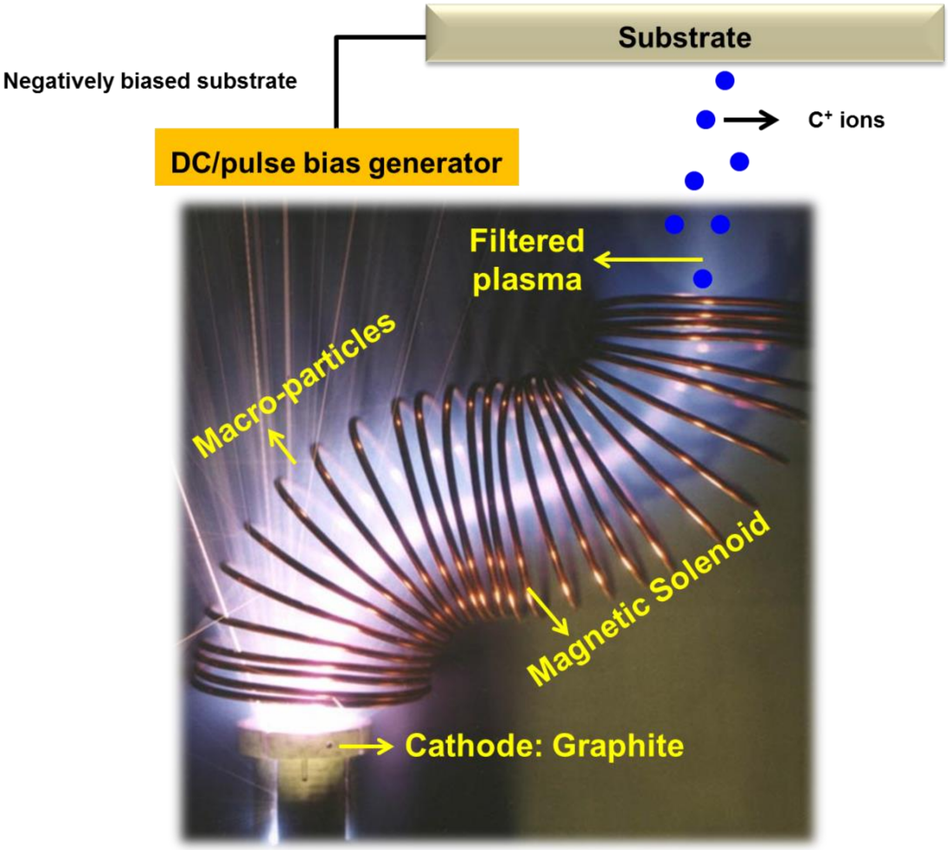

Figure 3.2 Schematic of FCVA technique equipped with S-bent filter.

An initial issue with this technique is the presence of nano- and micro-particles in the plasma which are regarded as defects when depositing a very thin carbon coating. The quality of the plasma is then improved by the usage of magnetic filters [4]. These filters guide the plasma through it. They are magnetic solenoids curved at an angle of 90° with respect to the arc source. The magnetic field causes the C^+ ions to traverse along the shape of the filter. However, because of higher momentum, the undesirable macro-particles are not affected by this field. They continue to move along a straight line and thus get trapped at the curvature of the solenoid. S-bent filters consist of two curves. The first curvature is at an angle of 90° with respect to the arc source and the second is at an angle of 90° with respect to the first curvature. The latter is used to trap any residual macro-particles.

The fully ionized plasma from the S-bent filter has energy of ~20 eV. However, the energy of the C^+ ions can be varied to alter the properties of the carbon films. The ions are accelerated to the substrate surface by applying a negative bias voltage (either by DC or pulsed biasing) to the substrate. By changing the biasing, the energy of the ions leaving the S-bent filter can be altered. All the features of the FCVA technique equipped with the S-bent filter have been pictorially presented in Figure 3.2.

3.2 Patterning Techniques

3.2.1 Solvent vapor annealing for achieving self-assembly of block copolymer

Self-assembly comprises immiscible organic-organic blocks which can micro-phase separately into a variety of morphologies depending on the composition of each block. The self-assembly of block copolymers depends on the Flory-Huggins parameter – defined as a degree of incompatibility between the blocks governed by interaction energies per repeat unit in the copolymer [5]. The self-assembly process can be driven by solvent vapor annealing. In solvent vapor annealing, the vapor of a solvent or solvent mixture is used to depress the glass transition temperature of the polymer chains to make them more mobile and eventually phase separate [6]. The schematic of the self-assembly process and the setup is shown in Figure 3.3. More details on the mechanism and implication of solvent vapor annealing are discussed in Chapter 7. The block copolymer investigated to create masks for patterning magnetic nano-structures was polystyrene-b-polydimethylsiloxane (PS-*b*-PDMS). As shown in Figure 3.3, a few milliliters of solvent/solvent mixture are put into the glass chamber. A glass slide is balanced on the kinks inside the chamber on which samples are loaded. A lid is then placed on the chamber and sealed using a parafilm film. A saturated vapor pressure is created within the chamber. The samples are kept inside this sealed chamber for a suitable period of time to obtain self-assembly over a large area. The process is carried out inside the fume hood to ensure regulated air flow to maintain a uniform temperature of the chamber assembly.

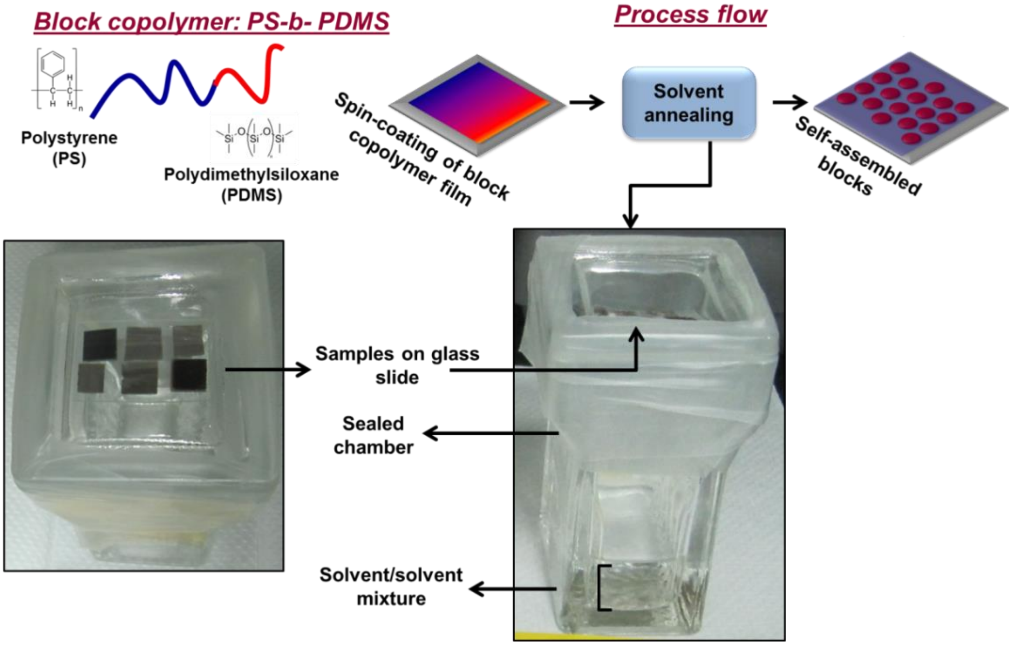

Figure 3.3 Schematic of the self-assembly process and images of the setup designed to carry out solvent vapor annealing.

3.2.2 Electron Beam Lithography (EBL)

EBL is a high resolution lithographic process that uses a focused beam of electrons to pattern custom shapes and patterns on substrates coated with electron-sensitive resist. Electron lithography offers higher patterning resolution than other optics-based lithography techniques because of the shorter wavelength possessed by the electrons. For example, in accordance with Equation 3.1, the wavelength of an electron possessing energy of 100 keV is 4 × 10^{-3} nm, thereby making it possible to pattern sub-100 nm patterns. In other words, it is not restricted by diffraction. It is limited by the aberrations present in the optical design of the system. It is a mask-less patterning technique and requires the electron beam to scan the entire substrate surface in a serial manner which, in turn, makes it time-consuming. A typical EBL system consists of an electron source (gun) emitting the electrons; a column with electromagnetic lenses to focus and deflect the electron beam; a stage that controls the mechanical motion of the wafer under the electron beam; and a computer system that monitors various functions of this equipment [7].

$$\boldsymbol{\lambda} = \frac{\mathbf{h}}{\sqrt{\mathbf{m}\,(\mathbf{0.5} \times \mathbf{E})}} \qquad \text{Equation 3.1}$$

where $\mathbf{h}$ is the Planck’s constant, and $\mathbf{m}, \mathbf{E}, \boldsymbol{\lambda}$ are the mass, energy and wavelength of the electron, respectively.

Electron sensitive resists can be of two types – positive resist (in which the exposed resist region becomes soluble in an appropriate solvent termed as ‘developer’) and negative resist (in which the exposed region becomes further cross-linked; thus, it is the unexposed region which is removed by the developer). Depending on the electron dose, as defined by Equation 3.2, the solubility of the resist can be controlled and the pattern quality can be fine-tuned accordingly [8].

$$\mathbf{D} = \frac{\mathbf{T} \times \mathbf{I}}{\mathbf{A}} \qquad \text{Equation 3.2}$$

where $\mathbf{D}$ is the dose and is defined as the number of electrons striking a unit area, $\mathbf{I}$ is the electron current, $\mathbf{T}$ is the exposure (dwell) time, and $\mathbf{A}$ is the exposed area.

In this project, an Elionix ELS-7000 electron-beam lithography system operating at 100 kV has been used to pattern hydrogen silsesquioxane (HSQ; negative resist) in a sub-20 nm regime. The patterning process employing EBL is represented in Figure 3.4.

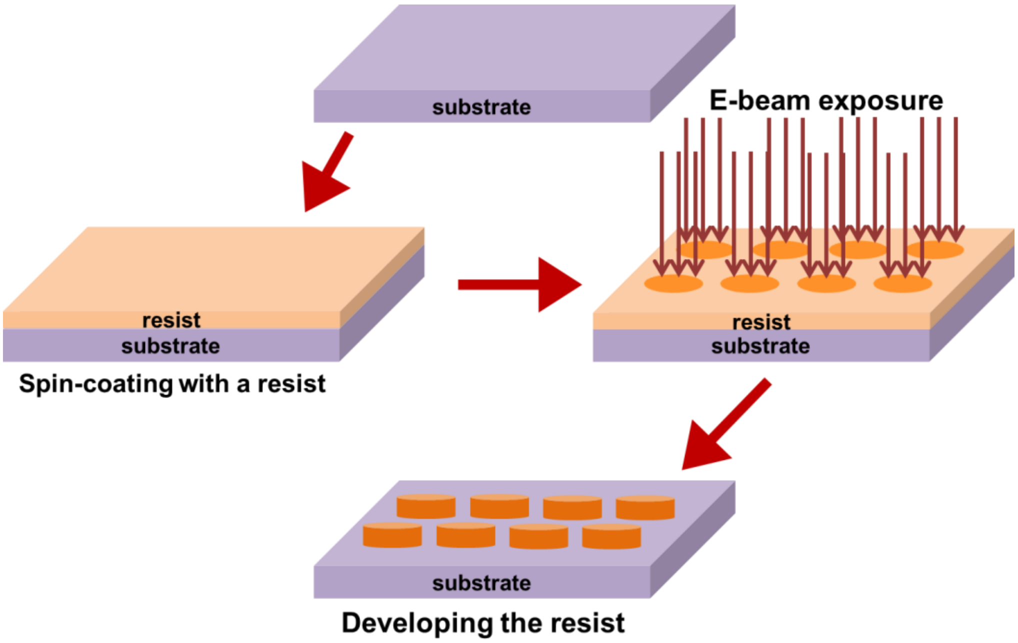

Figure 3.4 Various steps of patterning a resist using an EBL tool.

3.3 Characterization Methods

3.3.1 Surface (or topography) characterization

3.3.1.1 Field emission − Scanning electron microscopy (FE−SEM)

The SEM uses a focused beam of high-energy electrons to generate a variety of signals at the surface of solid specimens. The signals that are obtained from electron-sample interactions reveal information about the specimen's external morphology and texture. In a SEM, electrons with sufficient kinetic energies are accelerated from an electron gun towards the sample surface to be imaged. The interaction of the electrons with atoms present on the surface of the sample produces signals which include secondary electrons, backscattered electrons, Auger electrons, cathodoluminescence, and x-rays. The secondary electrons are collected by a detector present near the sample and are used for reconstructing the morphology and topography of the sample. The backscattered electrons are used for obtaining compositional maps of a sample. The different contrasts seen in the image correspond to the various phases present in the sample [9].

A JEOL JSM6700F FE-SEM was used to acquire high resolution images of as-prepared as well as self-assembled PS-*b*-PDMS structures. A field emission gun (FEG) is used in which a sharp Müller-type emitter is at a negative potential of a few kV relative to a nearby electrode. Therefore, the potential gradient at the emitter surface leads to field electron emission [10]. Emitters can be made of single crystal W or LaB_6 with tips of radius ~100 nm. Schottky type emitters, based on thermionic emission, can also be used. In these emitters, ZrO_2 is coated on the tips of the W tips. With the use of FEG, enhanced electron brightness at a lower accelerating voltage, higher spatial resolution, and improved SNR is obtained. A resolution of ~1 nm can be acquired using 15 kV in JEOL JSM6700F FE-SEM. A schematic of the SEM is shown in Figure 3.5. Apart from the FEG and secondary electron detector, electromagnetic (condenser and objective) lenses are used to focus the imaging electron beam at a specific area on the sample.

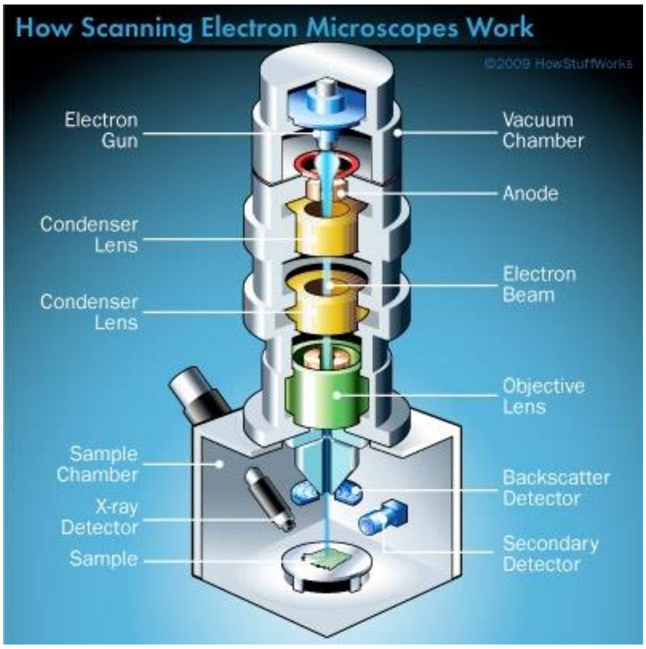

Figure 3.5 Schematic of SEM [11].

3.3.1.2 Atomic force microscopy in tapping mode (AFM)

A scanning probe microscope can be operated in two different modes – atomic force microscopy-mode (AFM) and magnetic force microscopy-mode (MFM). Since the MFM mode is used for investigating the magnetic domains of a sample, it has been discussed along with other measurement techniques used for characterizing magnetic materials in Section 3.3.2.2. The AFM mode is discussed below.

The AFM comprises of a setup in which a cantilever with a sharp tip at its end is used for scanning the sample surface. The cantilever is generally silicon or silicon nitride with the tip having a radius of curvature in the order of nanometers. When the tip is placed close to the sample surface, short-range Van der Waals forces between the tip and the sample cause the cantilever to deflect in accordance with the Hooke's law [12]. A laser spot is incident on the top surface of the cantilever. The spot is reflected off into an array of position sensitive photodiodes upon the angular displacement of the cantilever. The change in the location of the laser spot at the photodiode detector is then used for measuring the extent of the cantilever’s deflection and, in turn, maps the sample’s topography. Since there is a probability of collision of the tip which is scanning at a constant distance with the surface, a feedback mechanism for adjusting the tip-to-sample separation to maintain a constant force between the two is employed. The sample is mounted on a scanner of three piezo crystals which is connected to the feedback unit and monitors the sample’s movement in the x, y and z directions.

In the tapping mode, in order to avoid any damage to the sample, the AFM tip comes into contact with the sample surface intermittently. A piezo actuator attached to the cantilever and operating at a certain drive frequency causes the tip to oscillate at its resonant frequency. Depending on the tip-sample separation, the deflection amplitude of the cantilever changes and is converted into electric signals which are useful for reconstructing the sample surface. An electronic servo connected to the piezoelectric actuator controls the height of the cantilever above the sample surface. The servo regulates the tip-sample distance to maintain certain cantilever oscillation amplitude as the cantilever travels over the sample [13]. The mechanism of tapping mode AFM is shown in Figure 3.6. A Digital Instruments Nanoscope® IV atomic force microscope (AFM) was used in the project to study the surface roughness of various media samples. Conducting antimony doped silicon tips with resonant frequency ranging between 230-410 kHz is used.

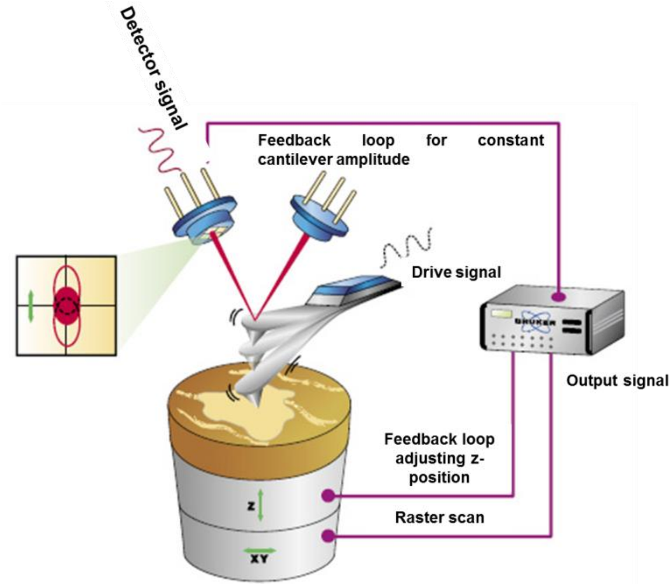

Figure 3.6 Schematic representation of tapping mode-AFM [14].

3.3.2 Magnetic Characterization

3.3.2.1 Vibrating sample magnetometer (VSM)

Invented by Simon Foner in 1955, VSM is used for measuring magnetic properties of materials as a function of the magnetic field [15]. The VSM is schematically shown in Figure 3.7. It comprises an electromagnet driven by a DC power supply to generate magnetic field. A sample placed in the magnetic field is made to vibrate using a control unit. Induction coils are placed near the vibrating sample. The continuously changing flux through the coil, arising from the vibrating sample, then produces a signal voltage. The measured voltage is a product of the material's magnetic moment, amplitude of vibration, frequency of vibration, and the sensitivity factor of the coils being used. Therefore, the behavior of the magnetic moment with respect to the applied field can easily be extracted from the output voltage/measurement [16].

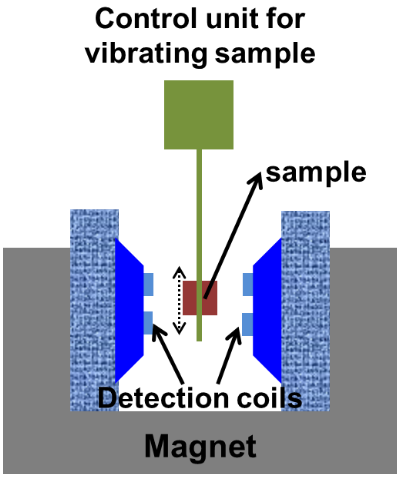

Figure 3.7 VSM represented schematically.

In this project, the VSM utility function provided in the Quantum Design physical property measurement system (PPMS) was used to measure the hysteresis loops and saturation magnetization of the FePt samples. The instrument facilitates the usage of external fields extending up to 9T.

3.3.2.2 Magnetic Force Microscopy (MFM)

In MFM, a magnetized AFM tip is initially used in the tapping mode to reconstruct the topography of the sample surface. “Lift Mode” is then used in which the tip retraces the profile of the surface from a fixed height over the sample surface − slightly higher than the tip-sample separation used for mapping the topography. The resulting long-range interaction between the magnetic sample and the magnetized AFM tip reproduces the magnetic field distribution within the sample, independent of its topography. As mentioned in Section 3.3.1.2, the piezo actuator causes the tip cantilever to oscillate at its resonant frequency in the tapping mode. In the lift mode, the resonant frequency shifts by a small amount whenever a variation is sensed in the magnetic field strength arising from the sample.

The change in oscillation frequency of the cantilever is detected by measuring its phase of oscillation with respect to the drive frequency of the piezo actuator [17]. The working principle of MFM is presented in Figure 3.8.

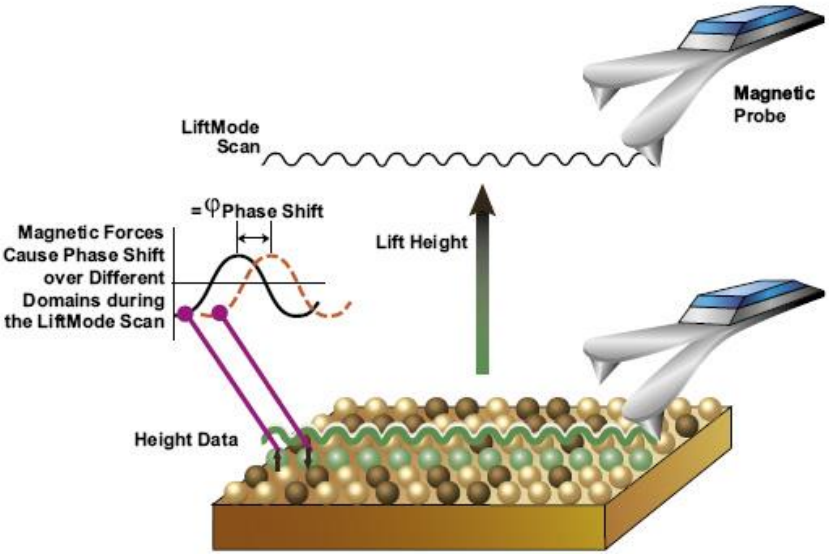

Figure 3.8 Working principle of MFM [18].

A Veeco® scanning probe microscope, operating in MFM mode, was used for studying FePt samples. Conducting antimony doped silicon tips coated with cobalt from VEECO were used. The resonant frequency lies between 60 and 100 kHz. The samples are AC demagnetized before subjecting them to MFM. Alternate positive and negative fields perpendicular to the sample surface are applied. In the beginning, a maximum field value of 20 kOe is used which is then reduced continuously after the completion of a cycle of positive and negative fields in steps of 1 kOe till zero field value is reached. In the AC demagnetized state, information of the sample's magnetic field distribution in the as-deposited state is extracted. MFM can be used for imaging domains in patterned structures provided that the pattern size is >30 nm. This is because the typical resolution of the MFM is limited to ~30 nm [19].

3.3.3 Structural Characterization

3.3.3.1 Transmission electron microscopy (TEM) equipped with electron energy loss spectroscopy (EELS)

In a TEM, electrons are transmitted through an ultra-thin sample. Depending on the interaction of the samples with the electrons passing through them, a grey-scale image is produced on a fluorescent screen. The brighter appearing regions are the ones through which a large number of electrons have passed. On the other hand, the darker appearing regions represent denser composition of the materials which restrict the passage of electrons through them [20]. The image resolution depends on the velocity of the electron beams. High electron velocity leads to shorter wavelengths and, therefore, detailed reconstruction of the specimen surface is enabled. A spatial resolution of ~0.2 nm can be achieved using a TEM [9]. This mode of operation is known as bright field imaging.

Similar to SEM, the TEM system also comprises field emission or thermionic electron gun (using energies of ~100-400 keV), electromagnetic lenses, condensers, specimen stage, and a fluorescent screen upon which the transmitted electrons are incident after passing through the sample, all inside a vacuum chamber [9]. The TEM sample preparation involves dimple grinding the sample followed by an ion milling process to create wedges. It is these thin edges which are used for TEM imaging [21].

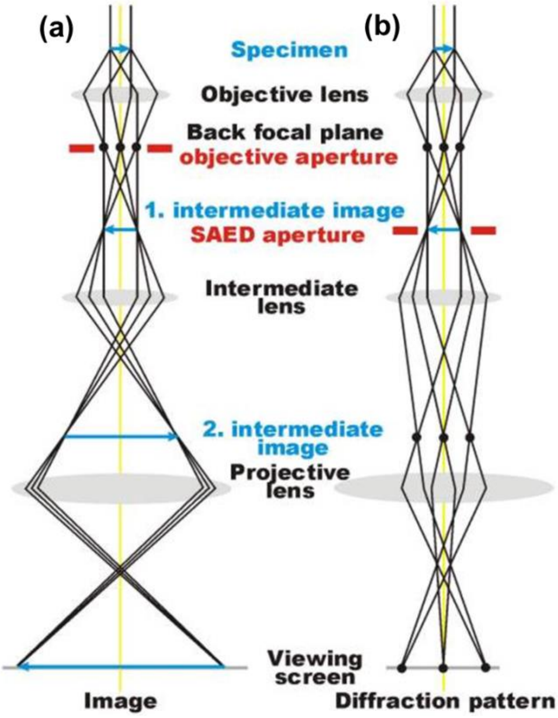

Figure 3.9 TEM operating in (a) imaging mode and (b) SAED mode [22].

Another function of TEM which can be used is selected area electron diffraction (SAED). The atoms present in the specimen can cause the diffraction of the electrons traversing through the sample. By inserting a selected area aperture into the beam path, a series of spots can be attained on the image screen. Each of these spots represents a diffraction condition corresponding to the crystal structure of the specimen. SAED is useful for identifying the crystal structure and structural defects present in a region as small as a few hundred nanometers. A detailed study on SAED can be found in [23]. The ray paths of the electrons in a TEM used in both imaging and obtaining SAED patterns are shown in Figure 3.9.

Structural analysis of FePt samples was performed using a Phillips CM300 FEG−TEM. The TEM operating at 300 kV equipped with EELS was used to analyze the composition of individual FePt grains. The principle of EELS is discussed briefly in the following few sentences. A number of electrons are inelastically scattered when electrons are incident upon a specimen surface. They lose a certain amount of energy which corresponds to their interaction with a particular element in the periodic table. By analyzing this loss in the transmitted electron energy, with a spectroscope attached under the electron microscope, elemental composition and distribution of a small region (~100 nm in size) can be mapped effectively [24].

3.3.3.2 X-ray diffraction (XRD)

The schematic of XRD is shown in Figure 3.10. X-ray source is incident on a sample surface. Both the source and the detector move in a way such that the source beam incident at an angle θ with respect to the film surface makes an angle 2θ with respect to the diffracted beam. The x-ray interaction with the sample causes the beam to diffract, depending on the crystal plane of the atoms in the sample. The condition for a diffraction (peak) to occur is defined by Bragg’s law and can be simply written as:

$$\mathbf{2d\sin\theta = n\lambda} \qquad \text{Equation 3.3}$$

where $\mathbf{d}$ is the spacing between the crystal planes, $\boldsymbol{\lambda}$ is the wavelength of the incident x-ray and $\mathbf{n}$ is an integer.

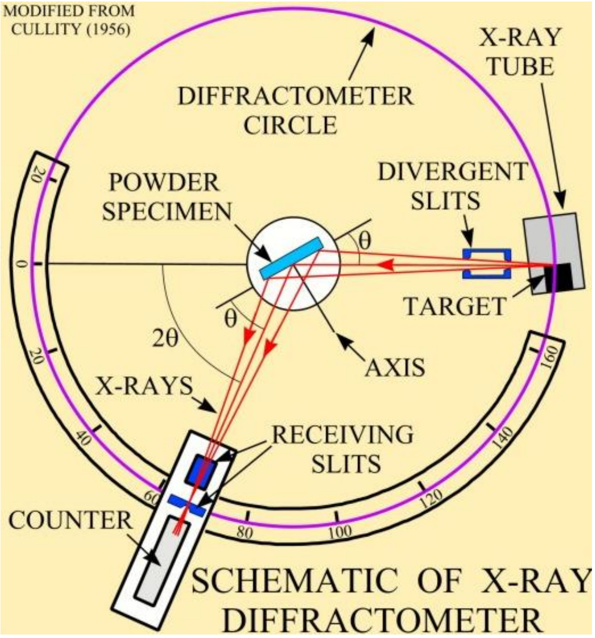

Figure 3.10 Principle of XRD following Bragg's law [25].

The diffraction pattern shows scattering peaks corresponding to the various spacings in the crystal lattice [26]. The intensity of the diffracted beam is detected at each 2θ value in the scanned range defined by the user. The positions and intensities of the peaks from the intensity versus 2θ plot are used for identifying the underlying crystallographic structure (or phase) of the material. The diffraction peaks are indexed and phases are determined by comparing the experimental peak position with the standard database from the Joint Committee on Powdered Diffraction Standard (JCPDS). XRD was performed on the media samples using a Bruker D8 general area detector diffraction system (GADDS) equipped with a Cu-K_{α} source.

Rocking curve measurements employing the XRD setup were carried out to investigate the dispersion of a particular plane around the film's normal direction. The detector was initially fixed at an angle of 2θ with respect to the incident beam. The rocking curve of the texture peak at an angle 2θ was then calculated. Then the angle between the incident beam and the normal direction of the film plane was scanned around the value of θ. The full-width at half-maximum ($\Delta\theta_{50}$) determined from the rocking curve provides an indication of the quality of the texture. The smaller the $\Delta\theta_{50}$ value, the better is the quality of the texture.

3.3.3.3 Time of Flight – Secondary Ion Spectroscopy (ToF-SIMS)

ToF-SIMS is a technique to analyze the composition and distribution of atoms, molecules and chemical structures on surfaces. However, it can be employed to achieve depth profiles of multi-layered samples.

A pulse of ions (primary ion gun source) is incident on the specimen to remove atoms and molecules from the surface. Along with these atoms and molecules, a few ionized species are also produced. These secondary ions generated are accelerated into a spectrometer. All the entities are accelerated using a constant field, and they depart from the same location in the sample at the same time. They travel through a specific distance and reach the ion detection and counting unit. The lighter ones arrive at the detection unit before the heavier ones. The “time-of-flight” of an ion is proportional to the square root of its mass. Therefore, all the different masses are separated during the flight and can be detected independently. It should be noted that the next pulse of primary ions cannot be initiated until the secondary ions of the first pulse have cleared the analyzer. This is so because the slower moving heavy ions generated from the first pulse will be overtaken by the faster light ions of the second pulse. However, this time interval between consecutive pulses can be used for charge neutralization and another low energy ion beam can be used to sputter off some material when depth profiling of the samples is being carried out [27].

ToF-SIMS provides a depth resolution of <1 nm and a spatial resolution <100 nm. Since charge neutralization is utilized, the detection of insulating materials can be easily carried out. ToF-SIMS from ION-TOF GmbH was utilized in this project to inspect the changes in composition of the FePt films along the depth when exposed to C^+ ion bombardment. Bi was the primary ion gun source incident on the sample at energy of 25 keV. On the other hand, Cs^+ ions accelerated at a lower energy of 1 keV were used for sputtering off the film.

3.4 Stopping range of ion in matter (SRIM) − Transport of Ions in Matter (TRIM)

SRIM is a group of computer programs which interprets the interaction of ions with other atoms [28]. TRIM forms the fundamental part of SRIM. Statistical algorithms, based on a Monte Carlo simulation method, i.e., binary collision approximation, are used for efficient computation of ion-atom collisions. Two important features of this program are: (a) analytical determination of atom-atom collisions, and (b) using the concept of a free-flight-path between collisions such that only significant collisions are evaluated. This program effectively provides a quantitative evaluation of ions losing energy into matter (or target) followed by their slowing down, coming to rest and final distribution in the target.

The program requires the user to provide input parameters such as –

- Species to be implanted
- Implantation energy
- Angle of the incoming ion
- Constituents, composition and thickness of the target material
- In addition, the number of ion species upon which the simulation will be performed can also be decided by the user. Clearly, the higher the number of ions, the higher is the accuracy.

In this study, low energy embedment (<500 eV) of C^+ ions in FePt thins films have been simulated using TRIM. Each simulation run comprised 99999 C^+ ions. The ions bombarding the surface of a material get embedded into the target after traversing a certain depth. This process is called direct implantation. Simultaneously, some bombarding ions may transfer significant energy to the target atoms which can move and create collision cascades. Such collision cascades may give rise to further replacement collisions, creation of vacancies and yield sputtering of atoms from the target volume [29]. Depending on the input parameters, intermixing of the foreign species with the target layers can lead to modification of target properties. Such a scenario is presented and the consequences are discussed in the later chapters of this thesis.

The energy loss mechanism experienced by these ions varies depending on the atomic number and energy of the ion species. Ions undergoing nuclear elastic collisions (or nuclear stopping) transfer energy in the form of translatory motion to the target atom as a whole. High energy losses and lattice disorder are highly likely to occur. Such nuclear stopping is prominent for heavier ions and lower energy. In contrast, electron inelastic collision (or electron stopping) results in the navigation ion exciting atomic electrons. Characterized by minimal lattice damage, this type of collision is dominant for lighter ion species and higher energy. Based on the scaling theory of ion-atom collision put forth by Lindhard, Scharff and Schiott, SRIM has also been designed to generate similar individual atom-atom stopping powers [30-32].

References

[1] D. L. Smith, *Thin Film Deposition,* Mc-Graw Hill Professional (2001).

[2] K. Seshan, *Handbook of Thin-Film Deposition Processes and Techniques: Principles, Methods, Equipment and Applications,* William Andrew Publishing/Noyes (2002).

[3] A. Anders, *A Brief History of Cathodic Arc Coating, in Cathodic Arcs: From Fractal Spots to Energetic Condensation*, Springer: New York (2009).

[4] A. Anders, Approaches to rid cathodic arc plasmas of macro- and nanoparticles: A review, Surf. Coat. Tech. **120-121**, 319 (1999).

[5] Y. Mai and A. Eisenberg, Self-assembly of block copolymers (Tutorial Review), Chem. Soc. Rev. **41**, 5969 (2012).

[6] Z. Lin, D. H. Kim, X. Wu, L. Boosahda, D. Stone, L. Larose, and T. P. Russell, A rapid route to arrays of nanostructures in thin films, Adv. Mater. **14**, 1373 (2002).

[7] P. Rai-Choudhary, *Handbook of Microlithography, Micromachining, and Microfabrication: Microlithography,* SPIE Press (1997).

[8] N. W. Parker, A. D. Brodie, and J. H. McCoy, High-throughput NGL electron-beam direct-write lithography system, Proc. SPIE, **3997**, 713 (2000).

[9] R.F. Egerton, *Physical Principles of Electron Microscopy: An Introduction to TEM, SEM, and AEM,* Springer (2005).

[10] J. R. A. Cleaver, Field emission guns for electron probe instruments, Int. J. Electron. **38**, 513 (1975).

[11] J. Atteberry, How Scanning Electron Microscopes Work [online]. Available at http://science.howstuffworks.com/scanning-electron-microscope2.htm

[12] B. Cappella and G. Dietler, Force-distance curves by atomic force microscopy, Surf. Sci. Rep. **34**, 1 (1999)

[13] Q. Zhong and D. Innlss, Fractured polymer/silica fiber surface studied by tapping mode atomic force microscopy, Surf. Sci. Lett. **290**, L688 (1993).

[14] Bruker, Tapping Mode AFM [online] (2011, June 1). Available at: http://blog.brukerafmprobes.com/2011/06/tapping-mode-afm/

[15] S. Foner, Versatile and Sensitive Vibrating-Sample Magnetometer, Rev. Sci. Instrum. **30**, 548 (1995).

[16] D. Speliotis, *Getting the Most From Your Vibrating Sample Magnetometer*, ADE Technologies, Inc., Newton MA.

[17] I. V Yaminsky and A.M. Tishin, Magnetic force microscopy, Russ. Chem. Rev. **68**, 165 (1999).

[18] Bruker, Magnetic Force Microscopy – MFM [online] (2011, June 1). Available at: http://blog.brukerafmprobes.com/2011/06/magnetic-force-microscopy-mfm/

[19] L. Abelmann *et al.*, Comparing the resolution of magnetic force microscopes using the CAMST reference sample, J. Magn. Magn. Mater. **190**, 135 (1998).

[20] B. Fultz and J. Howe, *Transmission Electron Microscopy and Diffractometry of Materials*, Springer (2007).

[21] TEM Sample Preparation for Beginners: Dimple grinding [online]. Available at: http://www.ims.uconn.edu/~micro/Dimple%20Grinding2.pdf

[22] Electron microscopy [online] (2012, May 14). Available at: http://www.microscopy.ethz.ch/TEMED.htm

[23] G. S. Y. Yeh and P. H. Geil, Selected-area small-angle electron diffraction, J. Mater. Sci. **2**, 457 (1967).

[24] D. A. Muller, D. J. Singh, and J. Silcox. 1998 Phys. Rev. B, **57**, 8181 (1998).

[25] Modified from Cullity (1956). Available at: http://pubs.usgs.gov/of/2001/of01-041/htmldocs/images/xrdschem.jpg

[26] B. E. Warren, *X-Ray Diffraction*, Addison-Wesley Publishing Company (1969).

[27] J. C. Vickerman and D. Briggs, *ToF-SIMS: Materials Analysis by Mass Spectrometry*, Surface Spectra, Manchester and IM Publications, Chichester (2013).

[28] J. F. Ziegler, Stopping of energetic light ions in elemental matter, J. Appl. Phys. 85, 1249 (1999).

[29] R.E. Stoller, M.B. Toloczko, G.S. Was, A.G. Certain, S. Dwaraknath, and F.A. Garner, On the use of SRIM for computing radiation damage exposure, Nucl. Instr. Meth. Phys. Res. B. **310**, 75 (2013).

[30] J. Lindhard, M. Scharff, and H. E. Schiøtt, Range concepts and heavy ion ranges (notes on atomic collisions, II), Mat. Fys. Medd. Dan. Vid. Selsk. **33**, 1 (1963).

[31] J. W. Mayer, L. Eriksson, and J. A. Davies, *Ion Implantation in Semiconductors*, Academic Press, New York and London (1970).

[32] Particle interactions with matter, [online]. Available at: http://www.srim.org/

CHAPTER 4

Spacer-less, granular and well-ordered $L1_0$ FePt media for HAMR

4.1 Motivation

$L1_0$ phase FePt is now a widely researched storage medium candidate for achieving ultra-high density by employing heat-assisted magnetic recording (HAMR). These ordered films, with a large magneto-crystalline anisotropy (K_u ~ 7 x 10^7 ergs/cc) [1], permit the fabrication and recording of thermally stable grains of dimensions ~3-4 nm in diameter. However, there are key technological challenges which need to be solved prior to its application in hard disk drives (HDD).

Apart from reduction of the $A1$-$L1_0$ phase transformation temperature, simultaneous attainment of well-ordered $L1_0$ FePt films and smaller-sized grains is necessary. Ion irradiation [2] and use of underlayers (such as CrMo, RuAl, MgO and Pt among others) have shown better quality (001) FePt texture [3-6]. On the other hand, addition of spacer materials (such as B, BN and C among others) has led to smaller, decoupled and uniform-sized grains [7-9]. It is, however, not unforeseen that the incorporation of such ternary elements into the $L1_0$ FePt recording film interferes adversely with the layer's magnetocrystalline anisotropy, thereby degrading its magnetic properties [9, 10].

The motivation of this particular work has been to grow granular and well-ordered $L1_0$ FePt media without the addition of any spacer materials into the films –

- Displaying coercivities > 20 kOe, and
- Having grain sizes approaching sizes <20 nm, both of which should be achieved concurrently.

To put it briefly, in order to achieve spacer-less $L1_0$ FePt media, an optimal volume of helium, ranging from 0.5 to 1%, was introduced into the argon environment in the sputtering chamber during deposition. The effect of change of the carrier gas composition on the magnetic and structural properties of the $L1_0$ phase FePt granular media was studied. Unlike the FePt films doped with spacer materials showing a trade-off between smaller grain sizes and higher out-of-plane coercivity, the $L1_0$ phase FePt films deposited in the argon-helium (Ar–He) environment displayed a substantial increase in the out-of-plane coercivity accompanied by reduction in grain size. This was attributed to the improvement in chemical ordering and nucleation kinetics of the growing FePt film due to the presence of helium in the sputtering gas mixture.

4.2 Experimental Details

The structure of the FePt media stack used in this study is shown in Figure 4.1. The FePt samples were prepared in a sputtering system maintained at a base pressure of ~5×10^{-9} Torr. 5 nm thick FePt films were grown on CrRu (24 nm) / MgO (3 nm) layers pre-deposited on a 0.5 mm thick glass substrate. The CrRu layer was grown at 400 °C to provide a (002) texture for the heteroepitaxial growth of (001) FePt. The MgO layer was introduced as a buffer layer between CrRu and FePt at 400 °C to prevent the diffusion of chromium into the magnetic recording layer. It further improved the crystallographic texture of the FePt layer. The FePt layer was deposited at 600

°C. The alloy target used for depositing the FePt film consisted of both Fe and Pt atoms in equal proportion. The alloy composition and sputtering conditions, chosen for fabricating the FePt media stack, were based on the previous work done by the group members [10, 11].

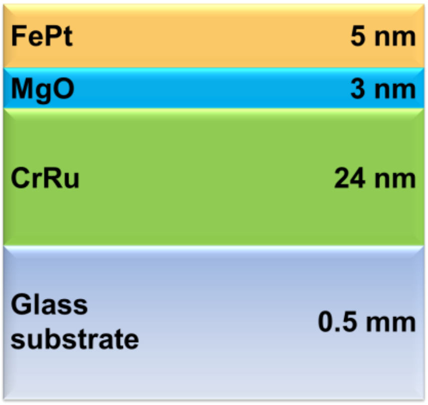

Figure 4.1 Schematic of FePt media stack used in the study.

Three sets of FePt films were grown using different carrier gas compositions. Table 4.1 shows the sputtering gas mixture used for each layer in the media stack. These values were based on the gas flow rates used in the sputtering chamber. Helium is pumped out from the sputtering chamber at a slower rate than argon. Therefore, the effective volume of helium was expected to be higher than that calculated in Table 4.1. However, it can be said that the increase was marginal since the addition of helium did not affect the deposition rate of the target atoms. The deposition rates calibrated for the targets were approximately the same for argon and argon-helium sputtering mixtures. All the other parameters such as gas pressure, deposition temperature and film thicknesses were kept constant during the study. The sputtering gas mixture composition was the only variable.

Set number	**Layers in the FePt recording media stack**					
	FePt		MgO		CrRu	
	Gas mixture	Pressure (mTorr)	Gas mixture	Pressure (mTorr)	Gas mixture	Pressure (mTorr)
A	Ar	3	Ar	1.5	Ar	1.5
B	Ar–He (0.5%)	3	Ar–He (0.5%)	1.5	Ar	1.5
C	Ar–He (1%)	3	Ar–He (1%)	1.5	Ar	1.5

Table 4.1 Gas mixtures and pressures used for depositing different FePt media stacks. The percentage included in the brackets indicates the volume percentage of He used in the experiment. The number was estimated by taking into account the relative flow rates (expressed in standard cubic centimeters per minute) of Ar and He in the chamber.

A systematic preliminary investigation to study the influence of helium on each layer had revealed that better magnetic properties were obtained when both MgO and FePt layers were grown in an Ar–He gas mixture. Table 4.2 summarizes the experiment carried out to arrive at the abovementioned inference. The table displays the out-of-plane coercivities of three sets of FePt samples – Set I in which only FePt was grown in Ar–He (0.5%), Set II in which the MgO and FePt layers were deposited in Ar–He (0.5%), and Set III in which all the three layers were grown in Ar–He (0.5%). Set II (~19 kOe) exhibited a considerable increase in the out-of-plane coercivity compared to Set I (~16 kOe). However, no major improvement in the magnetic properties of Set III (~19.5 kOe) was observed.

Layer used in the stack	**Carrier gas composition used for each layer**		
	Set I	**Set II**	**Set III**
FePt	Ar–He (0.5%)	Ar–He (0.5%)	Ar–He (0.5%)
MgO	Ar	Ar–He (0.5%)	Ar–He (0.5%)
CrRu	Ar	Ar	Ar–He (0.5%)
OOP (kOe)	16	19	19.5

Table 4.2 Gas mixtures used for each layer in the preliminary investigation to determine the appropriate recipe to fabricate the FePt media stack for mapping and understanding the influence of increasing helium volume on the FePt magnetic and structural properties. The out-of-plane coercivities (OOP) for each of the sets have also been provided.

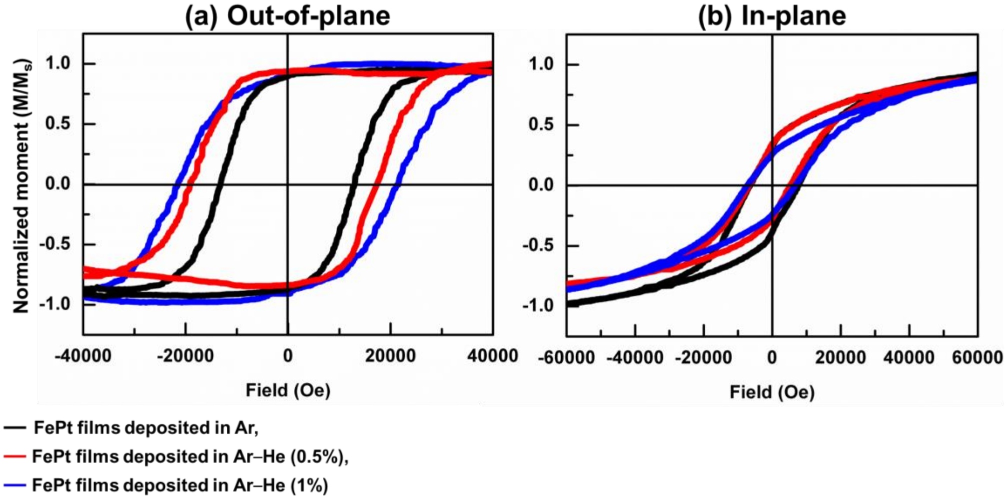

Figure 4.2 Out-of-plane and in-plane hysteresis loops of *$L1_0$* FePt films grown in Ar, Ar–He (0.5%) and Ar–He (1%).

4.3 Results: Characterizing the FePt films grown in Ar and Ar–He (0.5-1%)

Figure 4.2 provides a comparison of the out-of- and in-plane hysteresis loops of the FePt samples grown in the Ar and Ar–He (0.5-1%) environment. Set B exhibited an increment of ~17% in the out-of-plane coercivity (17.5 kOe) when compared to the reference Set A (15 kOe). Similarly, Set C also displayed an increase of ~46% in the out-of-plane coercivity (22 kOe) in comparison to reference Set A (15 kOe). The in-plane coercivities for all the three sets A, B and C were approximately equal (~6.5 kOe). These three sets were fabricated thrice and magnetic measurements were performed on all of them each time. They all showed consistent results. The increase in the out-of-plane coercivity without any considerable change in the in-plane coercivity observed for sets B and C indicated a gradual enhancement in the $L1_0$ ordering of the FePt layer with increasing helium percentage. Saturation magnetization (M_s) for the sets A, B and C were ~900, ~1000 and ~1100 emu/cc, respectively. The anisotropy field (H_k) was also measured for each sample set by finding out the intersection point of the out-of-plane and in-plane hysteresis loops. Sets A, B and C displayed H_k values of ~55, ~65 and ~90 kOe, respectively. The anisotropy constants (K_u) for these three types of FePt films were calculated using Equation 4.1 [12]. It was observed that the K_u values increased with an increase in the helium content in the sputtering gas mixture. The K_u values estimated for sets A, B and C were ~2.5, ~3.2, and ~4.9 $\times 10^7$ ergs/cc, respectively.

$$\mathbf{K_u} = \frac{\mathbf{M_s H_k}}{\mathbf{2}} \qquad \text{Equation 4.1}$$

The XRD profiles of all the three sets are shown in Figure 4.3. The presence of (001) and (002) peaks of FePt confirmed the attainment of the $L1_0$ phase for all the three sample sets. The (002) peaks of FePt were slightly asymmetrical towards smaller 2θ values because of the prevalence of the (200) FePt peaks. This is due to the weak fcc phase which was still present in the films. However, there were slight yet observable shifts of the (002) FePt peak towards higher 2θ value for sets B and C. Ideally, the (001) and (002) peaks of the $L1_0$ phase FePt layer are expected to appear at 23.9° and 48.9°, respectively. For Set A, the (001) and (002) peaks for the FePt film were estimated to be present at 23.7° and 47.8°, respectively. Hence, the peak shift observed for both sets B and C towards higher 2θ values implied an improvement in the fct phase of the FePt film when deposited in an Ar–He (0.5%) and Ar–He (1%) environment, respectively. The ratio of the superlattice (001) to the fundamental (002) peak intensities of the FePt layers obtained from the XRD results of the three samples was substituted in Equation 4.2 to estimate the ordering parameters (**S**) of the films [13].

$$\mathbf{S} \approx \mathbf{0.493}\left(\frac{\mathbf{I_{001}}}{\mathbf{I_{002}}}\right)^{\mathbf{1/2}} \qquad \text{Equation 4.2}$$

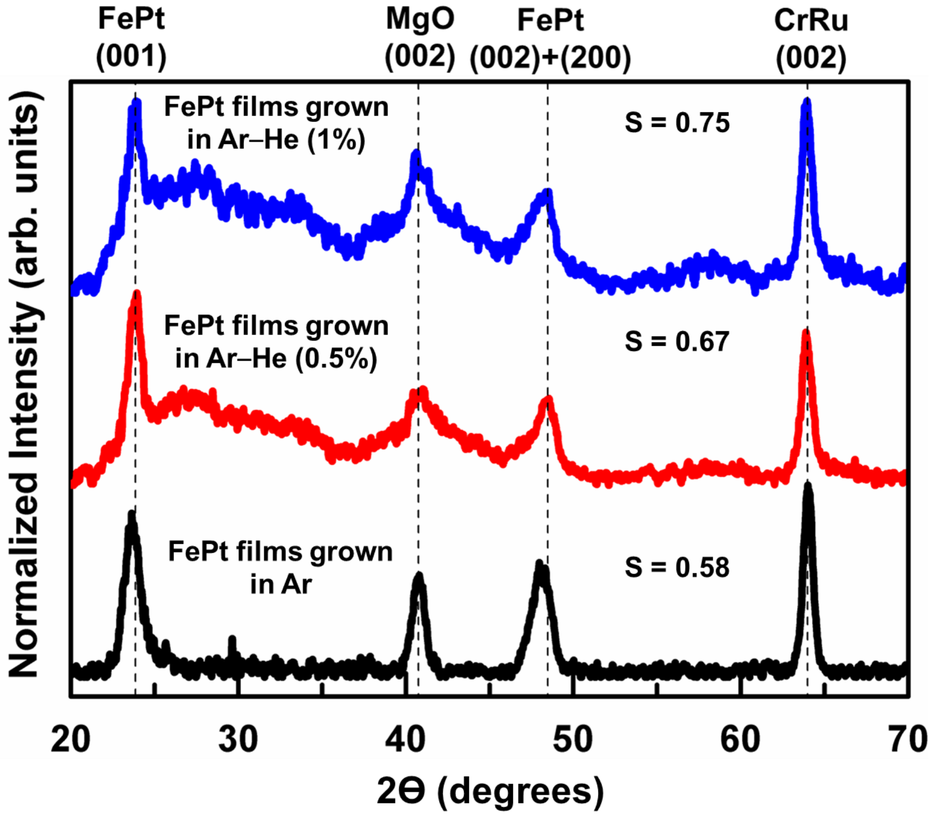

Figure 4.3 XRD profiles of $L1_0$ FePt films grown in Ar, Ar–He (0.5%) and Ar–He (1%) atmospheres.

A trend that is identical to the out-of-plane coercivity values [Figure 4.2] of the samples was seen in this structural characterization. There was a considerable rise in the ordering parameter of the FePt film deposited in Ar–He environments. Set B (***S*** = 0.67) and Set C (***S*** = 0.75) displayed higher ordering parameters with respect to the reference sample Set A (***S*** = 0.58). This observation supported the hypothesis that the incorporation of a small amount of helium in the chamber together with the carrier gas argon enhanced the magneto-crystalline anisotropy, which in turn increased the out-of-plane coercivity of the FePt film.

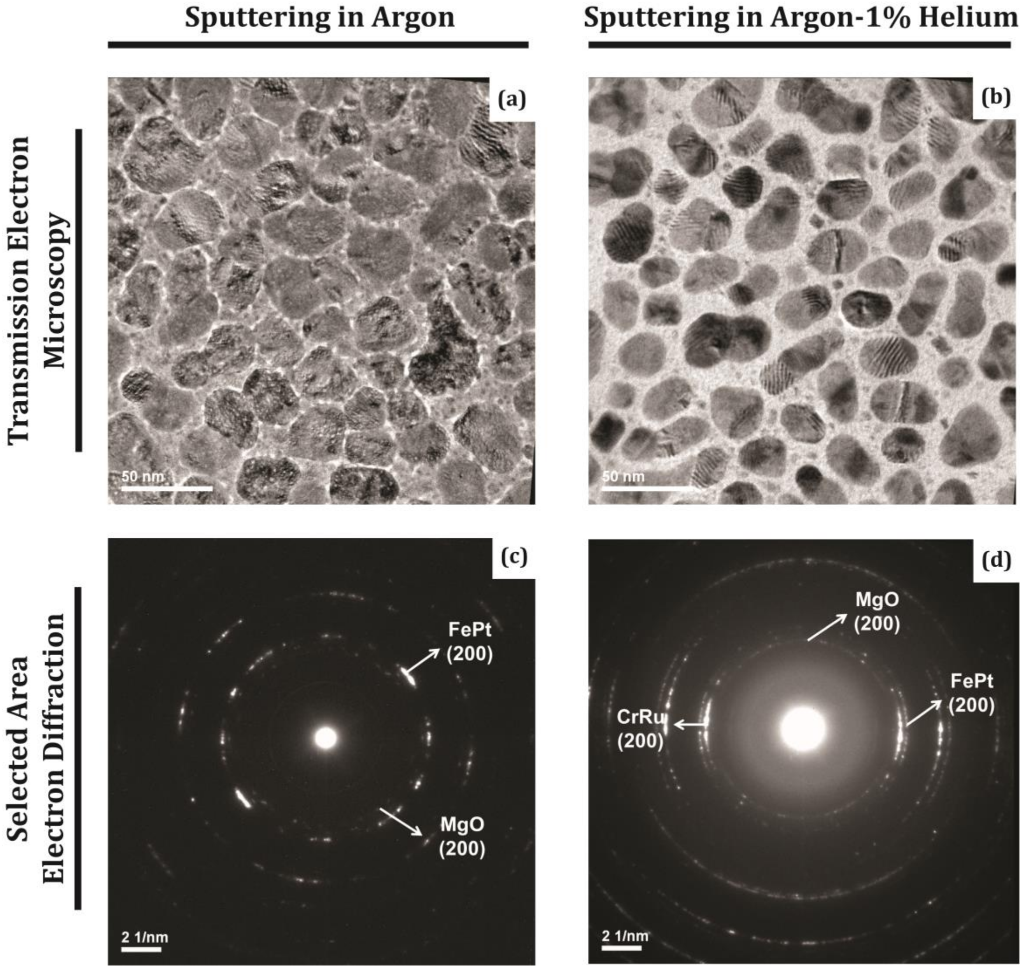

Figure 4.4 TEM and SAED images of $L1_0$ FePt films grown in Ar and Ar–He (1%) environments.

Next, it was necessary to find out if there were any noteworthy changes in the microstructure of the FePt films grown in the Ar–He atmosphere. TEM (top view) was carried out on Set A and Set C to identify and understand the basic changes brought about by the change in carrier gas composition on the $L1_0$ FePt grains. The TEM images of Sets A and C, as shown in Figure 4.4 (a) and (b) respectively, revealed that modifying the sputtering gas combination reduced the size of the FePt grains. The grain diameter and its distribution were calculated by analyzing the TEM images in the ImageJ software [14]. The ImageJ software can be programmed to distinguish the grain areas from the grain boundaries in a TEM image. The area covered by each grain was determined. For easier analysis, the grains were assumed to be circular and their respective grain diameters were estimated. The mean and standard deviation of the calculated grain diameters validated that the grain dimensions decreased from 40.6 nm ± 12 nm (for Set A) to 24.4 nm ± 10 nm for Set B. Selected area electron diffraction (SAED) was also carried out to detect any crystallographic difference over a small area (~200 × 200 nm^2) between the grains in Set A and Set C. Analogous to the XRD profile, the SAED patterns in Figure 4.4(c) and (d) also suggested the existence of a heteroepitaxial relationship between FePt and the underlying layers. However, unlike the SAED patterns obtained for Set A, the SAED patterns for Set C clearly displayed a diffraction ring corresponding to (200) orientation of CrRu. This reflected a strong crystallographic relation amongst the three layers, *viz.*, FePt (001)[100] || MgO (001)[100] || CrRu (001)[110].

Grain and grain boundary composition analyses on Sets A and C were simultaneously carried out using the TEM operating at 300 kV equipped with

EELS. Figure 4.5 shows the EELS data of elements present in the grain and grain boundary of sets A and C. From Figures 4.5 (a)-(d), it can be seen that the grains formed in both sets A and C were rich in Fe and Pt. However, lower transmitted signals (electron count) obtained from the grains in Set C compared to those in Set A were indicative of grains with smaller volume in the former. Elements from the underlying layers, i.e., Mg, O, and Cr, were also detected in both cases as shown in Figures 4.5(e)-(h). Elemental mapping of the grain boundaries in Set A exhibited a similarity to that of the grains, i.e., all the components mentioned previously were observed. In contrast, Set C showed no traces of Fe and Pt at the grain boundaries [Figures 4.5(b), (d)]. However, the K edges of Mg and O, and the L edge of Cr were seen distinctly in the grain boundaries [Figures 4.5 (f), (h)]. From the EELS data, it may be inferred that when FePt media was deposited in an Ar environment, the presence of a significant amount of Fe and Pt in the grain boundaries caused the grains to be exchange coupled. This would account for the lower coercivity of Set A. On the other hand, when Ar–He (1%) was selected as the sputtering gas, highly exchange decoupled and smaller sized FePt grains were obtained without the use of any non-magnetic ternary elements/species.

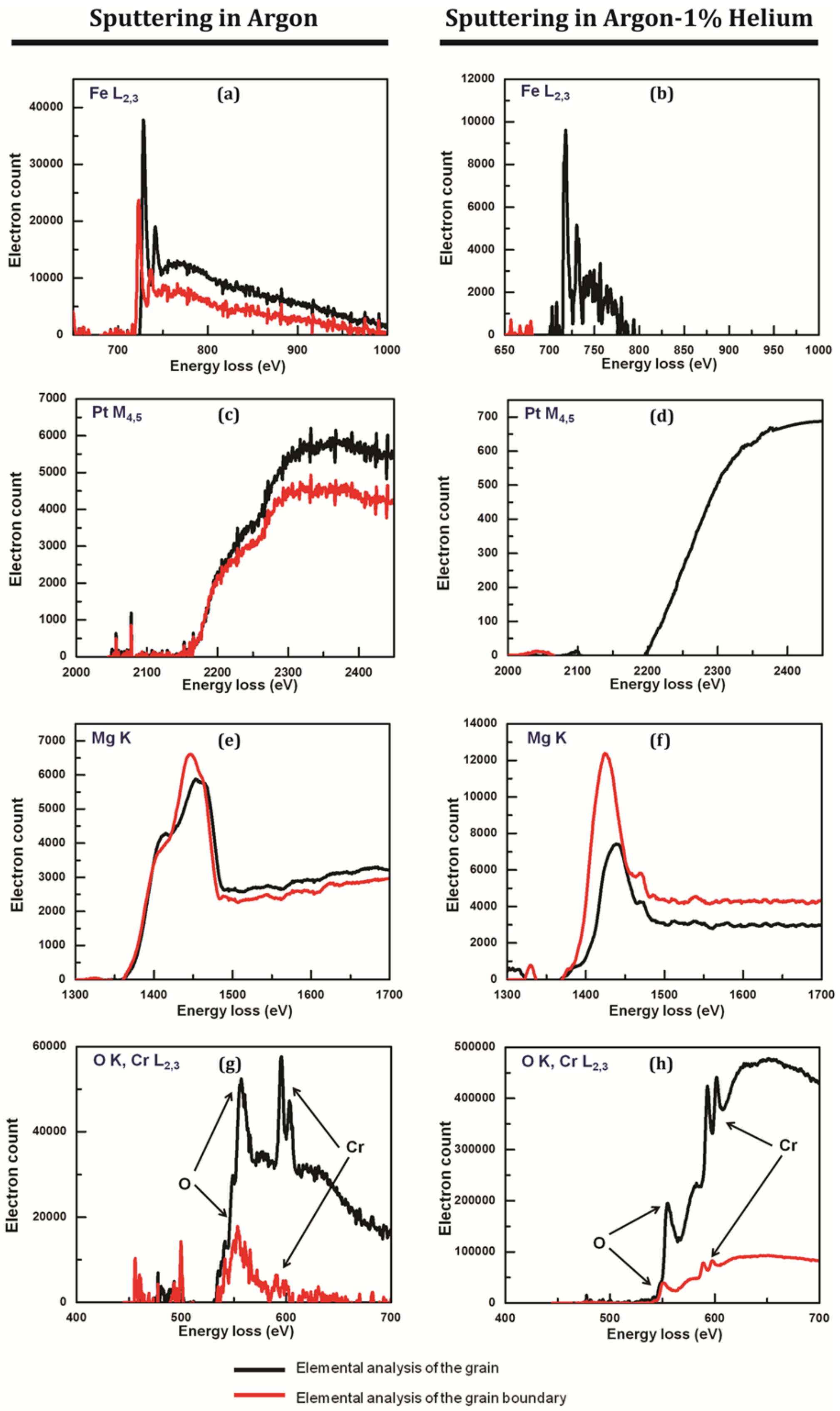

Figure 4.5 Grain and grain boundary composition analysis using EELS.

4.4 Discussion: Penning ionization

The refinement seen in the magnetic, structural and crystallographic properties of the FePt films, when deposited in the Ar–He environment, can be due to a change in the ion flux in the plasma caused by helium during deposition. Using helium, together with argon, initiated the Penning ionization [15] in the plasma. The plasma, ignited in the sputtering chamber when Ar–He was used as the carrier gas, comprised neutral atoms, atoms in their metastable states and positively charged ions of both the species (Ar and He), and electrons. The neutral excited metastable state of helium (He*) has the highest energy (19.82 eV) of all the rare gases [16] and is capable of ionizing the argon atoms, since its energy is higher than the first ionization potential of argon (15.6 eV). The ionization of Ar by He* may then be written as:

$$\mathbf{He}^{*} + \mathbf{Ar} \rightarrow \mathbf{Ar}^{+} + \mathbf{e}^{-} + \mathbf{He} \qquad \text{Equation 4.3}$$

Hence, there was an excess of Ar^+ ions in the plasma, apart from those produced conventionally by electron-impact ionization when helium was introduced into the chamber. This led to further enhancement of the number of Ar^+ ions bombarding the target surface per atom/entity. In other words, surplus energy was imparted to each target atom. Therefore, the increase in the ion current density in the plasma was responsible for providing the Fe and Pt atoms (as well as the Mg and O atoms) with the optimal adatom mobility required for their suitable arrangement in the lattice to achieve the chemically ordered fct phase. Addition of helium, as small as 0.5–1% by volume, to the sputtering gas was not expected to cause any change in the sputter yield. The plasma parameters of the targets – FePt (420 V, 240 mA), MgO (325 V, rf) and CrRu (360 V, 550 mA) – were the same, irrespective of the type of sputtering gas combination used, i.e., Ar or Ar–He (0.5–1%). The variation in ion density did not affect the magnetic properties of the FePt media stack in a radical manner when the CrRu layer was also deposited in Ar–He (Table 4.2, Set III). This suggested that unlike the Fe, Pt, Mg and O atoms, any change in the mobility of the Cr and Ru atoms on the substrate surface did not produce any major change in its texture. The heteroepitaxial relationship of $L1_0$ FePt and MgO with CrRu remained unperturbed. In other words, the crystallography of the FePt layer, and therefore its magnetocrystalline anisotropy, did not depend heavily on the sputtering gas combination used during the deposition of the CrRu layer.

There is another issue with argon when it is solely used as a sputtering gas. There is a high probability for the Ar^+ ions/neutrals to be backscattered with sufficient kinetic energy from the target, causing them to impinge on the substrate surface. These undesired Ar^+ ions/neutrals present on the growing film surface may collide frequently with the incoming Fe and Pt atoms, therefore reducing their kinetic energy. This could have further degraded their chemical ordering, leading to a shift in the (001) and (002) peak positions of FePt away from their ideal locations [Figure 4.3]. However, when the Ar–He mixture was used, there was a rise in the yield of the energetic Ar^+ ions by helium. These ions would then undergo increased collisions with the backscattered Ar^+ ions/neutrals in the plasma between the substrate and the target, thus deflecting them from their original path and preventing them from reaching the substrate surface. In addition, high momentum exchange between the argon and helium species would remove any entrapped Ar^+ ions/neutrals present in the film [17, 18]. This improvement in the chemical ordering of the

FePt film by the Ar–He sputtering gas combination was also reflected in its higher out-of-plane and lower in-plane coercivity values with increasing helium concentrations.

The small and gradual increase in the shearing of the hysteresis loops [Figure 4.2] pointed towards a possible increase in decoupling of the grains with an increasing volume of helium. The TEM images of the grains [Figure 4.4] and the EELS data [Figure 4.5] obtained for Set A and Set C confirmed that the FePt grains formed in the Ar–He (1%) environment were more exchange decoupled than those in the reference Set A. A planar growth of the grains is inferred from their large diameters in Set A. Microstructural evolution is dependent on the adatom binding energy to the substrate surface and contamination (including concentrations not detected by various analytical techniques) in the layers being deposited [19], amongst others. In an Ar environment, impingement of the Ar^+ ions/neutrals on the substrate surface and their subsequent collisions with the FePt adatoms hinder their rearrangement. This may result in them binding to the substrate more strongly than to each other, therefore displaying a two-dimensional growth. With the change in carrier gas composition from Ar to Ar–He (1%), a transition from planar grain growth to island growth was observed. As discussed earlier, the Ar–He environment may be responsible for improving the adatom mobility of the Fe and Pt atoms, lowering the Ar impingement onto the substrate surface and removing any residual Ar incorporated in the films. As a result, the FePt adatoms – deposited using Ar–He (1%) as the sputtering gas mixture – were bound to each other more strongly than to the substrate, which drove them towards island growth along the direction normal to the substrate surface.

4.5 Summary and Scope of Improvement

- The properties of the granular $L1_0$ FePt films were tailored by modifying the sputtering gas composition from Ar to Ar–He. Larger out-of-plane coercivities of the FePt magnetic media were achieved with increasing helium volume. Improved adatom mobility and lower argon-adatom interaction on the growing film surface with increasing helium percentage are suggested as the possible causes for the improvement in the ordering parameter of the FePt layer, which further ensured higher magnetocrystalline anisotropy values for sets B and C. The rise in anisotropy increased the out-of-plane coercivities of these two sets. In contrast to the grain dimensions obtained during deposition in the Ar atmosphere, smaller grains of diameter ~24 nm were achieved when the samples were grown in the Ar–He (1%) environment.

- This investigation presents a new technique, which generates higher out-of-plane coercivity, well-isolated grains and reduced grain sizes simultaneously, for developing the desired HAMR media for ultra-high areal densities >1 Tb/in^2. It may be proposed that further fine-tuning of the sputtering gas mixture such as a higher amount of helium in a given volume could lead to smaller grains (<24 nm). Introducing more helium into the sputtering chamber implies further increase in the creation of Ar$^+$ ions through penning ionization. In addition, He$^+$ ions will also be present in the plasma. As a result, there will be an increase in the number of collisions of the target atoms with He$^+$ ions. The plasma density and the number of gas-phase collisions in the chamber will be altered, which in turn will impact the energy imparted to the Fe and Pt adatoms. This will eventually influence the FePt grain growth and can lead to smaller grain sizes of ~3-4 nm. The TEM image of the grains in Figure 4.4(b) depicts the occurrence of two events – (a) merging of two FePt grains and (b) secondary nucleation in the wide grain boundaries. A gradual evolution in the microstructure of $L1_0$ FePt, attainment of smaller grain sizes and changes in grain density with further increases in the helium amount (>1%) could have been carried out. However, the investigation was limited by the fact that lighter gaseous atoms like helium cannot be removed effectively from ultra-high vacuum sputtering chamber using cryo-pumps such as ours. As a result, helium remains as predominant species inside the chamber. Therefore, using higher helium volume in the sputtering gas combination to explore its influence on the properties of $L1_0$ FePt is not easy in our sputtering system.

References

[1] K. R. Coffey, M. A. Parker, and K. J. Howard, High anisotropy $L1_0$, thin films for longitudinal recording, IEEE. Trans. Mag. 31, 2737 (1995).

[2] D. Ravelosona, C. Chappert, V. Mathet, and H. Bermas, Chemical order induced by ion irradiation in FePt (001) films, Appl. Phys.Lett. **76**, 236 (2000).

[3] Y. Ding, J. Chen, and E. Liu, Structural and magnetic properties of FePt films grown on $Cr_{1-x}Mo_x$ underlayers, Appl. Phys. A Mater. Sci. Process **81**, 1485 (2005).

[4] W. Shen, J. Judy, and J. Wang, In situ epitaxial growth of ordered FePt (001) films with ultra small and uniform grain size using a RuAl underlayer, J. Appl. Phys. **97**, 10H301 (2005).

[5] Y. Peng, J.-G. Zhu, and D. Laughlin, $L1_0$ FePt–MgO perpendicular thin film deposited by alternating sputtering at elevated temperature, J. Appl. Phys. **99**, 907 (2006).

[6] A. Sun, P. Kuo, J. Hsu, K. Huang, and J. Sun, Epitaxial growth mechanism of $L1_0$ FePt thin films on Pt/Cr bilayer with amorphous glass substrate, J. Appl. Phys. **98**, 076109 (2005).

[7] Y. Lee, B. Lee, C. Lee, B. Koo, and Y. Shimada, Effect of boron addition on disorder–order transformation of FePt thin films, J. Magn. Magn. Mater. **310**, e918 (2007).

[8] B. Li, C. Feng, Z. Gao, J. Teng, G. Yu, Z. Xing, and Z. Liu, Magnetic properties and microstructure of FePt/BN nanocomposite films with perpendicular magnetic anisotropy, Appl. Phys. Lett. **91**, 152502 (2007).

[9] L. Zhang, Y. K. Takahashi, A. Perumal, and K. Hono, $L1_0$-ordered high coercivity (FePt)Ag-C granular thin films for perpendicular recording, J. Magn. Magn. Mater. **322**, 2658 (2010).

[10] K. K. M Pandey, N. Gaur, and C. S. Bhatia, Interface mediated control of microstructure and magnetic properties of FePt-C thin films, J. Magn. Magn. Mater. **323**, 2658 (2011).

[11] N. Gaur, Investigations on ion implantation in advanced magnetic recording media [thesis, online] (2013). Available at: http://scholarbank.nus.edu.sg/bitstream/handle/10635/36572/Part1%20GaurN.pdf?sequence=1

[12] Y. Saito, H. Sugiyama, T. Inokuchi, and K. Inomata, Interlayer exchange coupling dependence of thermal stability parameters in synthetic antiferromagnetic free layers, J. Appl. Phys. **99**, 08K702 (2006).

[13] S. D.Granz and M. H. Kryder, Granular $L1_0$ FePt (001) thin films for heat assisted magnetic recording, J. Magn. Magn. Mater. **324**, 287 (2012).

[14] Examples of Image Analysis Using ImageJ [online] (June 2007). Available at: http://rsb.info.nih.gov/ij/docs/pdfs/examples.pdf

[15] A. A. Kruiphof and F. M. Penning, Determination of the townsend ionization coefficient α for mixtures of neon and argon, Physica **4**, 430 (1937).

[16] A. K. Chawla, S. Singhal, H. O. Gupta, and R. Chandra, Effect of sputtering gas on structural and optical properties of nanocrystalline tungsten oxide films, Thin Solid films **517**, 1042 (2008).

[17] Y.-H. Kim, W.-K. Kim, and J.-I. Han, Poly-Si TFTs fabricated on flexible substrates by using sputter deposited a-Si films, J. Korean Phys. Soc. **48**, S14 (2006).

[18] T. Voutsas, H. Nishiki, M. Atkinson, J. Hartzell, and Y. Nakata, Sputtering technology of Si films for low-temperature poly-Si TFTs, SHARP Technical Journal, No. 3 (2001).

[19] I. Petrova, P. B. Barna, L. Hultman, and J. E. Greene, Microstructural evolution during film growth, J. Vac. Sci. Technol. A **21**, S117 (2003).

CHAPTER 5

Low energy C^+ ion embedment induced structural disorder in $L1_0$ FePt media

5.1 Motivation

In addition to attaining smaller grain sizes in $L1_0$ FePt magnetic media, the realization of reduced magnetic spacing (head-to-media spacing) is also pivotal for achieving areal densities beyond 1 Tb/in^2 [1]. Current hard disk drives (HDDs) comprise a diamond-like carbon (DLC) coating (~2-3 nm thick) and a perfluoropolyether-based lubricant (<2 nm thick) over the media surface to protect it from oxidation and wear which, predictably, adds to the magnetic spacing [2]. This, in turn, adversely affects the areal density growth. Minimizing the DLC thickness disturbs the continuity of the sputtered overcoat and, in turn, deteriorates the tribological and corrosion performance [3]. In addition, stability of the lubricant is likely to decline when the recording media is subjected to HAMR conditions [4]. Therefore, the onset of the magnetic trilemma, discussed in Chapter 2, necessitates the simultaneous development of new media materials and surface modification techniques for growing thinner (<2 nm), wear- and thermal-resistant carbon coatings.

In recent years, filtered cathodic vacuum arc (FCVA) – a method capable of depositing thinner (≤ 2 nm) and continuous tetrahedral amorphous (ta-C) carbon coatings – has facilitated the realization of reduced magnetic spacing [5, 6]. Using the FCVA system, the top few nanometers (≤ 2 nm) of the recording layer is embedded with C^+ ions at low ion energies, ranging from 100-350 eV, to create a mixed layer of C^+ ions and atoms of the magnetic film. Typically, a graded media surface is formed which comprises an atomically mixed layer protected by a few monolayers of carbon. This recording media, which is *nearly* overcoat-free, exhibits wear and oxidation resistance on par with the traditional thicker carbon overcoats.

Magnetic and structural studies of $L1_0$ FePt films have mostly been confined to film thicknesses of <10 nm. Degradation in the *c*-axis texture of the film and increase in grain sizes are the reasons for restricting the recording layer thickness to <10 nm [7]. Studies pertaining to 20 nm thick FePt media surfaces modified by the FCVA technique have confirmed the attainment of improved thermal properties and reduced coefficient of friction, thereby providing a viable alternative to the heat-resistant lubricants being developed for the HAMR scheme [8]. Although improved tribological properties have been achieved, the effect of low energy C^+ ion bombardment on the magnetic properties of $L1_0$ FePt films is still not known. In this chapter, a systematic study has been carried out to determine the impact of low energy C^+ ion embedment on sub-10 nm $L1_0$ FePt magnetic media.

To summarize, a bi-level C^+ ion embedment process carried out at 350 eV and subsequently at 90 eV on FePt media surfaces provided the desired optimal wear durability conditions. Figure 5.1 compares the wear test of a bare and embedded 15 nm thick FePt. The coefficient of friction was reduced by a considerable amount upon embedment, reflecting the effectiveness of the FCVA technique in producing wear-resistant <2 nm thick carbon overcoats. Surprisingly, a noteworthy transformation in the crystallography of the FePt films, with thicknesses ranging from 5 to 15 nm, was observed following this surface treatment. This, in turn, brought about a substantial decrease in the out-of-plane coercivity values of the media. Elemental analysis attributed this outcome to the diffusion of C^+ ions through the entire length of the FePt grains. Interestingly, even though low energy embedding was performed on the samples, the basic aspects of ion beam mixing – the size of the incident C^+ ions with respect to the media's lattice constant, the existence of channeling in $L1_0$ FePt, and the presence of multiple collision driven momentum transfer – all played a crucial role in impacting the chemical ordering of the entire $L1_0$ FePt layer. These factors affect the feasibility of employing this otherwise tribologically useful carbon embedding FCVA technique in FePt thin films. In addition, the significance of this investigation lies in providing the groundwork necessary for exploring a novel method to fabricate FePt bit patterned media using this shallow embedment technique instead of high energy ion implantation (the details of which have briefly been presented in Section 5.5 and discussed in depth in Chapter 6).

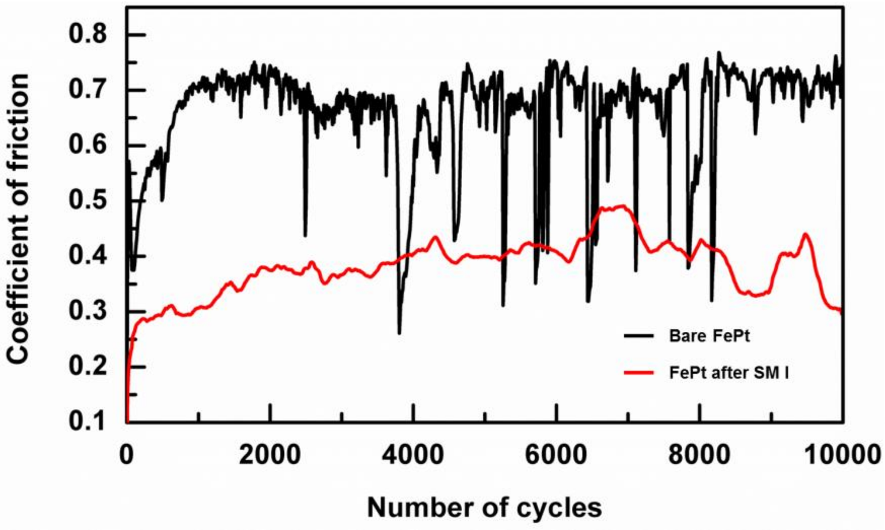

Figure 5.1 Tribological results obtained from a bi-level C^+ ion embedment process carried out at 350 eV and, subsequently, 90 eV on FePt. Prior to embedment, the surface was etched using Ar^+ ions. Comparison of the wear test carried out on FePt surfaces before and after C^+ ion embedment (SM1). Sapphire ball of 4 mm in diameter with an applied load of 20 mN load was used. The speed of rotation of the ball was 2.1 cm/s.

5.2 Experimental Details

Figure 5.2 shows the FePt media structure deposited in the sputtering system maintained at a base pressure of 5×10^{-9} Torr. Argon was used as the sputtering gas. FePt films of thicknesses 5, 10 and 15 nm were grown on deposited CrRu (20 nm) / MgO (3 nm) layers. The first underlayer, i.e. CrRu, was grown on a 0.5 mm thick glass substrate at 400 °C and 1.5 mTorr pressure. The deposition condition of MgO matched that of CrRu. FePt layers were grown at 600 °C and 3 mTorr pressure to achieve the $L1_0$ ordering.

A bi-level surface modification process was carried out in these films by employing the FCVA technique at Nanofilm Technologies International Private Limited (Singapore). The base pressure of the system was kept at 7.5×10^{-7} Torr. The films were subjected to C^+ ion bombardment at 350 eV to form an atomically mixed layer of C, Fe and Pt to improve the adhesion of the carbon layer to the media surface. This was followed by a relatively low energy embedment at 90 eV to generate higher sp^3 content in the carbon monolayer atop the mixed layer [2, 9]. To achieve the required ion energies, the substrate was negatively biased. Negative pulsed voltages of 340 and 80 V, at a frequency of 20 kHz and duty cycle of 60%, were applied. These energy values, deduced using the Transport of Ions in Matter (TRIM) program provided in the Stopping and Range of Ions in Matter (SRIM) software, suggested a shallow implantation depth of $\leq$ 2nm in the FePt films as shown in Figure 5.3. It should be noted that the TRIM simulations were designed by taking into consideration the 60% duty cycle used during the FCVA embedment. The arc current used during both the embedment processes for igniting the graphite target was 40 A. However, the system was not instrumented with techniques such as Faraday cup and Pearson coil to measure the C^+ ion dose used in the experiment.

Three sets of surface modification treatments on the $L1_0$ FePt samples are studied here. Surface modification I (SM I) comprised FePt films which were etched in Ar^+ ion plasma at 500 eV to remove any residual oxide layer present atop them. This was followed by the two-step C^+ ion embedding process. The next two sets of surface modifications were intended to probe the cause of change in the magnetic properties of the FePt films – the sputter etching species (Ar^+ ion) or the embedding species (C^+ ion). Therefore, the recording layer was subjected *separately* to Ar^+ ion etching (SM II) and bi-level C^+ ion embedment (SM III). The etching and embedding conditions were kept the same for all the three treatments. Table 5.1 summarizes the abovementioned surface treatments.

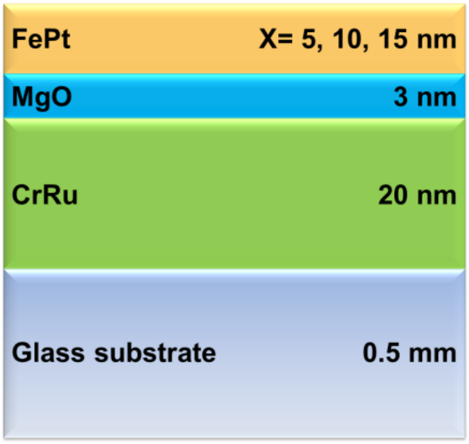

Figure 5.2 Schematic of the FePt media stack(s) employed for studying low energy induced C^+ ion embedding.

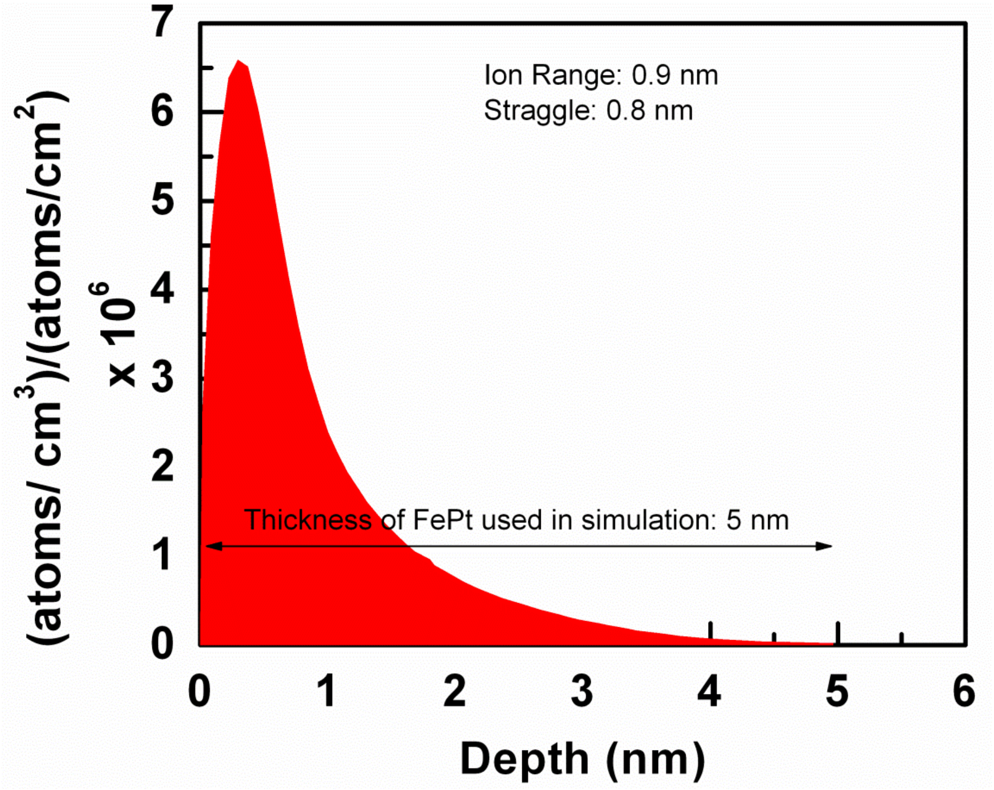

Figure 5.3 TRIM simulated embedment profile of the C^+ ions in the top few nanometers of the FePt film. Embedment was carried out at 350 eV followed by 90 eV. The 60% duty cycle used in the experiment was also taken into consideration while carrying out the simulations. The incident angle between the substrate surface and the incoming ion was 90°.

Sample type	**Ar^+ ion etching at 500 eV**	**C^+ ion embedment at 350 followed by 90 eV**
Reference *$L1_0$* FePt	No	No
SM I	Yes	Yes
SM II	Yes	No
SM III	No	Yes

Table 5.1 Summary of the different surface treatment conditions to which the FePt films had been subjected.

5.3 Results: Characterizing low energy C^+ ion embedded FePt films

Figure 5.4 compares the out-of-plane hysteresis loops of the $L1_0$ FePt magnetic media before and after the three surface modifications. Prior to embedment, FePt films with thicknesses 5, 10 and 15 nm exhibited coercivities of ~15, ~14 and ~13 kOe, respectively [Figures 5.4 (a), (c) and (e)]. A kink was observed at zero field in the hysteresis loop measured for the 15 nm thick FePt media. This may be attributed to the growing soft magnetic phase in the film, thus indicative of the deteriorating crystallography with increasing recording layer thickness.

Upon undergoing SM I, the FePt films with thicknesses 5 and 10 nm [Figures 5.4(b) and (d)] displayed a severe decrease in coercivity values to ~1 kOe. Furthermore, the squareness of the loops dropped to ~20%, thereby suggesting substantial degradation of the *c*-axis texture within the films. The damage to the magnetic properties of the $L1_0$ FePt films may be due to a possible lattice rearrangement brought about by the embedded C^+ ions or an excessive sputter etching of the magnetic layer when exposed to Ar^+ ions initially, or a combination of both of these processes. Momentum transfer between the incoming Ar^+ ions and the host atoms could possibly disorder the fct phase instead of purely knocking the Fe and Pt atoms off the film. Therefore, it was necessary to examine the FePt films treated with SM II and SM III. Both SM II and SM III resulted in diminished coercivities for 5 and 10 nm thick FePt films [Figures 5.4 (b) and (d)]. The coercivity values for samples which underwent SM III were slightly higher compared to those which were treated with SM I and SM II. Nevertheless, these results confirmed the manifestation of the two aforementioned events in the FePt media – Ar^+ ion induced damage (SM II) and C^+ ion embedment initiated disorder (SM III) in the recording layer. By tuning the etching conditions, this deleterious effect of Ar^+ ions on the FePt layer can be significantly reduced. In contrast, tailoring the energy values of the C^+ ions is not preferred as the tribological properties of the film may be compromised.

The surface modified 15 nm thick FePt films were also investigated as shown in Figure 5.4(f). Similar to the FePt films with thickness ≤10 nm [Figures 5.4(b) and (d)], the 15 nm thick FePt films [Figure 5.4(f)] also showed reduced out-of-plane coercivities. The decrease in coercivity was estimated to be ~60, ~47 and ~45% in the FePt layer after treatment with SM I, SM II and SM III, respectively. Therefore, the adverse effect on the magnetic properties of the $L1_0$ FePt films arising from the C^+ ion bombardment was slightly suppressed by increasing the layer thickness above 10 nm. Table 5.2 summarizes the out-of-plane coercivities of the reference and surface modified films of all thicknesses.

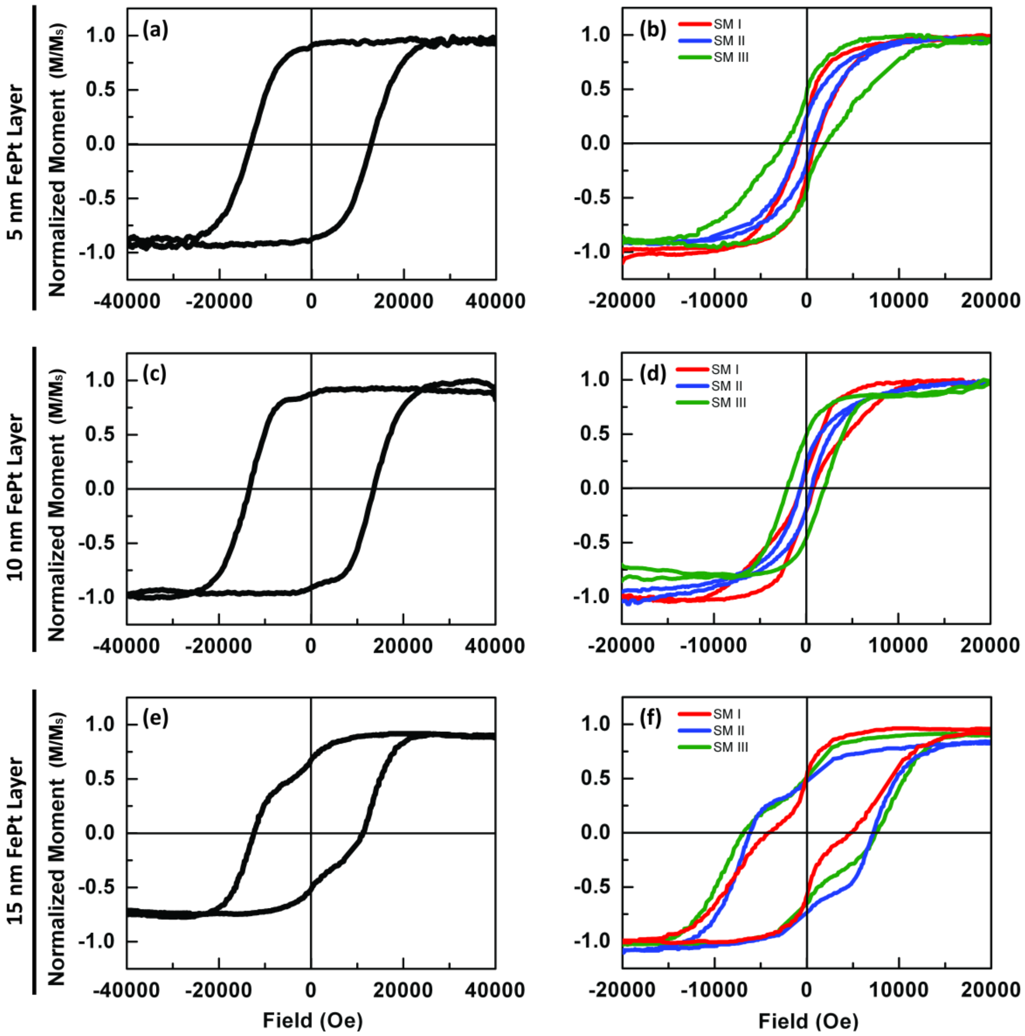

Figures 5.4 (a), (c) and (e) show the out-of-plane hysteresis loops of the reference $L1_0$ FePt films of thicknesses 5, 10 and 15 nm, respectively. (b), (d) and (f) show the out-of-plane hysteresis loops of the 5, 10 and 15 nm thick FePt films, respectively, after SM I, SM II and SM III treatments (Table 5.1).

Sample Type	**Out-of-plane coercivities at varying thicknesses (kOe)**		
	5 nm	**10 nm**	**15 nm**
Reference *L1₀* FePt	15	14	13
SM I	0.7	0.8	5
SM II	0.8	0.8	6.8
SM III	2	2	7.1

Table 5.2 Summary of the coercivities of the FePt films of thickness 5, 10 and 15 nm before and after SM I, SM II and SM III.

Figure 5.5 shows the XRD results of the reference and surface modified FePt films. In order to streamline this discussion to the effect of C^+ ions embedding in the FePt layer, results obtained from samples treated with SM III only have been presented and analyzed with respect to the reference $L1_0$ FePt samples. From Figure 5.5, the (001) and (002) FePt peaks which are characteristic for the $L1_0$ phase were observed along with the (002) MgO and (002) CrRu peaks for all the three reference films. Ordering parameters (S) were estimated for these samples from the ratio of the superlattice (001) to the fundamental (002) peak intensities of the FePt layers acquired from the XRD profiles and then substituted in Equation 5.1 [9].

$$\mathbf{S \approx 0.493\left(\frac{I_{001}}{I_{002}}\right)^{1/2}} \qquad \text{Equation 5.1}$$

The 5 and 10 nm thick FePt films prior to any embedding were well-ordered and exhibited S=0.7 and 0.6, respectively [Figures 5.5(a) and (b)]. On the other hand, the reference samples with a thickness of 15 nm displayed S=0.45, lower than that of the ≤10 nm thick FePt films [Figure 5.5(c)]. This is expected since the epitaxial relation between (001) FePt and (002) MgO and CrRu deteriorates with increasing thickness, thereby affecting the *c*-axis texture.

When SM III was carried out, no clear (001) FePt peak was visible for any of the films, whether they were ≤ or >10 nm in thickness. Broad bulges were observed as opposed to the (001) peaks which are likely to correspond to amorphous carbon. The occurrence of these bulges in the XRD plot might be due to the presence of embedded C^+ ions in the FePt films [10]. Therefore, calculating S from the (001) and (002) FePt peak intensities was not acceptable. Nonetheless, a small yet consequential shift in the (002) FePt peak towards lower theta values was noted for each of these surface treated films of different thicknesses [Figures 5.5(a), (b) and (c)], signifying the emergence of the low anisotropy disordered phase.

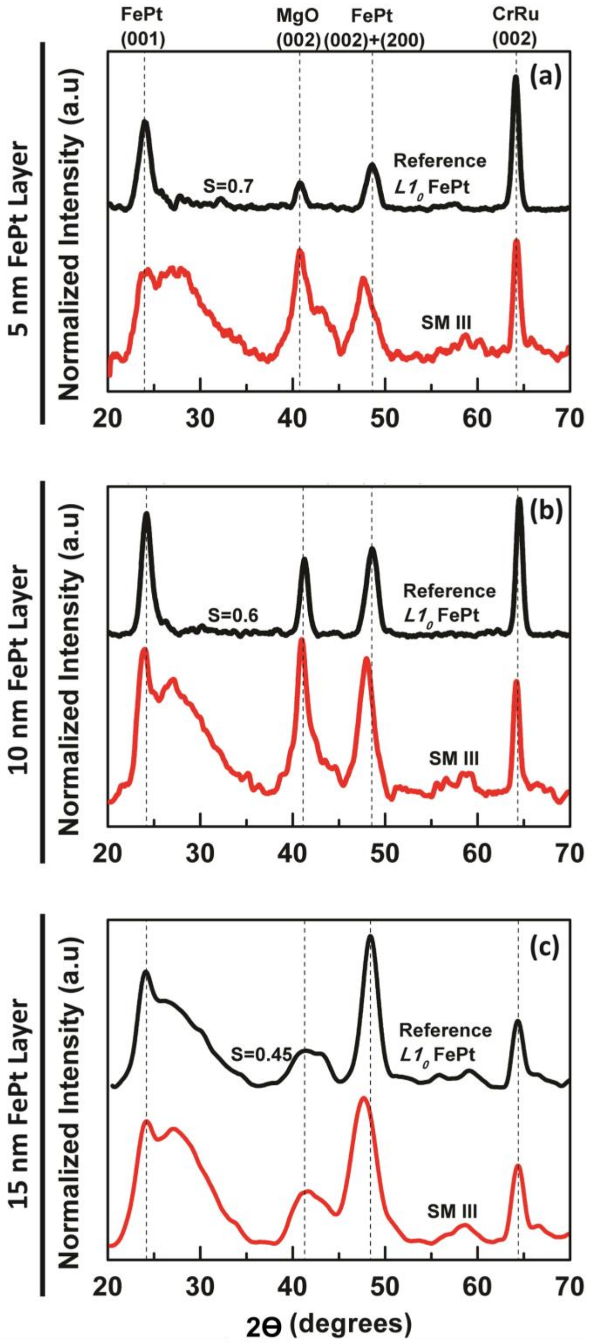

Figures 5.5(a), (b) and (c) display the XRD plots of 5, 10 and 15 nm thick reference and SM III treated FePt films, respectively.

Figures 5.6(a) and (b) display the TEM images of the reference and SM III treated 10 nm thick FePt layer. It can clearly be observed from the two images that a 2 nm thick carbon layer existed upon SM III treatment. The overlapping of the carbon layer with the FePt film, depicted in Figure 5.6(b), confirmed the formation of a thin mixed layer, which is essential for obtaining good tribological properties (refer to Figure 5.1). However, an elemental scan using scanning TEM (STEM) operating at 200 kV in high angle annular dark field (HAADF)-STEM mode and equipped with energy dispersive X-ray spectroscopy (EDX) indicated possible diffusion of C^+ ions through single FePt grains [Figure 5.7] which have been imaged and shown in Figure 5.6(b). The comparison between reference and SM III samples revealed the likelihood of having C^+ ion distribution throughout the length of the grains after exposure to SM III. Carbon was detected in the reference $L1_0$ FePt grain. This was anticipated due to the residual organic contamination on the film from ion milling during sample preparation as well as from the environment. Hence, for a fair comparison between the reference and SM III treated samples shown in Figures 5.7(a) and (b) respectively, Fe, Pt and C intensities were normalized. As shown in Figure 5.7(a), the C^+ ion profile appeared constant across the reference FePt grain length. On the other hand, a gradient was observed in the C^+ ion distribution in the SM III treated FePt grain [Figure 5.7(b)], which suggested possible diffusion of the C^+ ions from the surface to the bottom of the FePt grain.

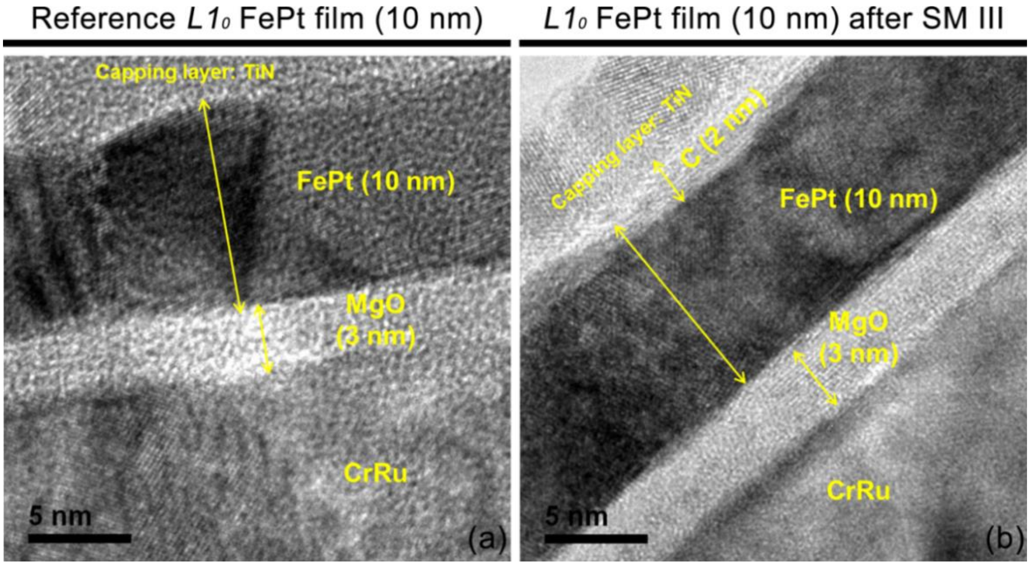

Figure 5.6 TEM images of the 10 nm thick FePt film (a) before and (b) after SM III.

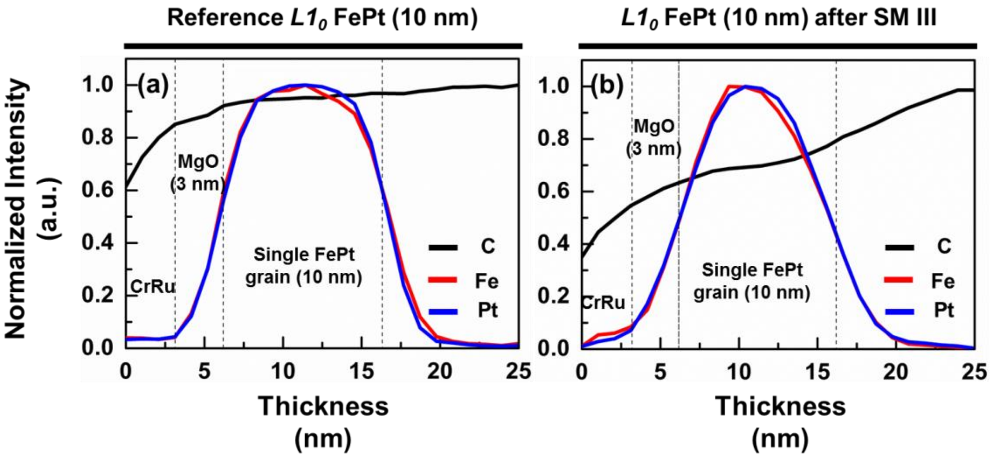

Figure 5.7 EDX analysis of a FePt grain (a) before and (b) after SM III.

The C$^+$ ion embedment in FePt films was designed to be restricted to the film surface. Interestingly, FCVA-based surface treatment showed an adverse effect on the crystal structure of the FePt layer, thereby leading to poor magnetic properties. The TRIM simulations of ion implantation of C$^+$ ions in the FePt layer assume the latter to be amorphous. Therefore, embedding at a low energy of 350 eV should cause the C$^+$ ions to scatter and give rise to a Gaussian profile close to the FePt film surface defined by a mean range of 0.9

nm and a straggling of 0.8 nm about this mean value [Figure 5.3]. However, during implantation in crystalline materials, the range distribution of the embedded ions within the lattice may vary depending on the material's crystallographic orientation with respect to the direction of ion velocity [11]. In this case, the direction of motion of the incoming C^+ ions coincides with the *c*-axis of the $L1_0$ FePt lattice. Hence, it is likely that the ions might traverse through the crystal structure slightly more than that estimated by TRIM. Moreover, this phenomenon, known as channeling [11], is seen to be prominent when the lighter incident ions are embedded into a crystalline solid consisting of heavier atoms because the atomic radius of the ion is less than the lattice spacing [12]. Therefore, the smaller size of the C atoms in contrast to the lattice spacing along the *a*-axis (3.83 Å) of the FePt [13] further supports the proposition on order-disorder transition induced in a significant portion of the $L1_0$ FePt layer due to surface modification. Hence, in order to examine the embedment depth of the C^+ ions in the FePt layer, ToF-SIMS was carried out on an area of $4 \times 4\ \mu m^2$ of the samples.

Figure 5.8(a) depicts the depth profile of the reference $L1_0$ FePt media in which the recording layer thickness was 10 nm. Peaks corresponding to elements Fe and Pt from the recording layer were observed. These were then followed by the MgO peak. Background C from the system was also detected. The emerging MgO peak is used in Figure 5.8(a) as an index to identify the end of the recording layer and the beginning of the layers underneath. It was inferred from the plot that the 10 nm thick FePt layer was extended till the etching time of ~300 seconds. The intensity count obtained from the materials was plotted against time instead of depth. The actual depth for each ToF-SIMS analysis is dependent on the etch-rate of the ion-gun, which in turn, will be determined by the material being removed at any given depth. Therefore, two different materials with different etch rates could not be plotted on the same depth axis.

Figure 5.8(b) shows the depth profile carried out on a 10 nm thick FePt sample subjected to SM III. The embedded C^+ ion profile in the FePt layer, attained after subtracting the background C, displayed a Gaussian shape similar to the one simulated using TRIM [Figure 5.3]. The mean range calculated from the plot was ~1.2 nm, which appeared to be in relatively good agreement with the mean range value (0.9 nm) obtained from the TRIM simulations [Figure 5.3]. However, unlike the profile in Figure 5.3, the embedded C^+ ion profile had a tail penetrating deeper than 2 nm into the FePt layer. Furthermore, additional peaks superimposed on the Fe and Pt peaks, representing the magnetic layer [Figure 5.8(a)], were clearly visible in Figure 5.8(b). These peaks most likely represented the Fe and Pt atoms in the magnetic layer which had undergone recoil implantation upon bombardment with C^+ ions. In other words, these were the atoms which had been knocked out from their original lattice positions to locations that were a few lattice sites away. It would be reasonable then to assume that these recoiled atoms contributed significantly to the disordering of the fct phase, which led to lower anisotropy and, eventually, reduced values of coercivity.

The TRIM simulations were carried out to verify the outcome from the ToF-SIMS analysis. Figure 5.8(c) shows the simulated recoil distribution of the Fe and Pt atoms after the embedment of the C^+ ions. The profile of the implanted C^+ ions, scaled to the size of the largest recoil atom, is also shown in the plot.

The inset of Figure 5.8(c) depicts the recoil distribution of the Fe and Pt atoms obtained experimentally by subtracting the reference Fe and Pt profiles [Figure 5.8(a)] from their respective profiles achieved after SM III [Figure 5.8(b)]. The experimental and simulated recoil profiles of the host atoms appeared similar. However, it should be noted that the simulated recoil distribution had a mean range value of ~0.6 nm for both the host atoms. On the other hand, the mean range peaks from the experimentally obtained recoil distributions of Fe and Pt atoms were ~1.6 and ~1.9 nm, respectively. These values were estimated by taking into consideration that the 10 nm thick FePt films were etched away in ~300 seconds while generating the depth profile using ToF-SIMS [Figure 5.8(a)]. Furthermore, the Gaussian recoil distribution of these recoiled atoms exhibited tails ranging to ~8 nm, as opposed to ~4 nm observed for the simulated recoil profiles, in a 10 nm thick FePt film. Therefore, a shift in the range of the recoiled host atoms deeper inside the recording layer, detected experimentally, implied that the disordering of the host atoms was not restricted to the top 2 nm of the FePt layer. More importantly, these results suggested channeling of the smaller sized C^+ ions into the crystalline FePt layer. It should be noted from Figure 5.8(b) that the maximum range representing an ideal channeling profile [14] was not achieved. In other words, only a certain number of the C^+ ions, incident on $L1_0$ FePt at a particular time, penetrated a distance greater than the simulated value before coming to rest by diffusion.

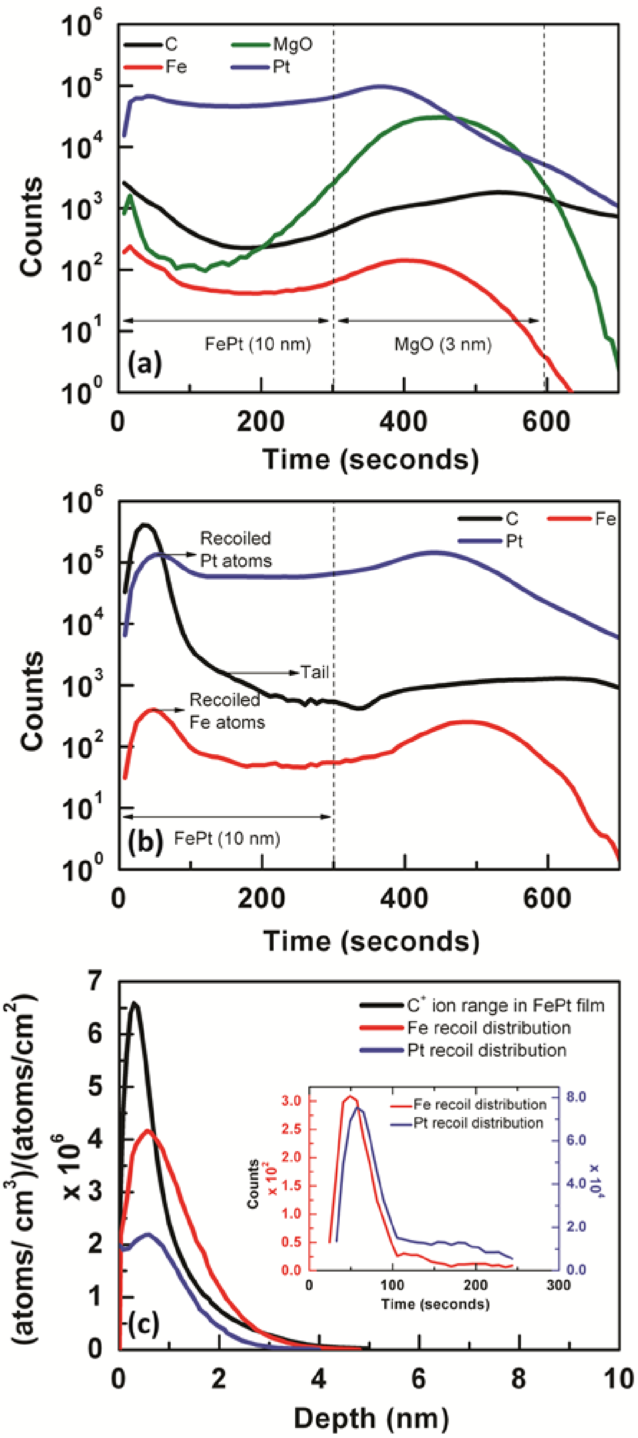

Figure 5.8 ToF-SIMS characterization of (a) reference *$L1_0$* FePt and (b) SM III treated FePt. The FePt film thickness was 10 nm. (c) shows the TRIM simulated Fe and Pt recoil distribution in the 10 nm thick FePt layer. The C^+ ion distribution is also shown. The inset in (c) shows the experimentally generated recoil distribution of Fe and Pt atoms in the FePt film after SM III.

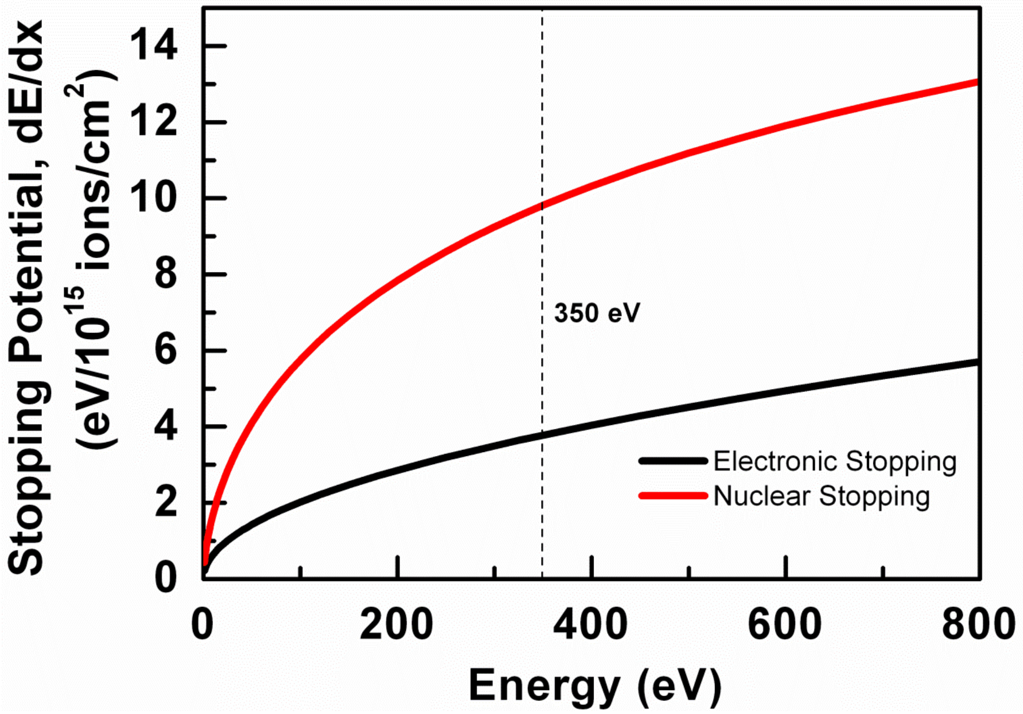

Figure 5.9 Electronic and nuclear stopping potential of the C^+ ions in the FePt layer.

5.4 Discussion: Kinchin-Pease model for navigating C^+ ions through FePt

It is essential to get a clear understanding of the degradation of magnetic properties of the FePt media samples after surface modification using C^+ ions. Figure 5.9 displays the TRIM simulated nuclear and electronic stopping potentials of the C^+ ions in FePt. It is evident from the plot that nuclear collisions dominate when embedment is carried out at 350 eV. Energy from the incident atoms is transferred as translatory motion to the host atoms as a whole and this leads to lattice disorder. The maximum energy transferred to the host atom ($\mathbf{E_t}$) is expressed as [14]:

$$\mathbf{E_t} = \mathbf{E_i}\frac{\mathbf{4M_1M_2}}{(\mathbf{M_1}+\mathbf{M_2})^2} \qquad \text{Equation 5.2}$$

where $\mathbf{E_i}$ and $\mathbf{M_1}$ are the energy and mass of the incident ion, and $\mathbf{M_2}$ is the mass of the host atom.

In our experiment, when the incoming C^+ ions bombarded the FePt film, the host atoms underwent collisions and were relocated several lattice sites away. Mere collisions between the host and incident atoms may not be responsible for the deterioration of the chemical order in the FePt films. Besides recoil mixing, a concurrent phenomenon taking place in the magnetic layer during embedding is cascade mixing − a series of repeated unrelated low energy atomic displacements and relocation events [15]. The host atoms, knocked out by the incident C^+ ions, are capable of displacing other host atoms from their lattice positions provided that their energy is greater than the threshold displacement energy $\mathbf{E_d}$ of the host atoms, which are still present in their respective lattice sites. According to the modified Kinchin-Pease model [16-18], the number of displaced atoms $\mathbf{N_d}$ that can be created by a primary recoiled host atom is given by:

$$\mathbf{N_d} = \frac{\boldsymbol{\kappa}(\mathbf{E_t} - \widehat{\mathbf{E_e}})}{\mathbf{2E_d}} = \frac{\boldsymbol{\kappa}\hat{\mathbf{E}}}{\mathbf{2E_d}}, \hat{\mathbf{E}} > \frac{\mathbf{2E_d}}{\boldsymbol{\kappa}} \qquad \text{Equation 5.3}$$

where $\hat{\mathbf{E}}$ is the mean energy possessed by the primary recoiled host atom, $\widehat{\mathbf{E_e}}$ is the average energy lost due to electron excitation during the cascade, and $\boldsymbol{\kappa}$ is the displacement efficiency factor not dependent on the incoming ion, energy of the recoiled atom and temperature.

In an ideal situation in which the host atom has negligible binding energy and maximum energy is transferred to the host atom by the incident ion, the measured values of $\mathbf{E_t}$ for the C-FePt system lies in the range of 160-200 eV. On the other hand, the values of $\mathbf{E_d}$ for Fe and Pt, according to the American Society for Testing of Materials (ASTM) standard [19], are 40 and 70 eV respectively. Therefore, the occurrence of cascade mixing is highly probable.

Similarly, the secondary recoiled host atoms can further displace additional host atoms in the layer. Thus, atomic mixing was generated in the recording layer due to continuous recoil and collision cascades of the Fe and Pt atoms. These dislocated host atoms occupy the interstitial sites, leaving behind empty lattice sites. In addition, given that the ToF-SIMS study has established the occurrence of the C^+ ions navigating deeper into the recording layer [Figure 5.8(c)], it is conceivable that the collision cascade diverging out of each of these incident ions would also have shifted further into the magnetic layer.

To summarize, the channeled C^+ ions, on their passage through the FePt layer, produce recoil- and cascade-based atomic mixing before, most likely, coming to rest at an interstitial site. Possible interstitial sites in the $L1_0$ FePt structure are (½, ½, ½) and (½, 0, 0). Both the interstitial sites have a radius of 0.561 Å. The radius of the C atom is known to be 0.78 Å [20]. Therefore, the C^+ ions, upon coming to rest and attempting to occupy interstitial sites, are bound to further disrupt the atomic rearrangement of the recording layer. In short, even a small number of C^+ ions coming to rest after traversing a depth of >2 nm in the recording layer are capable of creating lattice disorder and this is reflected in diminished magnetic properties. The estimation of the interstitial radius is shown on the next page.

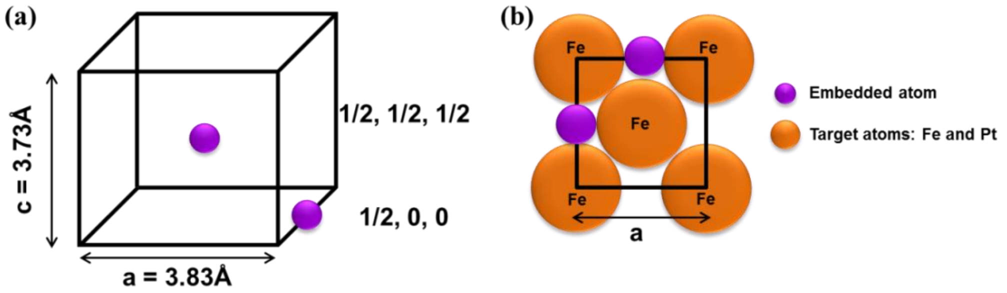

Figure 5.10 (a) Possible interstitial sites in fct-FePt and (b) interstitial sites being occupied by the embedded atom in the Fe layer of a fct unit cell.

(½, ½, ½) and (½, 0, 0) are the possible interstitial sites in the fct $L1_0$ FePt structure as shown in Figure 5.10(a). The interstitial site (½, 0, 0), present along the <100> direction, is considered for this discussion. The host atoms surrounding this particular interstitial location are Fe atoms. It is evident from Figure 5.10(b) that:

$$\mathbf{R_{Fe}} = \frac{\sqrt{2}\mathbf{a}}{4} = \frac{\sqrt{2}\times 3.83\text{Å}}{4} = \mathbf{1.354}\ \text{Å} \qquad \text{Equation 5.4}$$

$$\mathbf{2R_{Fe}} + \mathbf{2r_{int}} = \mathbf{a} = \mathbf{3.83}\ \text{Å} \qquad \text{Equation 5.5}$$

$$\mathbf{r_{int}} = \frac{3.83-(2)(1.354)}{2} = \mathbf{0.561}\ \text{Å} \qquad \text{Equation 5.6}$$

where $\mathbf{R_{Fe}}$ is the radius of Fe atom, $\mathbf{r_{int}}$ is the radius of the interstitial site, and **a** is the lattice parameter along *a*-axis of the fct FePt crystal. Similar calculations also show the $\mathbf{r_{int}}$ at (½, ½, ½) site to be 0.561 Å. The radius of the C atom is known to be 0.78 Å [20]. Since the radius of the C^+ ions is larger than the radius of the interstitial site, the ions will perturb the lattice arrangement while attempting to occupy these sites.

5.5 Summary and Scope of the Study

- **From tribological perspective:** The study demonstrates clearly that low energy C^+ ion embedment at 350 eV in FePt films could not be confined to the top ~2 nm of the media surface. The smaller sized C^+ ions initiated an order-disorder transformation in the *$L1_0$* FePt layer while traversing through it. This led to the deterioration of the magnetic properties of the recording layer. The damage was slightly suppressed by increasing the thickness of the magnetic film. The Gaussian tail of the implanted C^+ ions and recoiled Fe and Pt atoms extended to a depth of ~8 nm in the 10 nm thick FePt layer. Therefore, it was highly unlikely for the FePt films with thicknesses of $\leq$10 nm to retain the perpendicular magneto-crystalline anisotropy that was necessary to exhibit high out-of-plane and reduced in-plane coercivities. The damage induced in 15 nm thick FePt films *via* this surface modification technique was less severe. Nevertheless, such thick films, prior to embedding, display degraded *c*-axis texture, leading to poorer magnetic properties. Therefore, FePt films of thicknesses $\geq$10 nm are not suitable for studying the recording performance expected from the next-generation FePt media. In other words, tribologically useful FePt film surfaces could be achieved but at the expense of deteriorating chemical ordering.

Previously, commercial CoCrPt-based media had been subjected to C^+ ion embedment to achieve better tribological properties. However, no adverse impact on the macro-magnetic properties of these media was reported [21, 22]. This may be due to a host of reasons such as higher film thickness, different crystallography, and the absence of any chemical ordering of the recording layer. On the other hand, *$L1_0$* FePt has an fct-ordered phase arising from the stacking of alternating layers of Fe and Pt atoms. Therefore, bombarding the FePt film with C^+ ions created discrepancies in the ordered crystal arrangement which, in turn, adversely impacted the associated magneto-crystalline anisotropy.

- **For implementation in bit patterned media (BPM) fabrication:** Apart from showcasing the technological consequences brought about by the C^+ ion embedding technique in FePt films, the experiments also highlighted the cause behind the low energy embedment (SM III)-induced lattice damage. The lattice damage in the 5 nm thick $L1_0$ FePt films led to a drastic reduction in its out-of-plane coercivity by 86% (from 15 to 2 kOe). Also, the presence of non-magnetic C atoms in the magnetic layer decreased its saturation magnetization from ~900 to ~600 emu/cc. The magnetic properties of $L1_0$ FePt films have formerly been quenched using high energy ion implantation with the goal to achieve BPM [23]. Implantation-assisted BPM fabrication eliminates surface planarization of the media. However, higher energies of the order of a few keV had to be used to ensure that the Gaussian peak of the ions which are being implanted lies in the middle of the recording layer. The use of higher energies are accompanied with undesired lateral movement of host/implanted atoms over distances extending to a few nanometers. This is of consequence if the bit density being targeted in BPM is >1 Tb/in^2. The spacing between the bits is reduced to ≤ 12 nm and thus the lateral straggle reduces the bit size and deteriorates their magnetic behavior. Low energy ion embedment (< 500 eV) is a suitable technique for fabricating BPM since lateral straggle should scale down with decrease in ion embedment energy. This is explored in Chapter 6.

References

[1] Mark H. Kryder *et al.*, Heat assisted magnetic recording, Proc. IEEE, **96**, 1810 (2008).

[2] A. C. Ferrari, Diamond-like carbon for magnetic storage disks, Surf. Coat. Technol. **180**, 190 (2004).

[3] P. Bernhard, Ch. Ziethen, R. Ohr, H. Hilgers, and G. Schönhense, Investigations of the corrosion protection of ultrathin a-C and a-C:N overcoats for magnetic storage devices, Surf. Coat. Technol. **180**, 621 (2004).

[4] L. Wu, Modelling and simulation of the lubricant depletion process induced by laser heating in heat-assisted magnetic recording system, Nanotechnology **18**, 215702 (2007).

[5] H.-S. Zhang and K. Komvopoulos, Surface modification of magnetic recording media by filtered cathodic vacuum arc, J. Appl. Phys. **106**, 093504 (2009).

[6] E. Rismani, M. A. Samad, S. K. Sinha, R. Yeo, H. Yang, and C. S Bhatia, Ultrathin Si/C graded layer to improve tribological properties of Co magnetic films, Appl. Phys. Lett. **101**, 191601 (2012).

[7] T. Bublat and D. Goll, Temperature dependence of the magnetic properties of $L1_0$-FePt nanostructures and films, J. Appl. Phys. **108**, 113910 (2010).

[8] M. A. Samad, S. Xiong, L. Pan, H. Yang, S. K. Sinha, D. B. Bogy, and C. S. Bhatia, A novel approach of carbon embedding in magnetic media for future head/disk interface, IEEE Trans. Magn. **48**, 1807 (2012).

[9] S. D.Granz and M. H. Kryder, Granular $L1_0$ FePt (001) thin films for heat assisted magnetic recording, J. Magn. Magn. Mater. **324**, 287 (2012).

[10] A. Onda, T. Ochi, and K. Yanagisawa, Hydrolysis of cellulose selectively into glucose over sulfonated activated-carbon catalyst under hydrothermal conditions, Top Catal. **52**, 801 (2009).

[11] J. W. Mayer, L. Eriksson, and J. A. Davies, *Ion Implantation in Semiconductors*, Academic Press, New York and London (1970).

[12] J. F. Ziegler and R. F. Lever, Channeling of ions near the silicon <001> axis, Appl. Phys. Lett. **46**, 358 (1985).

[13] C. Liua, T. J. Klemmera, N. Shuklaa, X. Wua, D. Wellera, M. Tanaseb, and D Laughlin, Oxidation of FePt nanoparticles, J. Magn. Magn. Mater. **266**, 96 (2003).

[14] R. G. Wilson and G. R. Brewer, *Ion Beams: With Application to Ion Implantation*, John Wiley & Sons, New York (1973).

[15] M. Nastasi, J. Mayer, and J. K. Hirvonen, *Ion-Solid Interactions: Fundamentals and Applications*, Cambridge University Press (2013).

[16] M. I. Norgett, M. T. Robinson, and I. M. Torrens, A proposed method of calculating displacement dose rates, Nucl. Eng. Des. **33**, 50, (1975).

[17] M. T. Robinson and I. M. Torrens, Computer simulation of atomic-displacement cascades in solids in the binary collision approximation, Phys. Rev. B **9**, 5008 (1974).

[18] G. H. Kinchin and R. S. Pease, The displacement of atoms in solids by radiation, Rep. Progr. Phys. **18**, 1 (1955).

[19] ASTM E521-89, *Neutron Radiation Damage Simulation by Charged-Particle Irradiation*, ASTM Book of Standards 12.02, (1990).

[20] H. O. Pierson, *Handbook of Refractory Carbides & Nitrides: Properties, Characteristics, Processing and Applications*, William Andrew (1996).

[21] M. A. Samad, E. Rismani, H. Yang, S. K. Sinha, and C. S. Bhatia, Overcoat free magnetic media for lower magnetic spacing and improved tribological properties for higher areal densities, Tribol Lett. **43**, 247 (2011).

[22] M. Shakerzadeh, S. N. Piramanayagam, R. Ji, B. Varghese, H. K. Tan, and M. Bosman, The effect of high deposition energy of carbon overcoats on perpendicular magnetic recording media, Appl. Phys. Lett. **103**, 161604 (2013)

[23] N. Gaur *et al.*, Lateral displacement induced disorder in $L1_0$ FePt Nanostructures by ion-implantation, Sci Rep. **3**, 1907 (2013).

CHAPTER 6

Creating alternate magnetic and non-magnetic regions in $L1_0$ FePt using low energy C^+ ion embedment

6.1 Motivation

Irradiating magnetic media with energetic ions to create bit patterned media (BPM) is an attractive solution to eliminate planarization of media surfaces (refer to Chapter 2). From the study carried out in Chapter 5, it is evident that C^+ ion energies <1 keV can significantly destroy the out-of-plane magnetocrystalline anisotropy of the FePt layer, even though the Gaussian peak lies close to the FePt surface. This is due to the channeling effect of the C^+ ions. Previously, high energy ion implantation in media materials, including the high anisotropy FePt films, had been carried out to achieve the aforementioned state of the magnetic media to create a matrix of alternating magnetic and non-magnetic islands for BPM fabrication [1-4]. The Gaussian peak of the implantation profile lies at the center of the recording layer to ensure that the ions navigate the entire depth of the FePt layer to cause the necessary damage. Figures 6.1(a) and (b) show the TRIM simulated Gaussian peak positions of two ion bombardment processes – low energy embedment and high energy implantation of C^+ ions in FePt films. This comparison has been provided to demonstrate that even though the Gaussian peak positions of the C^+ ions obtained from these two irradiation processes are different, the damage to the magnetic properties are comparable [Ref. 4 and Chapter 5]. Therefore, low energy embedment appears to be a more viable option over high energy implantation since there is less power consumption associated with the former.

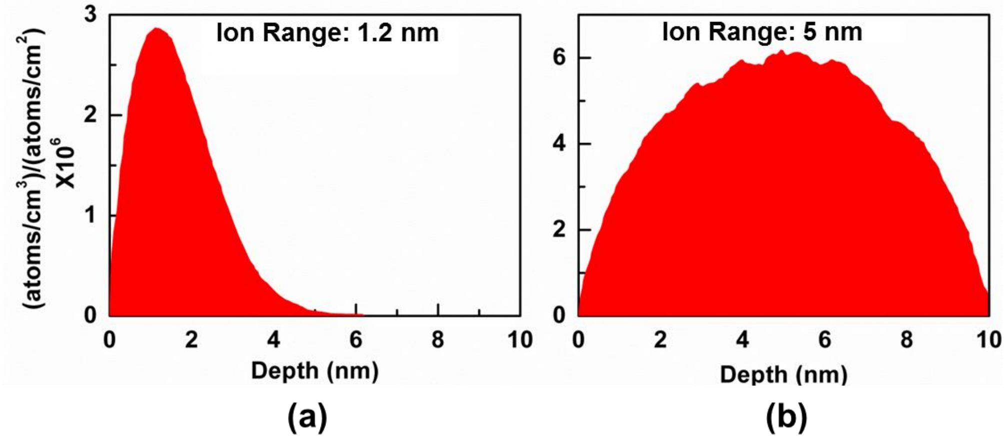

Figure 6.1 Comparison of the ion ranges when C^+ ion bombardment is carried out in FePt at (a) 350 eV and (b) 4 keV. TRIM software was used.

More importantly, ion embedment has the potential to tackle a major bottleneck associated with high energy ion implantation − lateral straggle of the ions into the masked regions [4, 5]. This is illustrated in Figure 6.2. The incoming ions do not have directionality and therefore their lateral movement into the areas beneath the lithographically designed masks is inevitable. The host atoms present underneath the masks are also displaced from their lattice positions by these ions, thereby causing an undesirable change in the magnetic properties of the 'bit' being designed. In FePt, particularly, the chemically ordering changes from $L1_0$ to $A1$ in the bit region [5]. The plot of lateral straggle (simulated using TRIM) versus the energy of the incoming C^+ ions is shown in Figure 6.3(a). The lateral straggle decreases with reduction in energy of the bombarding ions. The C^+ ions, moving along the depth of the FePt layer and laterally, generate a collision cascade. Recoil host atoms are produced. The damage cascade resulting from each of these C^+ ions and recoil host atoms can be simulated using TRIM until their energy drops below the lowest displacement energy [6]. This multiple collision-induced damage area will be larger than the straggle area of the C^+ ions. The damage cascades produced by the C^+ ions when embedment is carried out at 350 eV and 4 keV are depicted in Figures 6.3(b) and (c), respectively. The collision cascade-induced damage area along the lateral direction (z-axis) is smaller when ion energy of 350 eV is used instead of 4 keV. This further supports our proposal of creating FePt-based BPM *via* C^+ ion embedment at energies ranging between 100−500 eV. Therefore, in the forthcoming sections, experiments have been carried out to create '$L1_0$ FePt-based BPM' at areal densities > 1 Tb/in^2. Efforts have been directed towards understanding the impact of lateral straggle in patterned FePt. The areal density limit imposed on ion embedment assisted-BPM by lateral straggle has also been debated.

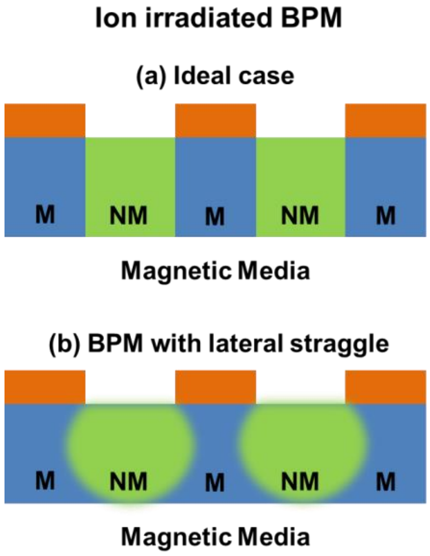

Figure 6.2 Schematic of ion irradiated BPM in (a) an ideal scenario and (b) when the concept of lateral straggle is introduced.

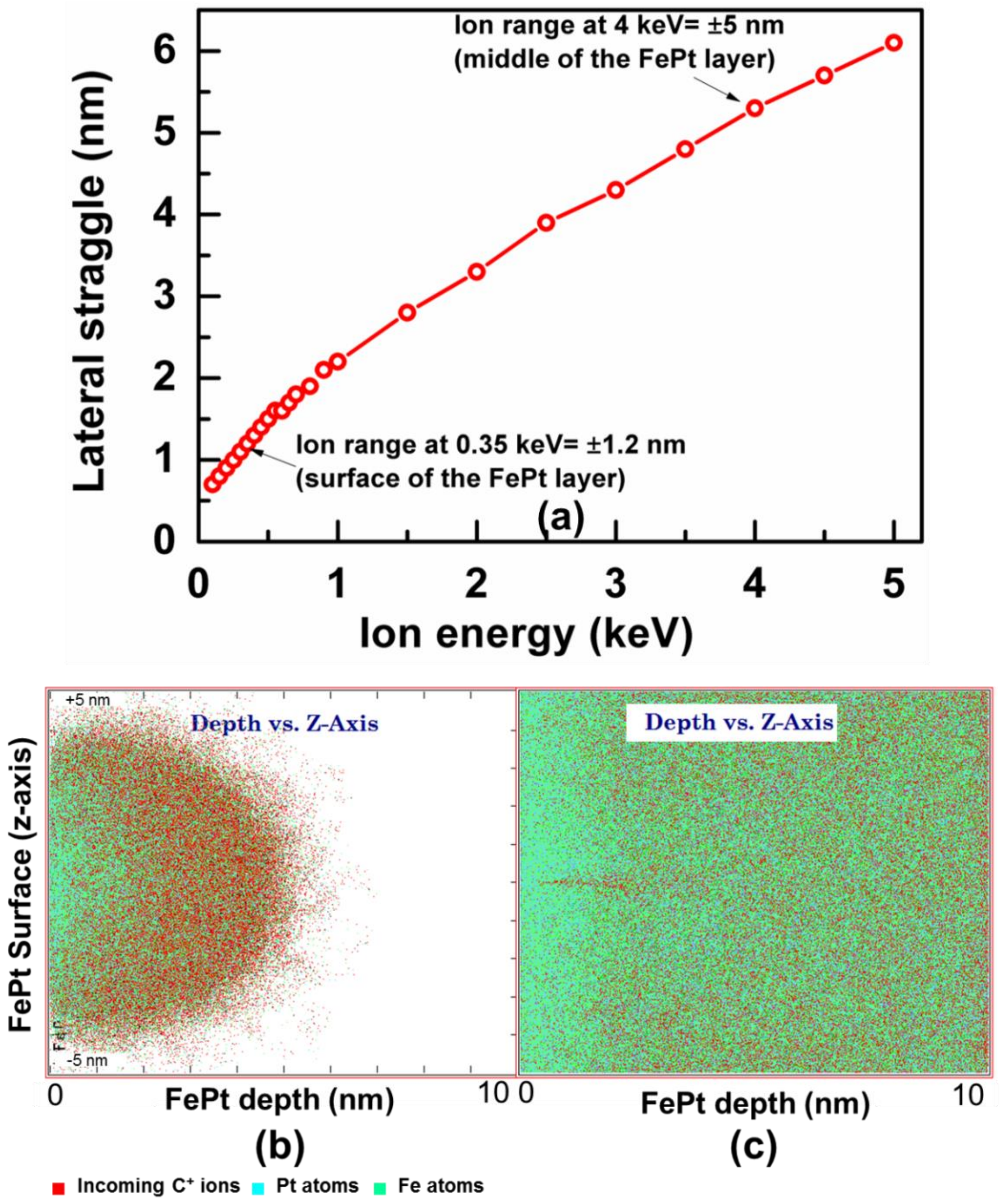

Figure 6.3(a) Lateral straggle versus ion energy of C^+ ions bombarded into FePt layer. (b) and (c) are the pictorial representations of the lateral movement of the ions and the host atoms when embedment is carried out at 350 eV and 4 keV. It is viewed along the cross-section of 10 nm thick FePt.

6.2 Experimental Details

- **FePt media stack used for the study:** The FePt media stacks designed previously in Chapter 4 and 5 offered root mean square surface roughness values (R_{rms}) of ~1.6 nm. Patterning of high density structures (of areal density ~1.6 Tb/in^2) on such surfaces is not easy. Therefore, the Ar gas pressure used during the deposition of the FePt layer was increased to ~5 mTorr. Slightly smoother surfaces (R_{rms} ~0.9 nm) were obtained at such higher Ar pressures. Nano-masks of diameter ~10 nm could then be uniformly patterned atop these FePt films. The FePt surfaces were then capped with a ~1 nm thin layer of amorphous silicon at room temperature (RT) to improve the adhesion of the resist to the film. The deposition temperature of FePt was kept constant at 600° C to achieve the desired $L1_0$ phase. The deposition conditions have been shown along with the schematic of the FePt stack in Figure 6.4. The substrate was changed from glass to silicon to avoid charging effects during patterning using the electron beam lithography (EBL) tool.

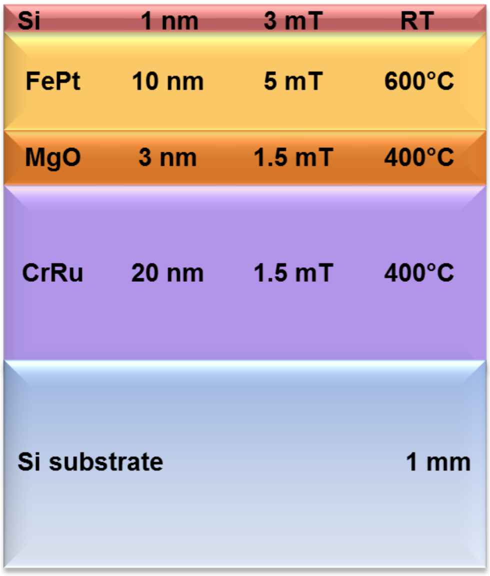

Figure 6.4 Magnetic media stack used for studying BPM at an areal density of ~1.6 Tb/in^2.

The SEM and AFM images of the FePt surfaces achieved using the above-mentioned deposition conditions are presented in Figure 6.5. It can be seen that the FePt grains are not granular. They appear connected to one another (continuous), which is favorable for BPM fabrication. Fewer grain boundaries within each patterned bit reduces the jitter noise from them.

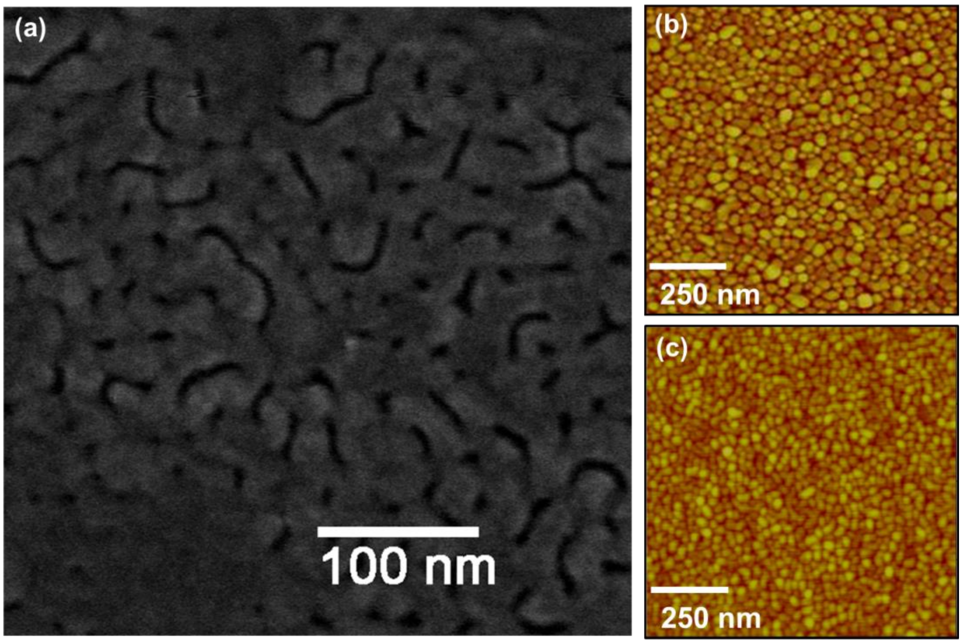

Figure 6.5 (a) SEM image of the FePt surface coated with ~1 nm thin Si. Two-dimensional AFM scans of the FePt surfaces grown using the deposition conditions provided in Section 5.2 of Chapter 5 (R_{rms} ~1.6 nm) and the deposition conditions given in Section 6.2 (R_{rms} ~0.9 nm) have been shown in (b) and (c), respectively.

- **Procedure for patterning an areal density of ~1.6 Tb/in^2:** A 25 nm thick hydrogen silsesquioxane (HSQ) resist was spin-coated on the FePt media samples. HSQ dots of diameter ~10 nm and pitch ~20 nm were defined using the EBL tool (for details on the EBL system used, refer to Section 3.2.2 in Chapter 3). The accelerating voltage and the beam current used for patterning these features over an area of ~3600 µm^2 were 100 kV and 200 pA, respectively. The samples were then developed in an aqueous solution of 1% NaOH (w/w) and 4% NaCl (w/w) for a minute followed by a deionized (DI) water rinse. The excess water from the substrate surface was removed by using a nitrogen blow-gun. Figure 6.5 shows the SEM images of the FePt surfaces masked with high density HSQ pillars.

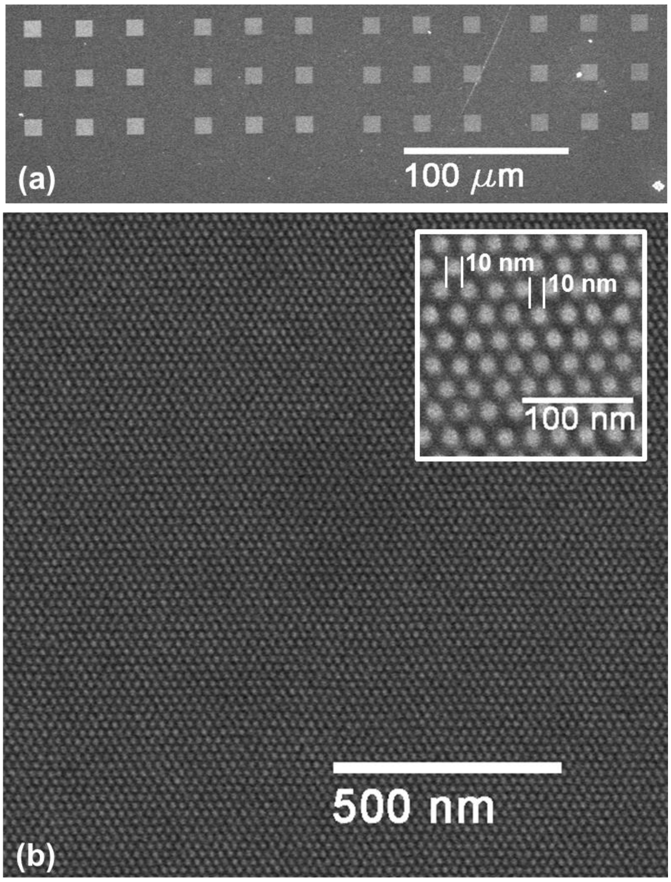

Figure 6.6 (a) Low magnification SEM image of the areas which have been patterned using the EBL (brighter appearing square regions). Each square is 10 µm by 10µm and there are 36 similar squares on the sample. (b) Higher magnification SEM image of the patterns in each square amounting to an areal density of ~1.6 Tb/in^2. The inset shows a further magnified view of (b).

These densely masked FePt films were embedded with C^+ ions at 350, 175 and 100 eV using the FCVA technique at Nanofilm Tech. Int. Pte. Ltd. (Singapore). Bare FePt films without any patterns were also subjected to embedment under similar conditions. This was done in order to draw a comparison between the magnetic properties of patterned and bare FePt films post-embedment. Unlike in Chapter 5, DC biasing was used instead of pulse biasing. The embedment conditions are summarized in Table 6.1. The base pressure of the system was maintained at 7.5 × 10^{-7} Torr. The arc current used during all the three embedment processes was 40 A. As mentioned previously, the ion dose for these experiments could not be estimated as the FCVA system was not instrumented with a Faraday cup or Pearson coil to accumulate charged particles in vacuum. The lateral straggle values for different embedment energies, simulated using TRIM, are also provided below.

C^+ ion embedment energy (eV, DC bias)	**Time (seconds)**	**Any Ar^+ ion etching prior to embedment**	**Simulated lateral straggle of C^+ ions (nm)**
350	100	No	±1.2
175	100	No	±1.0
100	100	No	±0.7

Table 6.1 Experimental conditions used for studying ion embedment assisted BPM fabrication. Simulated lateral straggle values have also been provided.

6.3 Results: Out-of-plane and in-plane loops of the FePt samples patterned at different energies

Figures 6.7(a) and (b) show the out-of-plane and in-plane hysteresis loops of the reference FePt film, respectively. The out-of-plane coercivity is ~10 kOe, which is lower than the value previously achieved in Chapter 4 and 5. During the deposition of the FePt layer, the Ar pressure was raised to 5 mTorr which, in turn, caused increased collisions of the Ar species with the Fe and Pt atoms in the gas phase. The mean free path (MFP) of these sputtered elements decreased. As a result, the kinetic energies of the adatoms on the substrate surface were reduced, which further deteriorated their chemical ordering. This was reflected in the reduced out-of-plane coercivity of the reference film. Squarer hysteresis and larger out-of-plane coercivity of ~10 kOe than that along the in-plane direction (1.5 kOe) indicated the presence of the $L1_0$ phase in the reference film [7]. Microstructural evolution of the FePt layer was also affected [Figure 6.5(a)]. A more continuous, as opposed to granular, FePt film was formed.

Figures 6.7(c) and (d) show the out-of- and in-plane coercivities, respectively, of the patterned FePt films after embedding C^+ ions at different energies. Figures 6.8 (a) and (b) show the variation in the out-of- and in-plane coercivities of the FePt films with and without patterns when subjected to different embedment energies. The hysteresis loops and coercivities after carrying out each embedment are discussed below.

After embedment of C^+ ions at 350 eV: Optical microscopy was carried out on the patterned FePt films. The imaging showed the absence of the high density patterned regions. The nano-patterns were etched away during ion bombardment at 350 eV. These patterned films exhibited an out-of-plane coercivity of ~0.6 kOe and an in-plane coercivity of ~0.2 kOe. It is clearly visible that when embedment was carried out at 350 eV, both out-of- and in-plane coercivities of the patterned FePt films matched the values obtained for those embedded FePt films which had no nano-masks [Figures 6.8(a) and (b)]. This suggested that due to the removal of the HSQ pillars during ion bombardment, the C^+ ions were embedded throughout the FePt film and not at selected locations. The bare FePt films embedded at 350 eV displayed a drastic reduction in both out-of- and in-plane coercivities to ~0.2 kOe [Figures 6.8(a) and (b)] with regard to the reference film [Figures 6.7(a) and (b)]. In other words, such high energy embedment of C^+ ions damaged the crystallinity of the FePt film.

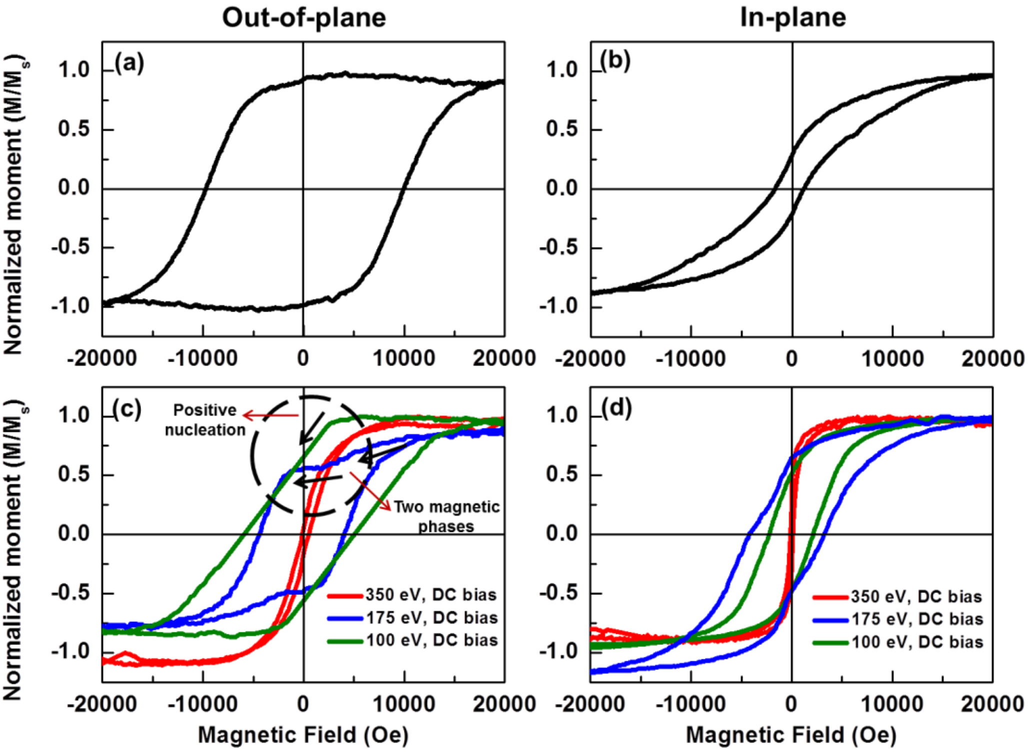

Figure 6.7 Out-of-plane hysteresis loops of (a) reference *$L1_0$* FePt sample and (c) patterned FePt at different energies, and in-plane hysteresis loops of (b) reference *$L1_0$* FePt sample and (d) patterned FePt at different energies.

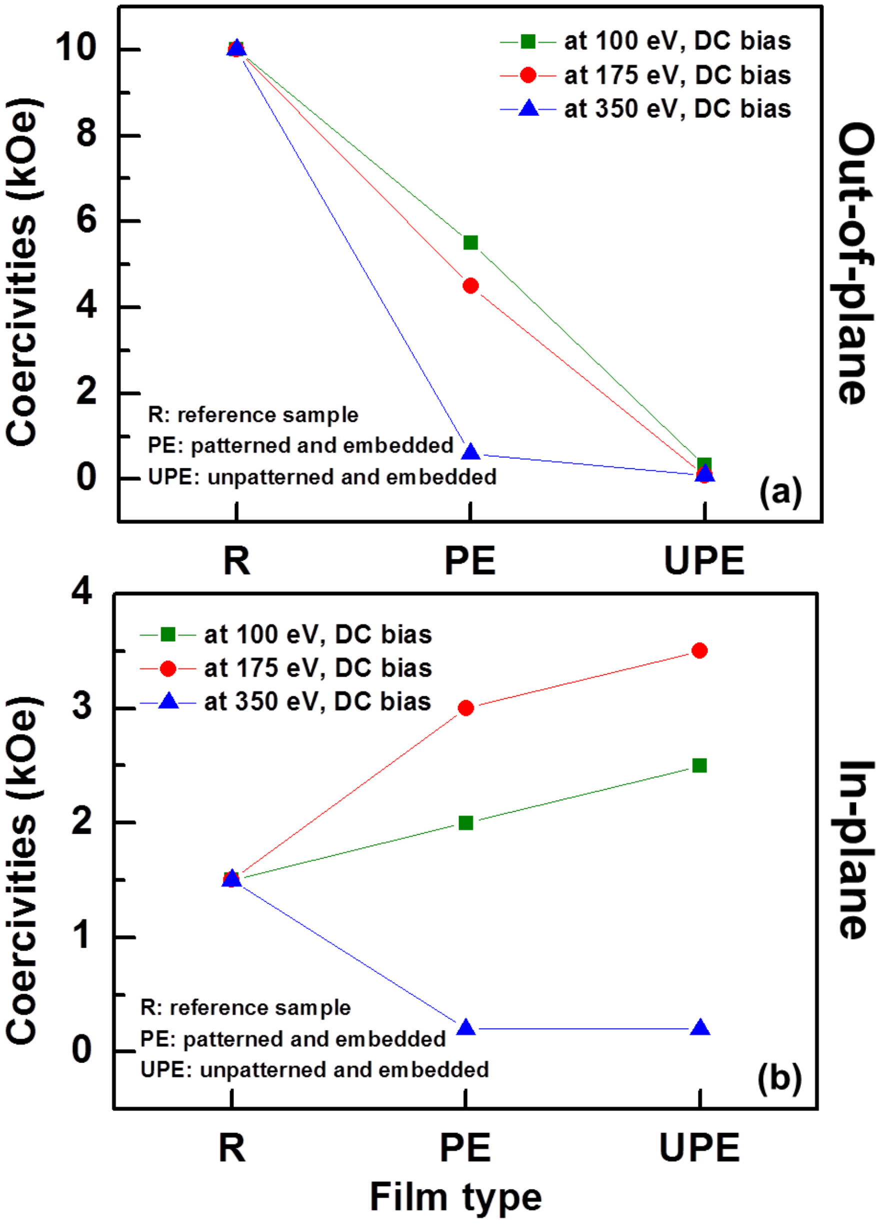

Figure 6.8 Mapping (a) out-of-plane and (b) in-plane coercivities of reference (R), and patterned FePt (PE) and bare FePt (UPE) films at different embedment energies.

After embedment of C^+ ions at 175 eV: The patterned regions on FePt were visible under the optical microscope after ion embedment at lower energy of 175 eV. After embedment at 175 eV, the patterned FePt films exhibited an out-of-plane coercivity of ~4.5 kOe and an in-plane coercivity of ~3 kOe [Figures 6.7(c) and (d)]. The difference between the out-of- and in-plane coercivities was not as large as the reference film. However, we can say that the $L1_0$ ordering was still present in these films since the out-of-plane coercivity was greater than the in-plane value. Furthermore, it can be seen from Figure 6.8(a) that the out-of-plane coercivity of the patterned FePt film (~4.5 kOe) was larger than the value obtained for bare FePt subjected to the same embedment conditions (~0.1 kOe). This indicated that bit isolation was attained in the FePt film masked with HSQ pillars – a necessary condition for creating BPM using ion irradiation. Alternate magnetic and non-magnetic regions were created. This out-of-plane coercivity value of the patterned FePt (~4.5 kOe), however, was lower than that of the reference $L1_0$ FePt film (~10 kOe). Lateral straggling of the ions into the masked regions is responsible for perturbing the fct-arrangement of several of the host atoms. This adverse impact is reflected in the appearance of two magnetic phases at remanance in the hysteresis loop [encircled region in Figure 6.7(c)]. This will be discussed in greater detail in Section 6.4. Surprisingly, unlike embedment at 350 eV, embedment at 175 eV might have induced an order-disorder transformation [Figures 6.7(b) and (d)]. The in-plane loop for patterned FePt [Figure 6.7(d)] appeared squarer than the reference in-plane loop [Figure 6.7(b)]. The in-plane coercivity of patterned FePt increased to ~3 kOe, which was slightly lower than the in-plane coercivity of the embedded bare FePt film [~3.5 kOe, refer to Figure 6.8(b)].

After embedment of C^+ ions at 100 eV: Analogous to ion bombardment at 175 eV, the patterned regions on FePt could also be seen under the optical microscope after ion embedment at 100 eV. The lateral straggle at 100 eV was expected to be smaller in comparison to the straggle value at 175 eV [Figure 6.3(a)]. Therefore, the undesirable effect produced by the lateral movement of the C^+ ions on the attainment of well-isolated bits should be lessened. The out-of-plane coercivity of patterned FePt increased to ~5.5 kOe, higher than the value obtained at 175 eV [Figure 6.7(c)]. It is also observed from Figure 6.8(a) that the out-of-plane coercivity was again lower than the value obtained for the reference $L1_0$ FePt sample (~10 kOe). However, it was more than that of the embedded bare FePt sample (~0.3 kOe). Therefore, similar to the embedment at 175 eV, bit isolation was present in these patterned FePt films as well. Embedding C^+ ions at 100 eV induced an order-disorder transformation in the regions not protected by the mask. The in-plane hysteresis loop of patterned FePt displayed squareness and a coercivity of ~2 kOe [Figure 6.8(d)], which was higher than the value achieved for the reference FePt film (~1.5 kOe) but slightly lower than that of the embedded bare FePt film [~2.5 kOe, refer to Figure 6.8(b)]. Larger out-of-plane and smaller in-plane hysteresis loops were attained for the FePt film when it was patterned at 100 eV instead of 175 eV. This demonstrated improved $L1_0$ ordering at reduced embedment energy. However, a positive nucleation [encircled in Figure 6.7(c)] was seen in the out-of-plane hysteresis loop of the patterned FePt film when it was embedded at 100 eV. The cause behind this observation is discussed below.

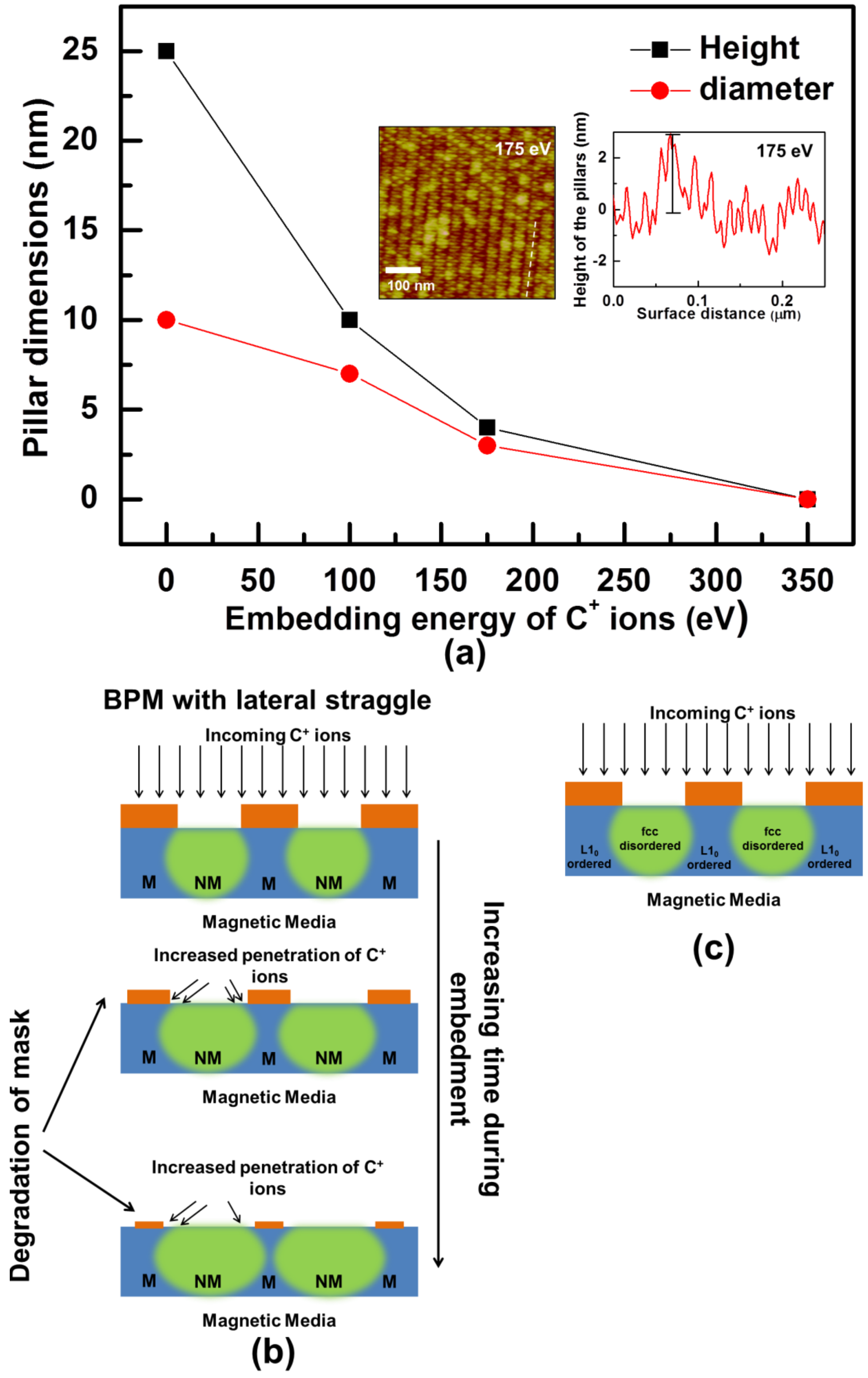

Figure 6.9 (a) Plot of pillar dimensions with increasing embedment energy. The insets show the AFM image and height profile of the patterns after embedment at 175 eV. (b) Illustration of gradual degradation of mask with time during the embedment process. (c) Schematic of FePt-based BPM which has alternate fct-ordered and fcc-disordered phases.

6.4 Discussion: Inferring lateral straggle from the out-of- and in-plane loops of the FePt samples

Inference from out-of-plane loops: It is clear from the results shown in Figures 6.7(c) and 6.8(a) that bit isolation was achieved when C^+ ion embedment was carried out at energies 100 and 175 eV. However, unlike the out-of-plane coercivity of the reference $L1_0$ FePt, the out-of-plane loops of the patterned FePt samples displayed reduced coercivities and anomalous behavior at and near remanance [encircled region in Figure 6.7(c)].

Embedment at 175 eV: After exposure to ion bombardment at 175 eV, two magnetic phases were observed in the hysteresis loop. It is known from Chapter 5 that the Gaussian peak in the embedment profile of the C^+ ions at 175 eV lies close to the FePt surface. Several C^+ ions traverse the entire depth of the FePt film, generating a damage cascade throughout their passage. Nonetheless, since the bulk of the C^+ ions are closer to the surface, the collision induced lateral damage to the fct-lattice structure will be larger closer to the surface of the FePt film than at the bottom. This is evident from Figure 6.3(b). The lateral damage decreases with increasing depth of the FePt layer. Therefore, it is likely that underneath the HSQ nano-masks, a relatively weaker perpendicular anisotropy region (soft magnetic region) is created in the top few nanometers of the FePt layer than at the bottom. The soft magnetic layer switches first, followed by the switching of the relatively hard magnetic layer (higher perpendicular anisotropy) present beneath it. There is another parameter which can add to the creation of the weaker anisotropy layer in the top few nanometers of the FePt layer – degradation of the mask. The height and diameter of the HSQ pillars were ~25 and ~10 nm, respectively. Figure

6.9(a) shows the change in the pillar diameter and height with different embedding energies. The AFM image of the nano-patterns and the corresponding height profile, after carrying out embedment at 175 eV, are also presented as insets in Figure 6.9(a). Both the height and diameter of these patterns decrease with an increase in the embedding energy. In other words, voluminous shrinkage of the patterns occurs during the embedment process. Therefore, degradation of the nano-mask results in a greater number of C^+ ions penetrating into the upper region of the FePt film. The straggle of these ions and the associated collision cascade could have further added to the creation of a softer magnetic layer just beneath the HSQ pillars. This phenomenon is illustrated in Figure 6.9(b).

Embedment at 100 eV: A higher out-of-plane coercivity was produced at 100 eV than at 175 eV. However, positive nucleation was observed during the magnetization reversal of the patterned islands from the hysteresis plot [Figure 6.7(c)]. Straggling of the C^+ ions into the FePt regions protected by the HSQ pillars was less at 100 eV than at 175 eV [Figure 6.3(a)]. In addition, the shrinkage in the mask dimensions was also less compared to that obtained at 175 eV [Figure 6.9(a)]. The pillar height and diameter had reduced to ~10 and ~7 nm, respectively. Therefore, cascade damage was induced by the lateral straggle of the C^+ ions, which penetrated the unmasked regions and the regions from where the pillars were etched away during the embedment process. This resulted in patterned FePt films with an out-of-plane coercivity value (5.5 kOe) lower than that of the reference sample (~10 kOe). Similar to ion bombardment at 175 eV, a weaker anisotropy region was created closer to the FePt surface (protected by the mask), which switches first (undergoes positive nucleation) and then aids the switching of the relatively hard magnetic layer (higher perpendicular anisotropy) present beneath it [8].

The variation in the abnormal behavior – positive nucleation and existence of two magnetic phases − observed at the remanance of the hysteresis loop after embedment at 100 eV and 175 eV could be due to the different values of the energies used for creating patterned FePt. The degree of degradation in the mask dimensions at different energy values [Figure 6.9(a)] could have also played a key role in this study.

Inference from the in-plane loops: The in-plane coercivities of the patterned FePt films after embedment at 100 and 175 eV exhibited a small yet significant increase from the reference value of 1.5 kOe to 2 and 3 kOe, respectively. The bare FePt films subjected to embedment at 100 and 175 eV displayed a marginal increase in the in-plane coercivity values – 2.5 and 3.5 kOe, respectively. The out-of-plane coercivities for both these films were $\leq$0.3 kOe. On the other hand, ion bombardment at 350 eV resulted in reducing both the in- and out-plane coercivities to ~0.2 kOe. It is likely that a random arrangement of Fe and Pt atoms was achieved after the film was exposed to high energy ion bombardment at 350 eV. In the case of embedment at 100 and 175 eV, these energy values were sufficient to create an order-disorder transformation of the FePt region which was not protected by the mask. A low anisotropy fcc phase was created, resulting in increased in-plane variants [7]. Therefore, an important conclusion from this study is that patterned FePt media fabricated using low energy ion embedment will consist of alternate $L1_0$ ordered and fcc disordered regions instead of magnetic and non-magnetic regions. This is illustrated in Figure 6.9(c).

The resolution limit of MFM restricts the imaging of magnetic domains in the sub-20 nm range. Therefore, 120 nm wide resist patterns (pitch = 200 nm) were created and embedded at 100 eV. The patterned sample was magnetized along one particular field direction and subjected to MFM (Figure 6.10). High anisotropy regions (higher contrast) separated by lower/weaker anisotropy regions (lesser contrast) were observed, indicating the creation of BPM.

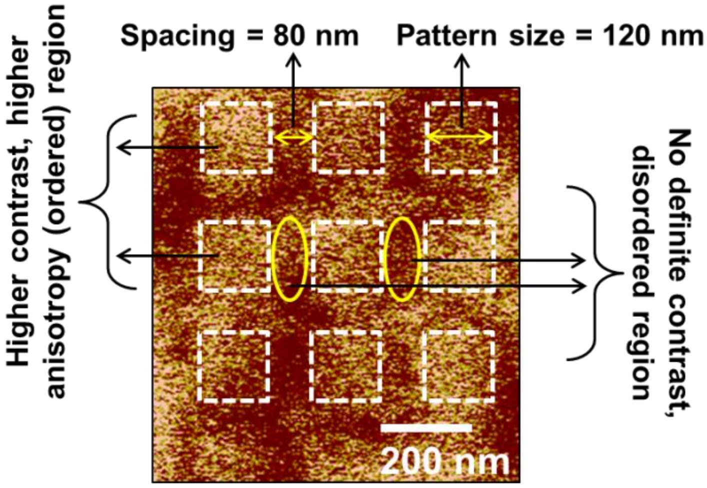

Figure 6.10 MFM image of 120 nm wide patterns (pitch = 200 nm). The resist used was ma-N 2401. The resist patterns were etched using O_2 plasma before subjecting the sample to MFM. This prevented the mapping of surface topography on the magnetic signal. (Phase = -0.5° to 0.5°)

6.5 Summary, Scope of Improvement and Limitations of the Study

- $L1_0$ FePt-based BPM fabrication using low energy C^+ ion embedment at an areal density of 1.6 Tb/in^2 was demonstrated. Due to the use of low ion energy, a matrix of high perpendicular anisotropy ($L1_0$ ordered) and low in-plane anisotropy (fcc phase) regions was produced. The surface roughness measured before and after ion embedment was approximately equal (R_{rms} ~0.9 nm). Hence, the technique shows that if further optimization can be carried out, then planarization after BPM fabrication is not essential.

- Several bottlenecks were encountered during the creation of FePt patterned media via C^+ ion embedment. Lateral movement of these C^+ ions created weaker anisotropy regions underneath the nano-masks. Also, degradation of these HSQ masks during embedment resulted in the higher penetration of the C^+ ions into the 'bit' region. These issues pose limitations on achieving areal densities >1.6 Tb/in^2 in BPM employing the ion irradiation technique. The use of other ion species which can also produce the desired channeling effect can be taken into consideration. This is discussed in detail in Chapter 8. Preventing the shrinkage of nano-masks during high energy embedment can also restrict the cascade damage induced by the incoming ions. Areal density of ~2Tb/in^2 may be achievable.

- Low energy embedment is useful in reducing the lateral straggle. However, decreasing the embedment energy below a certain value may not create the desired disordered region between two high anisotropy magnetic regions. Therefore, optimization of the lower energy limit is crucial and has been listed in future work in Chapter 8.

- Due to equipment limitation, the effect of varying ion doses on the creation of patterned media could not be studied. However, such a study is crucial and has been stated as one of the future works in Chapter 8. Here, a study on the effect of lateral straggle of the C^+ ions on patterned FePt media has been presented. The lateral straggle of the C^+ ions was quantified using simulation and its associated effects were studied in detail. Efforts are now being directed towards measuring the lateral straggle through experiments.

References

[1] K. Sato *et al.*, Magnetization suppression in Co/Pd and CoCrPt by nitrogen ion implantation for bit patterned media fabrication, J. Appl. Phys. **107**, 123910 (2010).

[2] T. Hinoue, K. Ito, Y. Hirayama, T. Ono, and H. Inaba, Magnetic properties and recording performances of patterned media fabricated by nitrogen ion implantation, J. Appl. Phys. **109**, 07B907(3) (2011).

[3] C. Choi *et al.*, Fabrication and magnetic properties of nonmagnetic ion implanted magnetic recording films for bit-patterned media, IEEE Trans. Magn. **47**, 2532 (2011).

[4] N. Gaur *et al.*, Lateral displacement induced disorder in $L1_0$ FePt nanostructures by ion-implantation, Sci. Rep. **3**, 1907(7) (2013).

[5] N. Gaur *et al.*, Ion implantation induced modification of structural and magnetic properties of perpendicular media J. Phys. D: Appl. Phys. **44**, 365001(9) (2011).

[6] Particle interactions with matter, [online]. Available at: http://www.srim.org/

[7] Y-N. Hsu, S. Jeong, D. E. Laughlin, and D. N. Lambeth, Effects of Ag underlayers on the microstructure and magnetic properties of epitaxial FePt thin films, J. Appl. Phys. **89**, 7068 (2001).

[8] C. Kooy and U. Enz, Experimental and theoretical study of the domain configuration in thin layers of $BaFe_{12}O_{19}$, Philips Res. Rep. 15, 7 (1960).

CHAPTER 7

Effect of magnetic media's angstrom-scale surface roughness on self-assembly

7.1 Motivation

Self-assembly of block copolymers has been identified as a potential candidate for high density fabrication of nanostructures [1-9]. The flexibility of self-assembly technique lies in the fact that it is scalable at sub-20 nm dimensions, and is a fast and cost-effective nanofabrication method that is ideal for fabricating etch masks necessary in bit patterned media (BPM) [10, 11]. More importantly, guided self-assembly enables the ordering of features over large areas in a circumferential manner on disk platters (refer to Chapter 2 for more details). Therefore, this technique is being extensively studied and exploited for possible application in next-generation BPM-based hard disk drives (HDDs).

It is crucial that the bit size and spacing are controlled in a stringent fashion to avoid issues such as adjacent bit erasure and increased jitter. Therefore, it is necessary to control the dimension, geometry and interspacing of the blocks. This can be achieved by tuning their molecular weight or by employing a blend of block copolymers and homopolymers [12]. Thermal annealing of the block copolymers [13] as well as application of localized electric [14] and large amplitude oscillatory shear fields [15] to the spin-coated films are effectual in dictating the alignment of blocks. An alternative and rapid route involving solvent vapor annealing of block copolymer films has also been proven to be effective in regulating the orientation and morphology of the microdomains [16-21].

It should be noted that almost all these self-assembly studies have been carried out on 'idealized' surfaces such as highly polished silicon or single crystal substrates [1-11]. There has hardly been any emphasis on the effect of surface roughness of the substrate on the self-assembly of block copolymers. Hence, it is not clear as to what factors originating from the substrate surface might adversely affect the reliability and reproducibility of self-assembly.

Magnetic thin films, produced by magnetron sputtering, exhibit nanoscopic surface roughness [22, 23]. Depending on the sputtering conditions such as target power, pressure, temperature and seed-layer, the degree of surface roughness can be varied on an angstrom-scale, giving rise to either continuous or granular magnetic media. Since self-assembly is a potential candidate for high density-BPM fabrication, it will be ideal to carry out a systematic study of the self-assembly of block copolymers on these media surfaces with varying roughnesses. In this chapter, the effect of angstrom-scale surface roughness on the self-assembly of polystyrene-polydimethylsiloxane (PS-*b*-PDMS) block copolymers using solvent annealing is investigated. In addition, the efficacy of self-assembly employing two solvent annealing systems as a function of surface roughness is also studied. Furthermore, this work provides an insight into the different aspects which need to be taken into consideration for large area patterning employing self-assembly.

7.2 Experimental Details

Five different media surfaces with roughness varying on the angstrom-scale were chosen for this study. The magnetic media and their corresponding deposition conditions are listed below.

- **Continuous and granular CoCrPt-SiO$_2$ [Figures 7.1 (a) and (b)] −** All the layers of CoCrPt-SiO$_2$ media were deposited at room temperature. Argon gas was used for deposition. To improve the adhesion of the deposited layers to the glass substrate, a Ta layer was grown on it. CoTaZr alloy was employed as the soft magnetic underlayer essential for perpendicular magnetic recording. A second Ta layer was used as the seed layer to provide a clean and smooth surface to the underlayer. In the case of continuous media, a single Ru interlayer was deposited at low pressure (3 mTorr) to promote a good crystallographic texture of the CoCrPt-SiO$_2$ magnetic layer (6 mTorr) [Figure 7.1(a)]. On the other hand, the granular media comprised two Ru interlayers. The first Ru layer improved the texture, while the second Ru layer, grown at a higher pressure (60 mTorr), caused grain segregation in the top recording layer (deposited at a pressure of 60 mTorr), leading to a higher surface roughness [Figure 7.1(b)] [24]. On both continuous and granular CoCrPt-SiO$_2$ media, carbon was deposited in the hydrogen and nitrogen environment to form a carbon overcoat on top of the media samples. The structural characterization of these media samples obtained using XRD are shown in Figures 7.2(a) and (b).

- **Granular FePt-C-Cu and FePt-C samples [Figures 7.1(c) and 7.1(d)]** − Similar to the fabrication of CoCrPt-SiO_2 media, argon was used as the sputtering gas. However, the layers were deposited at different temperatures. CrRu alloy was deposited at 400 ºC to give rise to a (002) texture which, in turn, induced the (001) texture in the FePt alloy through heteroepitaxy. A MgO layer grown at 400 ºC was introduced as a buffer layer between CrRu and FePt-C-Cu/FePt-C to avoid the diffusion of Cr into the recording layer. Moreover, it also promoted a good crystallographic texture of the recording layer. Both CrRu and MgO were deposited at low pressure (1.5 mTorr) to provide a smoother surface for the FePt-C-Cu and FePt-C layers to grow [Figures 7.1(c) and 7.1(d)]. The MgO layer was RF etched at 50 W for five minutes to planarize it further prior to the deposition of the FePt-C-Cu and FePt-C layers. FePt-C-Cu was deposited at 400 °C and 5 mTorr pressure. However, the desired $L1_0$ ordered phase was not attained as can be seen from Figure 7.2(c). On the other hand, FePt-C was deposited at 600 ºC and 3 mTorr pressure to obtain the $L1_0$ phase [Figure 7.2(d)]. Deposition at elevated temperatures was accompanied by grain growth, thereby resulting in higher roughness [25].

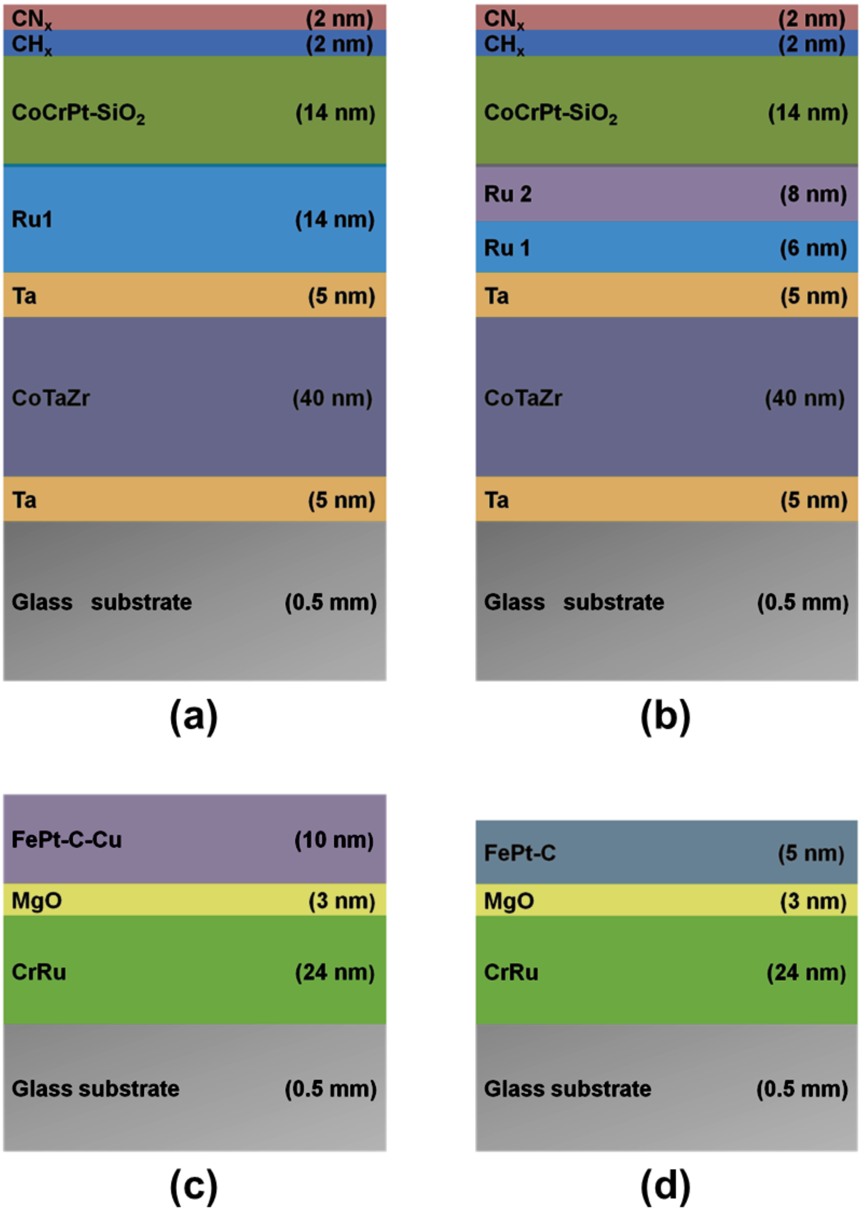

Figure 7.1 Schematic representations of different layers of (a) continuous CoCrPt-SiO$_2$, (b) granular CoCrPt-SiO$_2$, (c) granular FePt-C-Cu, and (d) granular FePt-C magnetic media.

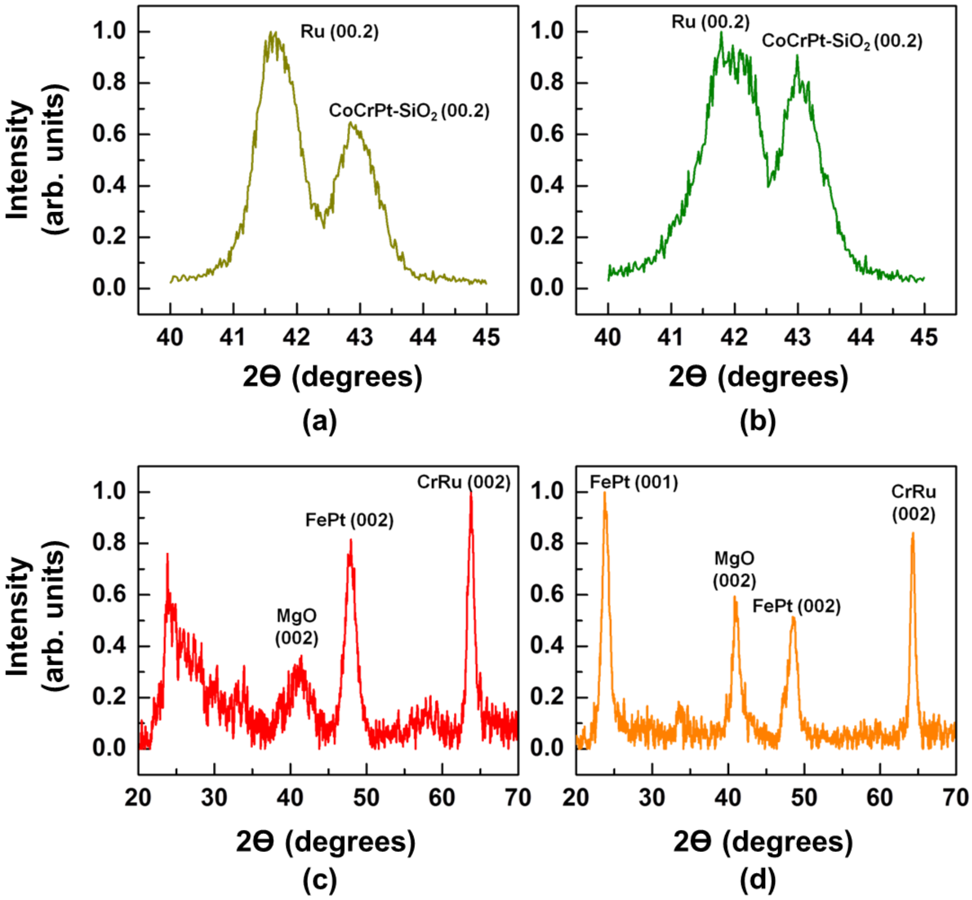

Figure 7.2 XRD of the media materials: (a) continuous CoCrPt-SiO_2, (b) granular CoCrPt-SiO_2, (c) granular FePt-C-Cu, and (d) granular FePt-C magnetic media**.**

PS-*b*-PDMS block copolymer preparation and its solvent annealing − PS-*b*-PDMS of molecular weight 51.5 kg/mol with PDMS volume fraction of 16% was chosen for the study as it leads to spherical morphology of the PDMS block in the PS matrix [2]. The presence of silicon in PDMS provides a high etch selectivity between the blocks. Moreover, the Flory-Huggins factor for phase separation of the blocks is large (0.26) compared to other block copolymers. This is an important parameter since it is a measure of the driving force for microphase separation [2, 26]. A 2.1 wt% solution of PS-b-PDMS in toluene was spun on the magnetic media (with or without TranSpin) to produce a ~54 nm thick film. The block copolymer film was solvent annealed in two different solvent (or solvent mixture) systems which were tetrahydrofuran (THF) and 6:1 toluene-heptane solvent mixture for nine hours. The solvent annealing process has been summarized in Section 3.2.1, Chapter 3. These solvents were chosen by comparing the solubility parameters of the blocks polystyrene (PS) and polydimethylsiloxane (PDMS) with those of the solvents used for annealing, i.e., toluene, heptane and tetrahydrofuran (THF), which are tabulated in Table 7.1 [26]. The solubility parameters of THF and toluene match that of PS, which ensures increased solubility of the block in these solvents and hence enhanced chain mobility. It is a similar case with PDMS and heptane. Annealing in the THF-heptane mixture did not yield acceptable results. From Table 7.1, it is seen that the solubility parameter of THF and heptane matches that of PS and PDMS, respectively. Since heptane is non-polar and THF is polar aprotic, it can be speculated that the polarity difference between the two solvents in the mixture may result in a heterogeneity in the vapor phase. THF was, therefore, replaced by non-polar toluene. When a 6:1 toluene-heptane mixture was employed, self-assembly was easily achieved on the least rough surfaces.

Solvent/polymer	**Hansen's Solubility Parameter (MPa)$^{1/2}$**
THF	18.6
Toluene	18.2
Heptane	15.3
PS	18.5
PDMS	15.5

Table 7.1 Hansen solubility parameters [26].

This was followed by a two-step etching process. A thin layer of PDMS surfaces above the PS matrix and needs to be removed to be able to observe the dots underneath. CF_4 plasma (3 sccm) at 50 W was used for five seconds to remove the top PDMS layer. This was followed by O_2 plasma (20 sccm) at 90 W for 20 seconds to remove the PS matrix and oxidize the PDMS dots to SiO_2. For the self-assembly of PS-*b*-PDMS on magnetic media with different surface roughnesses, chemical functionalization of the substrate is essential. Hydroxyl-terminated PS and PDMS brushes serve this purpose by bonding with the native oxide layer on top of the silicon substrates [2, 8]. On surfaces other than silicon, we found TranSpin™ (a proprietary material sold by Molecular Imprints, Inc.) to be an alternative choice. TranSpin is used as an adhesion promoter and for planarizing silicon wafers in step-and-flash nanoimprint lithography [27]. TranSpin has a water contact angle of 83° which is very close to that of PS (~90°) [28] compared to PDMS (110°) [29]. As a result, there is a preferential wetting of TranSpin and PS as opposed to PDMS. This preferential affinity enables PS to form a matrix. In contrast, this causes the PDMS block to organize into spherical dots. When TranSpin was spin-coated at 3000 rpm and baked at 195 °C for 90 seconds, an organic layer of <2 nm thickness was obtained. Ellipsometry measurements indicated the thickness of the planarizing layer to be ~1.7 nm. During solvent annealing, this thin organic layer enhances the chain mobility of the blocks by providing them with a softer platform. TranSpin also modifies the surface roughness of the magnetic media to a small extent and enables the study of self-assembly of PS-*b*-PDMS on a wider range of surfaces. More importantly, TranSpin eliminates any effects on self-assembly, apart from the surface roughness arising from the magnetic media underneath.

The topographies of the continuous and granular media samples were studied using SEM and AFM. Figure 7.3 and Table 7.2 show the root mean square roughnesses (i.e., R_{rms}) of different magnetic media exhibiting angstrom-scale variation. R_{rms} is the root mean square average of the height deviation from the mean image data plane. Another roughness parameter which has been considered is the peak-to-peak mean roughness depth (R_t). R_t is the average distance between the highest peak and lowest valley measured from the mean image data plane. It provides information regarding the coating quality of a material. From both R_{rms} and R_t values, it can be inferred that a more plateau surface was achieved after coating the media structures with TranSpin. The roughness data was extracted using Nanoscope Analysis software (supplied by Veeco Instruments). Statistical values were calculated according to the heights of the pixel in the image. The values of R_{rms} and R_t shown in Table 7.2 represent the mean and standard deviation from eight scans at different locations on the sample. Two different scan areas − 1 µm × 1 µm and 2 µm × 2 µm – were chosen. It is interesting to note that both the scan areas gave roughness parameters which were close to each other. That is, roughness measurements were not affected when the scan size was changed.

Magnetic media type/ Roughness parameters		**Continuous CoCrPt-SiO$_2$**		**Granular CoCrPt-SiO$_2$**		**Granular FePt-C-Cu**		**Granular FePt-C**		
		Without TranSpin	With TranSpin	Without TranSpin	With TranSpin	Without TranSpin	With TranSpin	Without TranSpin	With TranSpin	With TranSpin (5 layers)
Scan area: 2 µm x 2 µm	R_{rms}: Root mean square roughness (Å)	3.3±0.1	2.4±0.2	4.7±0.2	3.3±0.1	6.5±0.3	4.5±0.1	8.6±0.1	8.2±0.1	5.0±0.2
	R_t: peak-to-peak roughness (Å)	9.9±0.3	7.2±0.3	13.0±0.6	9.2±0.5	22.2±0.7	14.2±0.1	26.0±0.2	25.0±0.4	15.0±0.1
Scan area: 1 µm x 1 µm	R_{rms}: Root mean square roughness (Å)	3.2±0.3	2.4±0.2	4.7±0.3	3.2±0.1	6.5±0.4	4.3±0.3	8.9±0.3	8.2±0.2	5.0±0.2
	R_t: peak-to-peak roughness (Å)	9.6±0.4	7.2±0.5	13.0±0.7	9.3±0.6	22.5±0.6	13.1±0.2	26.0±0.3	26.0±0.5	15.0±0.2

Table 7.2 Roughness measurements on the magnetic media samples (unless otherwise stated; only one layer of TranSpin was coated).

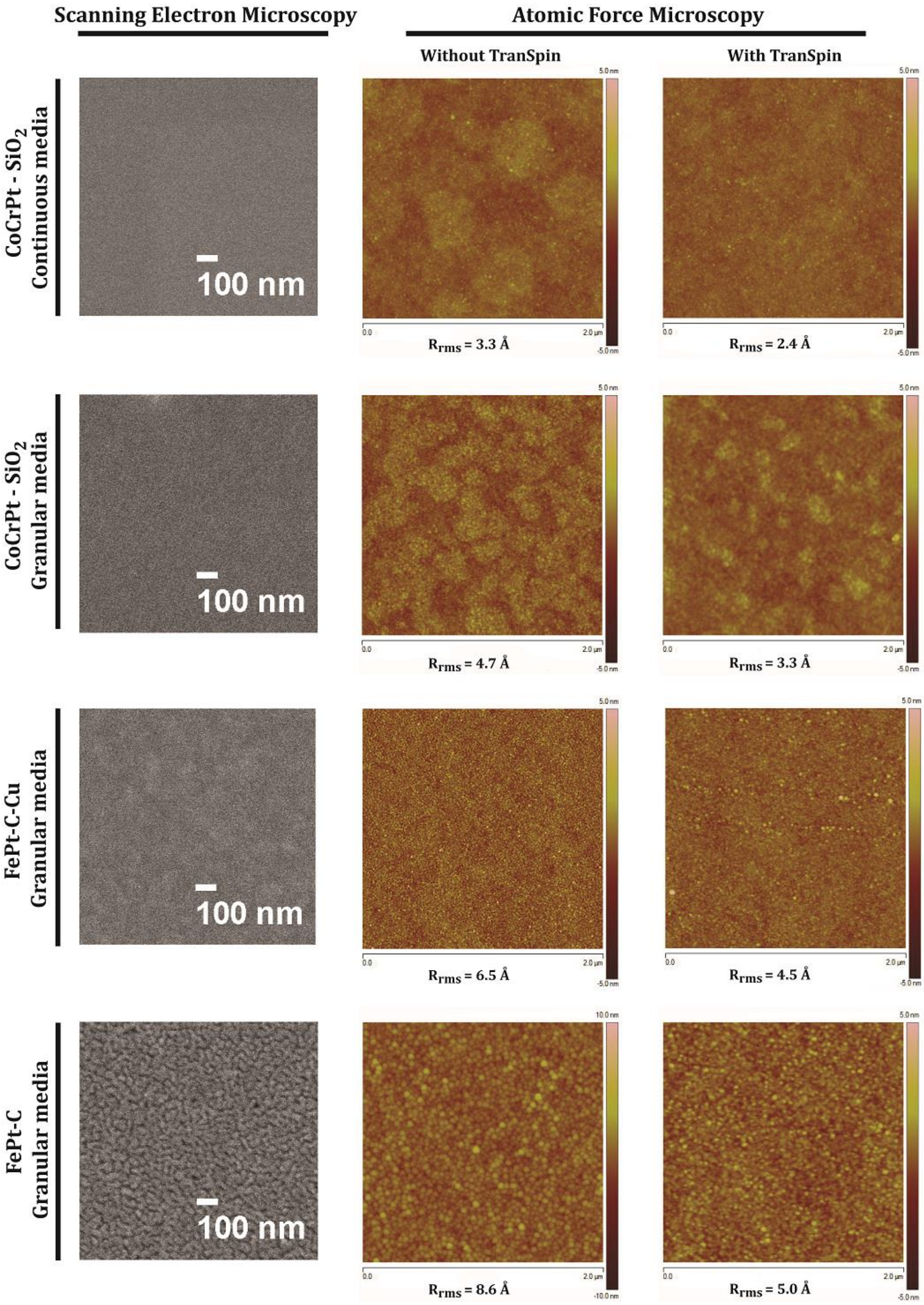

Figure 7.3 SEM and AFM images of the magnetic media with and without the TranSpin layer. The scan area is 2 × 2 µm^2. The vertical scale is from -5.0 to 5.0 nm. The surface roughness of granular FePt-C magnetic media is reduced to 8.2 Å (R_{rms}) when coated with a layer of TranSpin. The R_{rms} was further reduced to 5.0 Å when five layers of TranSpin were spin-coated on the granular FePt-C media.

7.3 Results: Effect of roughness on the self-assembly of PS-*b*-PDMS

The self-assembly of PS-*b*-PDMS was carried out on as-deposited samples as well as on samples coated with a layer of TranSpin. The results are shown in Figure 7.4. High resolution insets shown in Figure 7.4 were used to compute their corresponding fast Fourier transform (FFT) images [Figure 7.5] using ImageJ software. On continuous CoCrPt-SiO_2 media without any TranSpin underlayer (R_{rms}=3.3 Å), the dots did not appear to be well separated when solvent annealed in tetrahydrofuran (THF). This is because THF preferentially swelled PS more than PDMS, and therefore, the PDMS block did not have enough mobility to form dots. However, when the 6:1 toluene-heptane solvent mixture was employed for annealing, the self-assembly showed marginal improvement with some PDMS dot patterns exhibiting partial isolation from one another. On the other hand, spherical dots were clearly visible when self-assembly of PS-*b*-PDMS was carried out on the TranSpin-coated continuous media samples (R_{rms}=2.4 Å) and solvent annealed in THF and the 6:1 toluene-heptane mixture. Apart from reducing the surface roughness, the TranSpin layer also increased the chain mobility of the blocks, thereby enabling self-assembly. This is also evident as the first- and higher-order peaks in the corresponding FFT images became sharper [Figure 7.5].

On a slightly rougher granular CoCrPt-SiO_2 magnetic media (R_{rms}=4.7 Å), without the TranSpin underlayer, solvent annealing in THF barely showed the appearance of dots. However, on the TranSpin-coated samples (R_{rms}=3.3 Å), a marginal improvement in the self-assembly in the THF vapor was observed, possibly due to increased chain mobility. The existence of partial self-assembly was confirmed by the presence of first-order spots in the FFT image

[Figure 7.5]. Comparing the block copolymer self-assembly using THF vapor on the TranSpin-coated continuous and granular CoCrPt-SiO_2 magnetic media, it was seen that the latter's slightly higher roughness hindered phase separation of the individual blocks. When the 6:1 toluene-heptane mixture was used for solvent annealing, an excellent self-assembly was observed on the granular magnetic media [Figure 7.4]. Unsurprisingly, the FFT of the self-assembled dots showed sharp first- and higher-order spots. However, a slightly diffused halo around the first-order spots was observed in the case of TranSpin-coated granular CoCrPt-SiO_2 media, suggesting a minor degradation in self-assembly. The preferential swelling of PS by toluene and PDMS by heptane enabled the blocks to override the roughness barrier and, consequently, phase separate distinctly. In the TranSpin-coated continuous and granular media, cylinders along with the dots were observed when solvent annealed in the 6:1 toluene-heptane mixture. Heptane uptake by the PDMS block on continuous media increased its effective volume fraction, thus tending to change its morphology from spherical to in-plane cylinders, as suggested by the phase diagram [19].

The surface roughness rose to R_{rms}=6.5 Å when the magnetic media was changed to FePt-C-Cu. Self-assembly was *only* seen on the TranSpin-coated FePt-C-Cu substrate (R_{rms}=4.5 Å) when the block copolymer was solvent annealed in the 6:1 toluene-heptane mixture. However, the dots did not appear perfectly spherical as had been observed previously on the TranSpin-coated continuous and granular CoCrPt-SiO_2 media surfaces. Therefore, this can be viewed as a gradual deterioration of the self-assembly of PS-*b*-PDMS with increasing surface roughness [Figure 7.4]. This is reinforced by the fact that, unlike the continuous and granular CoCrPt-SiO_2 media surfaces, the FFT image of self-assembly on TranSpin-coated granular FePt-C-Cu showed first-order and extremely weak higher order spots. Solvent annealing of PS-*b*-PDMS on as-deposited and TranSpin-coated FePt-C-Cu employing THF vapor resulted in the formation of randomly oriented connected dots. A similar observation was also made when the block copolymer, spin-coated on the as-deposited sample, was annealed in the 6:1 toluene-heptane vapor. However, a few isolated dots were seen amongst the connected dots. This is most likely due to heptane providing the PDMS block with a slight increase in chain mobility to attempt to form dots.

The SEM images of self-assembly of PS-*b*-PDMS on as-deposited continuous CoCrPt-SiO_2 and granular FePt-C-Cu media samples showed the appearance of randomly connected dots when annealed in the THF vapor. The dots on continuous CoCrPt-SiO_2 media were on the verge of separating from one another. However, the PDMS block could not segregate completely into dots due to the lack of the required chain mobility, which has been shown to be provided by the use of the TranSpin layer. On the other hand, the dots on the FePt-C-Cu media tend to aggregate rather than move apart due to the higher surface roughness. Spinning a layer of TranSpin on the sample surface did not reduce the surface roughness significantly. Hence, the dots remained randomly connected. A similar observation was made for self-assembly on the *bare* samples employing the 6:1 toluene-heptane mixture. As R_{rms} was increased from 3.3 Å to 4.7 Å, the dots appeared fainter. However, when R_{rms} rose to 6.5 Å, randomly connected dots came into existence. It may be conjectured that the energy required by the PDMS block to surmount the energy barrier posed by the increased surface roughness was higher than the energy cost involved in remaining in an agglomerated form. This is supported by the FFT images of the self-assembly which show the presence of weak first-order spots, suggesting the absence of ordered dots [Figure 7.5].

The FePt-C film is the roughest among the four magnetic media prepared for this study [Figure 7.3]. The roughness arising from bare FePt-C media (R_{rms}=8.6 Å) was modified by applying one (R_{rms}=8.2 Å) and five layers of TranSpin (R_{rms}=5.0 Å). At R_{rms}=5.0 Å, there was no indication of self-assembly of PS-*b*-PDMS on FePt-C samples when annealed in the THF solvent vapor. In the case of the 6:1 toluene-heptane solvent system, the phase separation of the blocks appeared to be restricted by the high surface roughness of the media, resulting in an appearance of randomly connected dots. However, when the amount of heptane was increased two-fold in the solvent mixture, spherical dots were seen with a weak footing on the magnetic grains and they sparsely populated the sample [Figure 7.6]. This indicated that the swelling produced by heptane was not large enough to move over the roughness barrier of ~5.0 Å. On surfaces with R_{rms} > 5.0 Å, no self-assembly was observed and their topography appeared similar to that of the bare FePt-C surface [Figure 7.4]. The FFT image showed a diffused halo [Figure 7.5]. This observation can be attributed to the immobility of the PS-*b*-PDMS block copolymer, leading to its conformation onto such rough surfaces. The presence of the TranSpin layer seems to be ineffective in enabling the block copolymer to overcome the barrier posed by the surface roughness.

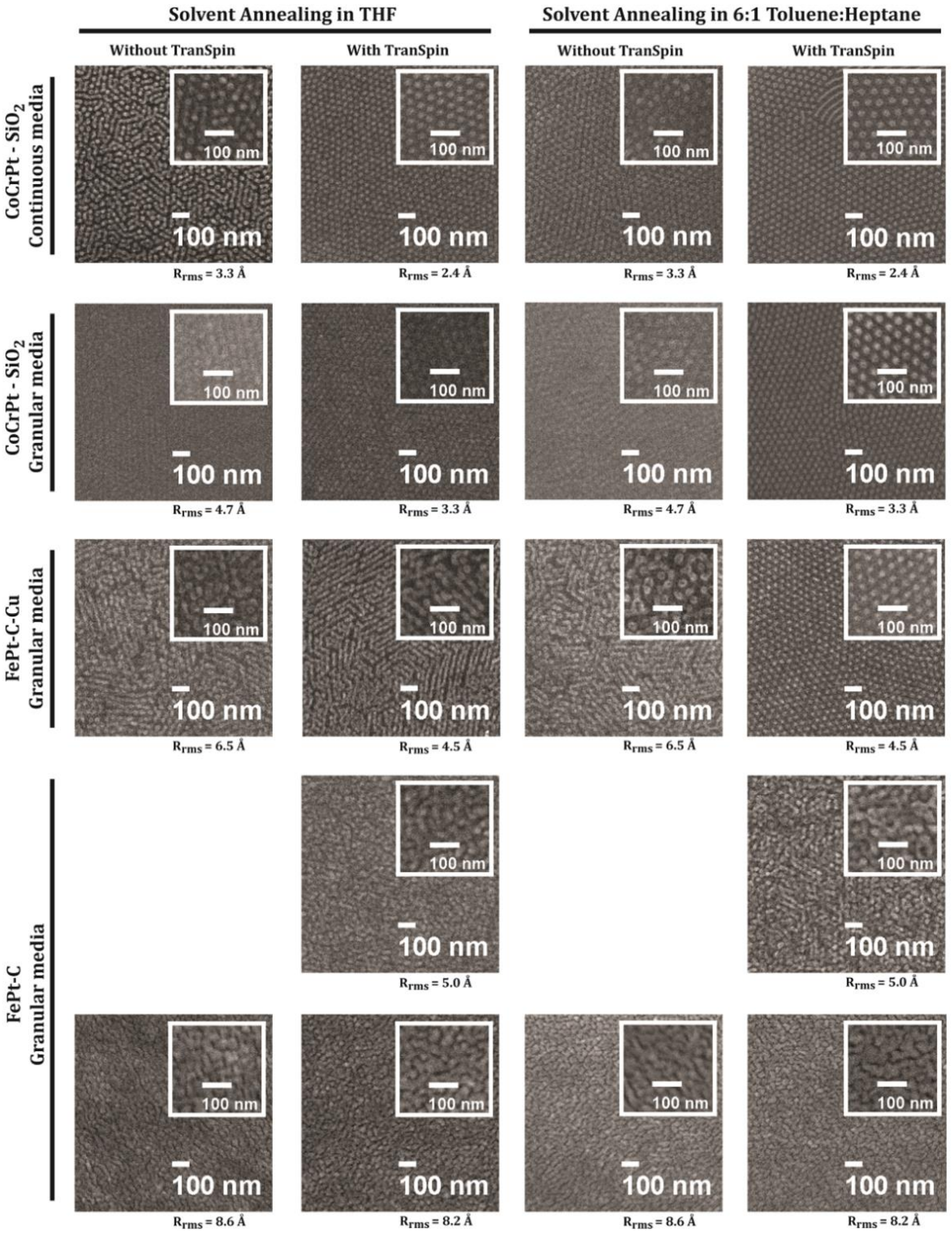

Figure 7.4 SEM images of the self-assembly of PS-*b*-PDMS on magnetic media with varying surface roughnesses and solvent annealed in THF and 6:1 toluene-heptane solvent systems. The roughness of FePt-C magnetic media was modified by spin-coating one (R_{rms} = 8.2 Å) and five layers of TranSpin (R_{rms} = 5.0 Å).

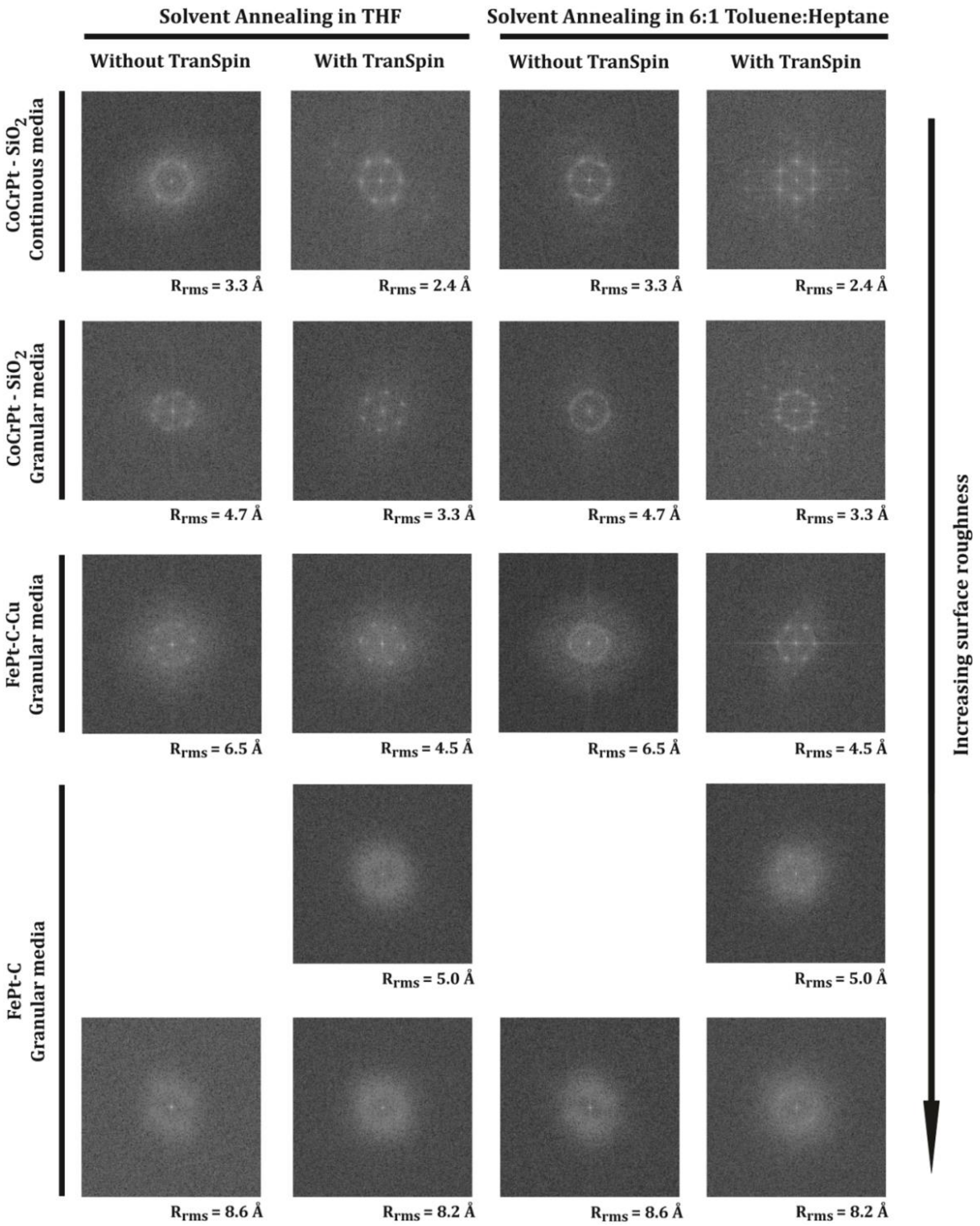

Figure 7.5 Fast-Fourier transform images of self-assembly of PS-b-PDMS on magnetic media with varying surface roughnesses and solvent annealed in THF and 6:1 toluene-heptane solvent systems. These images were computed from their corresponding high resolution insets shown in Figure 7.4.

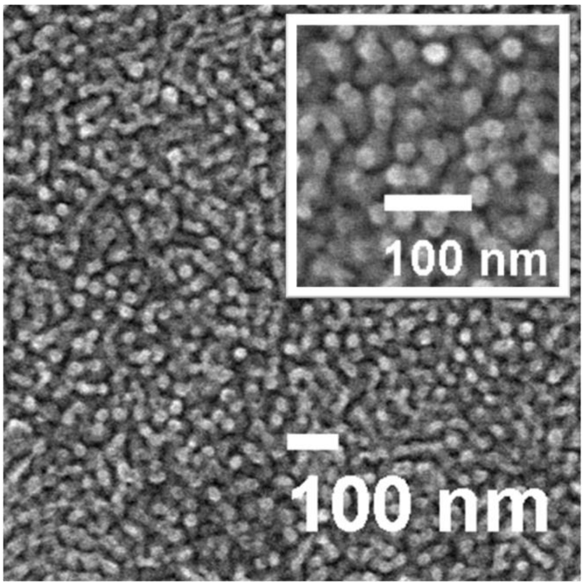

Figure 7.6 Self-assembly of PS-*b*-PDMS on FePt-C with surface roughness R_{rms}=5.0 Å, solvent annealed in 3:1 toluene-heptane mixture.

7.4 Discussion: Activation energy corresponding to the physical barrier hindering self-assembly

The self-assembly of PS-*b*-PDMS is kinetically hindered by surface roughness. Solvent annealing of the blocks is an effective way to swell them, improve their chain mobility and thus alleviate the impediment posed by surface roughness. When THF was employed for solvent annealing on the TranSpin-coated continuous CoCrPt-SiO_2 media, it preferentially swelled up the PS block. The PDMS block, in contrast, aggregated into spherical dots to avoid unfavorable interaction with THF. On the granular CoCrPt-SiO_2 media coated with TranSpin, the PDMS block lacked sufficient mobility to overcome the roughness-induced blockade and organize into dots. However, on switching the solvent annealing system from THF to the 6:1 toluene-heptane mixture, the PDMS block became mobile enough to self-assemble into dot patterns. PDMS is soluble in heptane and by deriving the required energy from the interaction with the latter, it was able to surmount the kinetic hindrance.

Faintly visible dots, as seen on the TranSpin-coated granular CoCrPt-SiO_2 media, disappeared on a slightly rougher FePt-C-Cu surface when the block copolymer was annealed in the THF vapor, and were replaced by the randomly connected dots. On the other hand, using the 6:1 toluene-heptane mixture for solvent annealing provided the blocks with a sufficient amount of energy to override the slight increase in roughness and self-assemble into dot-like features, albeit not perfectly spherical.

However, when R_{rms} reached close to 5.0 Å, the mobility of both the blocks was reduced even further, thus destroying self-assembly. Increasing the amount of heptane in the toluene-heptane mixture did not appear to improve the self-assembly on such rough surfaces. Therefore, the effectiveness of a solvent system to induce self-assembly of PS-*b*-PDMS is limited by surface roughness. The FFT images of self-assembly also showed a trend indicating the degradation of self-assembly with increasing surface roughness. The surface with least roughness showed sharp first- and higher-order spots. However, with increasing surface roughness, a diffused halo appeared around the first-order spots and the higher-order spots disappeared. When the $R_{rms} >$ 5.0 Å, only the diffused halo remained.

In a block copolymer, the chains are usually in the form of a collapsed globule. It has been suggested that solvent diffusion through the film creates a concentration gradient perpendicular to the film surface which enables the transition of the block copolymer film from a disordered to an ordered state from the substrate to the air surface [16, 17]. In our case, the block copolymer film closest to the bottom has to move over the surface roughness barrier first and undergo a transition to the ordered state. This transition is then propagated upwards throughout the entire film. However, if the surface roughness becomes insurmountable for the block copolymer film closest to the substrate surface during solvent annealing, the ordering is no longer observed. This results in the block copolymer conforming to the surface of the magnetic media.

Self-assembly is a process which exhibits a balance of the intermolecular forces between the homopolymer units and the chemical interaction of these units with the solvent system used for annealing. Qualitatively, the Gibbs free energy model is often used to describe the thermodynamics of self-assembly [21, 30]:

$$\mathbf{\Delta G_{SA} = \Delta H_{SA} - T\Delta S_{SA}} \qquad \text{Equation 7.1}$$

where $\mathbf{\Delta H_{SA}}$ is the enthalpy change taking place due to the intermolecular forces between the covalently bonded assembling units as well as their interaction with the solvent vapor causing the phase separation of the blocks. $\mathbf{\Delta S_{SA}}$ is the entropy change taking place in the system as the polymer units are arranged from a disordered to an ordered state, and is negative. Hence, to achieve self-assembly on a surface, the Gibbs free energy change, $\mathbf{\Delta G_{SA}}$, must be negative as the system goes from a disorder-to-order transition. Therefore, $\mathbf{\Delta H_{SA}}$ should be negative and in excess of the other counter-balancing term in the equation, i.e., $\mathbf{T\Delta S_{SA}}$ [30]. This free energy model for self-assembly assumes a *smooth ideal surface* and only involves the intermolecular interactions between the two blocks in a copolymer and solvent vapor.

However, when the self-assembly process with the same block copolymer and solvent system is carried out on surfaces with finite roughness values, the free energy model with the above parameters cannot explain the experimental observation of the gradual degradation of self-assembled structures with increasing roughness of the substrates. Therefore, we introduce a term $\mathbf{\Delta E_R}$ which represents the additional energy required by the polymer chains to diffuse over the corrugated surface. Taking into account the energy barrier posed by surface roughness, the modified Gibbs free energy model can be expressed as:

$$\mathbf{\Delta G_{SA*} = \Delta H_{SA*} - T\Delta S_{SA*}} \qquad \text{Equation 7.2}$$

where $\mathbf{\Delta H_{SA*} = \Delta H_{SA} + \Delta E_R}$

For self-assembly to be a spontaneous process on a substrate surface exhibiting roughness:

$$\mathbf{\Delta H_{SA*} > |-T\Delta S_{SA*}|}$$

$$\text{or } \mathbf{\Delta H_{SA} + \Delta E_R > |-T\Delta S_{SA*}|} \qquad \text{Equation 7.3}$$

In other words, $\mathbf{\Delta G_{SA*}}$ must be negative, suggesting that $\mathbf{\Delta H_{SA*}}$ is negative and exceeds the absolute value of the entropy term $\mathbf{T\Delta S_{SA*}}$. However, when the surface roughness exceeds a certain critical value, then $\mathbf{\Delta G_{SA*}}$ becomes positive, leading to the ceasing of self-assembly and the block copolymer conforming to the substrate surface.

The term $\mathbf{\Delta E_R}$ in Equation 7.2 can be expressed as the activation energy for the self-assembly process in the Van't Hoff-Arrhenius-Eyring equation as follows [31, 32]:

$$\mathbf{r = \vartheta_0 \exp\left(-\left|\frac{\Delta E_R}{RT}\right|^{n}\right)} \qquad \text{Equation 7.4}$$

where $\mathbf{r}$ is defined as the rate at which the blocks are phase separating to arrange into dots, $\boldsymbol{\vartheta_0}$ is the pre-exponential factor, $\mathbf{R}$ is the universal gas constant, $\mathbf{T}$ is the absolute temperature in Kelvin, and $\mathbf{n}$ is any integer.

$$\mathbf{ln}(\mathbf{r}) = \mathbf{ln}(\boldsymbol{\vartheta_0}) + \left(-\left|\frac{\Delta\mathbf{E_R}}{\mathbf{RT}}\right|^{\mathbf{n}}\right) \qquad \text{Equation 7.5}$$

Since $\boldsymbol{\vartheta_0}$, $\mathbf{R}$ and $\mathbf{T}$ all are constant and $\Delta\mathbf{E_R} \propto \mathbf{roughness}\ (\mathbf{R_{rms}})$, Equation 7.5 can be modified to:

$$\mathbf{ln}(\mathbf{r}) \propto (\mathbf{R_{rms}})^{\mathbf{n}} \qquad \text{Equation 7.6}$$

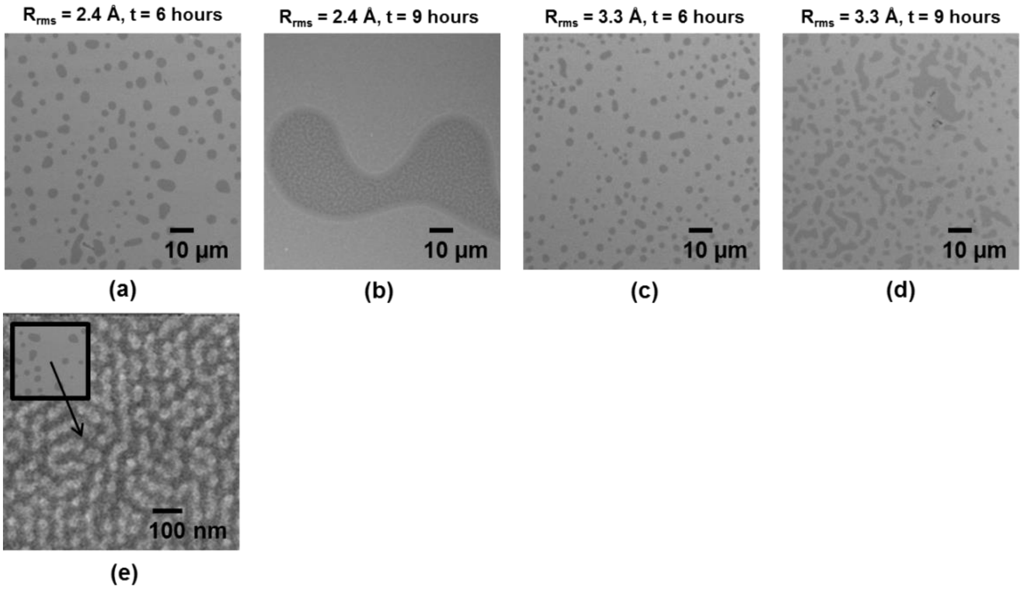

Figure 7.7 (a)-(d) Lower magnification images of the substrate surfaces with self-assembled patterns. Area scanned using ImageJ = 8000µm^2. (e) shows the higher magnification image of the lighter appearing regions. These regions consists of yet to be phase separated PDMS dots

In order to interpret the behavior of $\Delta\mathbf{E_R}$ with respect to $\mathbf{r}$, self-assembly of PS-*b*-PDMS on two surfaces of varying roughnesses (R_{rms} = 2.4 and 3.3 Å) in 6:1 toluene-heptane mixture were monitored over two different time durations (6 hours and 9 hours). Figure 7.7 shows low magnification images of the substrate surfaces after self-assembly. The darker appearing regions are covered with the self-assembled dots whereas the lighter appearing regions do not contain any self-assembled dots. These lighter appearing regions consist of oxidized PDMS which haven't undergone phase separation yet. They have been shown in a higher magnification image in Figure 7.7 (e). From the SEM images in Figure 7.4, it is evident that the size and pitch of the self-assembled dots did not vary for R_{rms} = 2.4 and 3.3 Å. In other words, the density of the dots did not change for these sets of samples. The area of the darker regions ($\mathbf{A}$) then became a direct estimation of the number of dots formed. ImageJ software was used for estimating the area covered by the dots on each of these substrate surfaces after six and nine hours, and the results are tabulated in Table 7.3. It can be seen from the values that the change in area coverage of the dots, $\Delta\mathbf{A}$, is faster with time on substrate surfaces with a lower roughness value (R_{rms} = 2.4 Å). The rate ($\mathbf{r}$) in this specific scenario is $\mathbf{\Delta A/\Delta t}$. Therefore, the change in $\mathbf{ln(r)}$ with increasing roughness is decreasing and is plotted in Figure 7.8. This indirectly indicates that the activation energy, $\mathbf{\Delta E_R}$, required to be surpassed by the blocks to diffuse and assemble into the desired morphology increases with increasing roughness. The behavior of $\mathbf{ln(r)}$ can be strongly Arrhenius (n=1, plotted in black line in Figure 7.8), super-Arrhenius (n >1, depicted in dotted blue line in Figure 7.8), and sub-Arrhenius (n <1, depicted in dotted red line in Figure 7.8) [33]. However, due to the degradation of self-assembly for R_{rms} > 3.3 Å and other complexities associated with self-assembly for higher time durations, more data points could not be collected and, thus, it was not possible to extrapolate the plot of $\mathbf{ln(r)}$ versus $\mathbf{R_{rms}}$ further. Nonetheless, understanding of roughness as an energy barrier could be recognized.

Substrate roughness (Å)	**Area covered by dots at t = 6 hours (μm^2)**	**Area covered by dots at t = 9 hours (μm^2)**	**ΔA (μm^2)**
2.4	1063	2890	1827
3.3	588	1183	595

Table 7.3 Change in area coverage of dots with varying roughnesses and time durations.

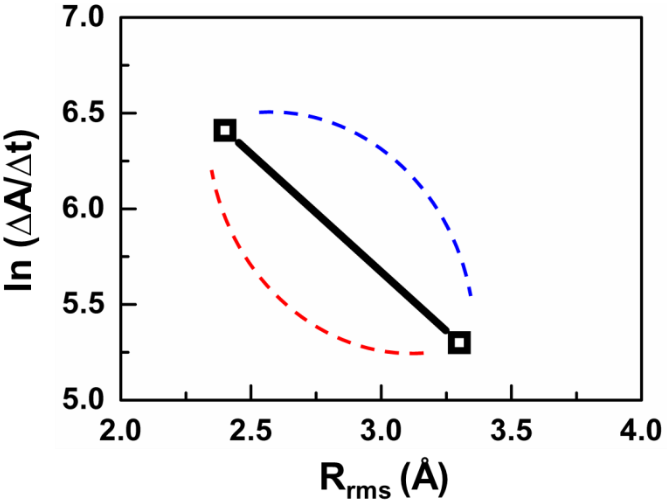

Figure 7.8 Arrhenius plot of $\mathbf{ln(r) = ln\left(\frac{\Delta A}{\Delta t}\right)}$ **versus** $\mathbf{R_{rms}}$ to map the behavior of the blocks with increasing roughness.

7.5 Summary, Inference and Scope of the Study

- To summarize, self-assembly of PS-*b*-PDMS using solvent annealing was studied on substrate surfaces with R_{rms} ranging from 2.4 Å to 8.6 Å. Phase separation employing THF was easily observed on the TranSpin-coated substrates exhibiting the least roughness (R_{rms}=2.4 Å). However, when the surface roughness of the TranSpin-coated substrate was increased to 3.3 Å, well-segregated dots could no longer be observed on the surface when annealed using THF. Here, the solvent was not able to provide the minor PDMS block sufficient energy to move over the rougher surface which kinetically hindered the formation of the dots. On the other hand, the 6:1 toluene-heptane solvent annealing system succeeded in providing self-assembly on the TranSpin coated-surfaces with roughness > 2.4 Å, but a slight deterioration in the shape of the dots was observed as the roughness was increased to 4.5 Å. For roughnesses above 5.0 Å, the 6:1 toluene-heptane solvent annealing system was ineffective in obtaining the desired spherical morphology. Therefore, the ability of a solvent system to swell individual blocks to overcome the surface roughness barrier reaches a limit when the roughness exceeds a certain critical value. At this point, self-assembly fails and the block copolymer conforms to the substrate surface. In addition, the necessity to use TranSpin on surfaces other than Si has been presented clearly. The polymer chains are provided with a softer platform for improved chain mobility leading to the phase separation.

- Block copolymers self-assemble in various morphologies on a substrate. Our study has shown that the surface roughness of a substrate plays an important role in governing the self-assembly. Just like the changes observed in spherical morphology of PS-*b*-PDMS with increasing roughness of the substrate, the in-plane cylindrical morphology can also be affected. However, the in-plane cylindrical structures face a consequence which is different from the spherical morphology when surface roughness of the substrate is increased [Figure 7.9].

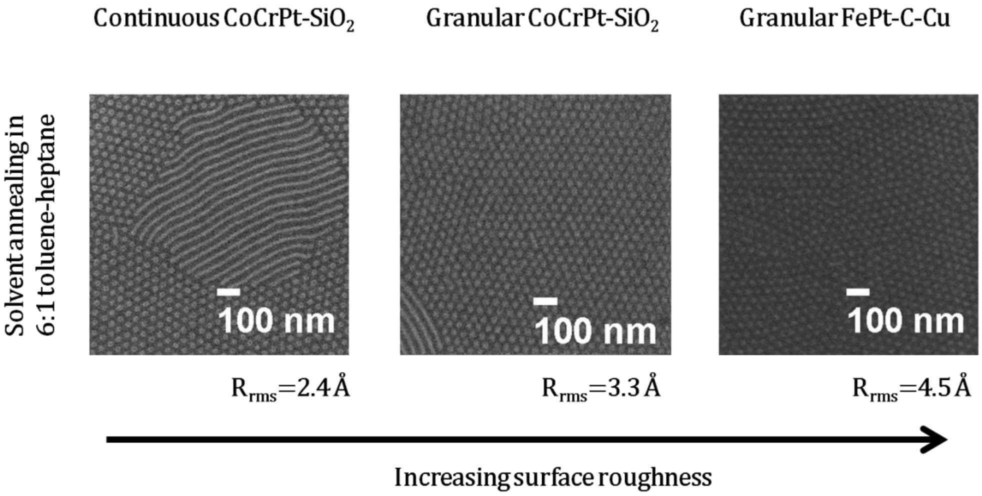

Figure 7.9 Effect of surface roughness on the in-plane cylindrical structures with increasing roughness. These structures are seen only when the 6:1 toluene-heptane mixture is used for solvent annealing.

It is known that the bulk morphology provided by the block copolymer system used in this study is spherical. However, heptane used in the solvent mixture caused the PDMS block to swell and increase its effective volume fraction. As a result, the bulk morphology changed from spherical to in-plane cylinders (from the block copolymer phase diagram) [19]. Dots and in-plane cylindrical structures were seen to co-exist together on a smoother surface, i.e., continuous CoCrPt-SiO$_2$ magnetic media. From Figure 7.9, it was observed that as the surface roughness increased, the in-plane cylindrical structures became less abundant. It can be surmised that as roughness rises, the increase in the effective volume fraction of the PDMS block by heptane may not be enough for it to assemble into in-plane cylinders.

- Nanofabrication by conventional techniques such as optical, electron and nanoimprint lithographies show good reliability and reproducibility [34]. The former two, due to the availability of good depth of focus and ability to pattern thick resists, are quite immune to the presence of surface roughness. On the other hand, nanoimprint lithography, especially using soft molds, can be used to imprint rough and uneven surfaces. Self-assembly, unlike conventional lithography methods, enables the creation of nanopatterns through physical movement of the polymer chains in a block copolymer. This study has shown that such a movement is sensitive to angstrom-scale surface roughness and its increase may result in the lowering of the reliability and reproducibility of self-assembly as a nanofabrication technique.

- The area covered by the assembled dots on the smoothest substrate (R_{rms}=2.4 Å) of dimensions 1 cm × 1 cm was estimated. Optical images of these substrates were analyzed using ImageJ software. Repeated measurements showed that area coverage by the dots as large as ~50% of the total substrate surface was possible when the block copolymer was annealed in 6:1 toluene-heptane mixture for nine hours. This suggests that self-assembly is a relatively faster and large area patterning technique with respect to its counterpart – high-resolution electron beam lithography. Nonetheless, a systematic investigation of the effect of surface roughness on self-assembly may be essential before it is employed as a reliable high density nanofabrication method. For example, in the case of BPM, ~20 nm features as obtained by self-assembly of the PS-*b*-PDMS block copolymer will provide an areal density of ~400 Gb/in^2 on a surface with R_{rms}<5 Å. To achieve areal densities of 1 Tb/in^2 and beyond in BPM, the bit size has to be shrunk to <12 nm. If self-assembly of block copolymers is employed to achieve such high areal densities and small bit sizes, we speculate that tighter control over the surface roughness of magnetic media will become necessary. Furthermore, it can now be seen that the implementation of $L1_0$ FePt in conjunction with self-assembly to create BPM for densities beyond 4 Tb/ in^2 (as proposed in Chapter 1) becomes a challenge.

References

[1] R. Ruiz *et al.*, Density multiplication and improved lithography by directed block copolymer assembly, Science, **321**, 936 (2008).

[2] I. Bita *et al.*, Graphoepitaxy of self-assembled block copolymers on two dimensional periodic patterned templates, Science **321**, 939-943, (2008).

[3] C. A. Ross *et al.*, Si containing block copolymers for self-assembled nanolithography, J. Vac. Sci. Technol. B, **26**, 2489 (2008).

[4] S. Park *et al.*, Macroscopic 10-terabit-per-square-inch arrays from block copolymers with lateral order, Science **323**, 1030 (2009).

[5] T. Hirai *et al.*, One-step direct-patterning template utilizing self-assembly of POSS-containing block copolymers, Adv. Mater. **21**, 4334 (2009).

[6] Y. S. Jung and C. A. Ross, Well-ordered thin-film nanopore arrays formed using a block-copolymer template, Small **5**, 1654–1659, (2009).

[7] Q. Wang *et al.*, A simple pathway to ordered silica nanopattern from self-assembling of block copolymer containing organic silicon block, Appl. Surf. Sci. **256**, 5843 (2010).

[8] Y. S. Jung and C. A. Ross, Orientation-controlled self-assembled nanolithography using a polystyrene-polydimethylsiloxane block copolymer, Nano Lett. **7**, 2046 (2007).

[9] V. P. Chuang, J. Gwyther, A. R. Mickiewicz, I. Manners, and C. A. Ross, Templated self-assembly of square symmetry arrays from an ABC triblock terpolymer, Nano Lett. **9**, 4364 (2009).

[10] B. C. Stipe *et al.*, Magnetic recording at 1.5 Pb m^{-2} using an integrated plasmonic antenna, Nature Photon. **4**, 484 (2010).

[11] O. Hellwig *et al.*, Bit patterned media based on block copolymer directed assembly with narrow magnetic switching field distribution, Appl. Phys. Lett. **96**, 052511 (2010).

[12] K. O. Stuen *et al.*, Graphoepitaxial assembly of asymmetric ternary blends of block copolymers and homopolymers, Nanotechnology, **21**, 495301 (2010).

[13] T. Hashimoto, J. Bodycomb, Y. Funaki, and K. Kimishima, The effect of temperature gradient on the microdomain orientation of diblock copolymers undergoing an order−disorder transition, Macromolecules, **32**, 952 (1999).

[14] P. Mansky *et al*., Large-area domain alignment in block copolymer thin films using electric fields, Macromolecules, **31**, 4399 (1998).

[15] Z. R. Chen, J. A. Kornfield, S. D. Smith, J. T. Grothaus, and M. M. Satowski, Pathways to macroscale order in nanostructured block copolymers. Science, **277**, 1248 (1997).

[16] Z. Lin *et al*., A rapid route to arrays of nanostructures in thin films. Adv. Mater. **14**, 1373 (2002).

[17] S. H. Kim, M. J. Misner, and T. P. Russell, Solvent-induced ordering in thin film diblock copolymer/homopolymer mixtures, Adv. Mater.**16**, 2119 (2004).

[18] J. Peng, Y. Han, W. Knoll, and D. H. Kim, Development of nanodomain and fractal morphologies in solvent annealed block copolymer thin films, Macromol. Rapid Commun. **28**, 1422 (2007).

[19] J. K. Bosworth *et al*., Control of self-assembly of lithographically patternable block copolymer films. ACS Nano, **2**, 1396 (2008).

[20] A. Knoll, R. Magerle, and G. Krausch, Phase behavior in thin films of cylinder-forming ABA block copolymers: Experiments, J. Chem. Phys. **120**, 1105 (2004).

[21] Y. S. Jung and C. A. Ross, Solvent-vapor-induced tunability of self-assembled block copolymer patterns, Adv. Mater. **21**, 2540 (2009).

[22] Y. Hirayama, I. Tamai, I. Takekuma, and R. Nakatani, Role of underlayer for segregated structure formation of CoCrPt-SiO_2 granular thin film, J. Phys.: Conf. Ser. **165**, 012033 (2009).

[23] R. Fernandez, N. Amos, C. Zhang, B. Lee, and S. Khizroev, Optimization of $L1_0$-FePt/MgO/CrRu thin films for next-generation magnetic recording media, Thin Solid Films, **519**, 8053 (2011).

[24] J. Z. Shi, S. Piramanayagam, C. S. Mah, and J. M. Zhao, Influence of gas pressures on the magnetic properties and recording performance of CoCrPt–SiO_2 perpendicular media, J. Magn. Magn. Mater. **303**, e145 (2006).

[25] Y. K. Takahashi, M. Ohnuma, and K. Hono, Ordering process of sputtered FePt films, J. Appl. Phys. **93**, 7580 (2003).

[26] J. A. Bandrup, E. H. Immergut, and E. A. Grulerke, *Polymer Handbook, 4th edition*, John Wiley & Sons (2005).

[27] X. Yang, Y. Xu, C. Seiler, L. Wan, and S. Xiao, Toward 1 Tdot/in.^{2} nanoimprint lithography for magnetic bit-patterned media: Opportunities and challenges, J. Vac. Sci. Technol. B, **26**, 2604 (2008).

[28] S. M. Park *et al.*, Sub-10 nm nanofabrication via nanoimprint directed self-assembly of block copolymers, ACS Nano, **5**, 8523 (2011).

[29] V-M. Graubner *et al.* Wettability and surface composition of poly(dimethylsiloxane) irradiated at 172 nm, Polym. Mater. Sci. Eng. **88**, 488 (2003).

[30] R. A. Farrell, T. G. Fitzgerald, D. Borah, J. D. Holmes, and M. A. Morris, Chemical interactions and their role in the microphase separation of block copolymer thin films, Int. J. Mol. Sci. **10**, 3671 (2009).

[31] S. Yokotsuka, Y. Okada, Y. Tojo, T. Sasaki, and M. Yamamoto, Activation energy of local polymer motions estimated from fluorescence depolarization measurements, Polym. J. **23**, 95 (1991).

[32] H. Eyring, Viscosity, plasticity, and diffusion as examples of absolute reaction rates, J. Chem. Phys. 4, 283 (1936).

[33] M. K. Chaudhurya and P. S. Goohpattader, Activated drops: Self-excited oscillation, critical speeding and noisy transport, Eur. Phys. J. E, **36**, 13015-2 (2013).

[34] R. F. Pease and S. Y. Chou, Lithography and other patterning techniques for future electronics, Proc. IEEE, **96**, 248 (2008).

CHAPTER 8

Conclusions and Future Work

8.1 Conclusion

Various aspects of high anisotropy $L1_0$ FePt media have been studied for application in advanced recording schemes such as heat-assisted magnetic recording (HAMR) and bit patterned media recording (BPMR) to achieve ultra-high areal densities >1 Tb/in^2 in hard disk drives (HDD).

For application in HAMR: Well-isolated, smaller sized FePt grains and high out-of-plane coercivities >20 kOe with least in-plane variants, all simultaneously, were achieved in this work. Ternary elements, which degrade the chemical ordering of the $L1_0$ phase FePt, were not used to obtain smaller grain sizes. Instead, the sputtering gas was merely changed from Ar to Ar–He. As a result, out-of-plane coercivity increased from 15 to 22 kOe and the grain dimensions reduced by twofold. The excited metastable helium species generated in the plasma modified the ion current density. Surplus Ar^+ ions, apart from those created through electron-impact ionization, were produced through Penning ionization of argon by helium. These Ar^+ ions imparted additional energy to the target Fe and Pt atoms. Therefore, helium is seen to play a pivotal role in providing the Fe and Pt atoms with optimal adatom mobility to produce well-ordered $L1_0$ FePt media. By fine-tuning the helium content in the sputtering gas mixture, grain diameters approaching the sub-5 nm range could be achieved in the future.

For usage in BPMR: Low energy embedment of C^+ ions was carried out to induce an order-disorder transformation in the *L1₀* phase FePt media. The out-of-plane coercivity of the 10 nm thick FePt film declined from 14 to 2 kOe when it was bombarded with C^+ ions at 350 eV (pulse bias). The embedded C^+ ions were supposed to be restricted to the top few nanometers (~2 nm) of the FePt film. However, elemental analysis indicated a penetration of >2 nm by several of the C^+ ions into the FePt film (channeling effect). Two phenomena − smaller diameter of the C^+ ions with respect to the lattice constant (*a*-axis) of $L1_0$ FePt and the parallel alignment of the direction of motion of the former with the crystallographic axis of the latter − caused the channeling of the ions throughout the entire depth of the FePt layer. These C^+ traversing ions created recoil host atoms and therefore were responsible for multiple collision-induced damage cascades.

This idea of inducing structural disorder in the FePt layer at energy values <1 keV was employed to create and study $L1_0$ FePt-based BPM. The advantage of low energy ion embedment over high energy ion implantation is reduced lateral straggle of the ions. $L1_0$ FePt-based BPM with an areal density of 1.6 Tb/in^2 (bit diameter ~10 nm, pitch ~20 nm) was fabricated. After embedment, the patterned FePt media comprised of a matrix of alternate $L1_0$ phase ordered (bit) and fcc disordered (spacing between the bits). However, the out-of-plane coercivity of the patterned FePt media (~4.5-5.5 kOe) was less than the coercivity of the reference sample (~10 kOe). The higher concentration of the incoming ions nearer to the FePt film surface led to a larger lateral straggle in the top few nanometers of the FePt film than at the bottom. As a result, a low anisotropy region followed by a relatively high anisotropy region was detected in the FePt ‘bit’. This led to switching of the bit at reduced field values.

Apart from magnetic and structural studies on *L1₀* FePt media, an investigation on its surface roughness was also carried out in this thesis. Due to the high deposition temperature, grain growth is very common in *L1₀* FePt films. This causes the films to exhibit high root mean square surface roughness (R_{rms}) of ~1 nm. Large area self-assembly on FePt surfaces is ideal for creating high throughput and high density BPM. However, a systematic study of the self-assembly of polystyrene-*b*-polydimethylsiloxane (PS-*b*-PDMS) on media surfaces with roughness varying on an angstrom scale revealed that self-assembly ceases when R_{rms} is ≥5.0 Å (critical surface roughness limit). The kinetic hindrance posed by the surface roughness of the magnetic media on the block copolymer led to its conforming to the surface without observable phase separation.

8.2 Future Work

Extending the study on FePt patterned media: Although *L1₀* FePt-based BPM was fabricated and studied, further investigation is required to address the bottlenecks stated in Chapter 6.

- In this thesis, lateral straggle and the associated cascade damage have been quantified using simulation. However, it is necessary to observe lateral straggle of the C^+ ions experimentally. This can be done using careful preparation of a patterned FePt sample for transmission electron microscopy (TEM). This sample can then be subjected to an elemental line scan using electron energy loss spectroscopy (EELS) equipped in the TEM to map the lateral straggle across the patterned FePt film.

- The coercivity of the bare $L1_0$ FePt film was reduced to a ~0.2 kOe when embedment of the C^+ ions was carried out at 100 eV. Also, the saturation magnetization of the embedded bare FePt film is 200 emu/cc, much lower than patterned (400 emu/cc) and reference FePt films (800 emu/cc). Therefore, this energy value is a viable option for creating patterned media. Nonetheless, no lower energy limit was estimated in this work below which the disordered region is not created between the two fct-ordered FePt bits. This is crucial and needs to be studied in order to have control over the lateral straggle of the embedding ions.

- A thorough investigation is necessary for studying the effect of varying fluences/doses of the embedding ions on the magnetic and structural properties of the FePt films at lower ion bombardment energies. This study could not be performed in this thesis due to the limitation of the equipment used for carrying out embedment of the C^+ ions.

- Apart from the C^+ ions, additional ions with diameters less than the lattice constant of the $L1_0$ FePt film and can, therefore, undergo channeling, such as N^+ ions, are worthwhile to be studied. With atomic mass greater than that of C, the ions will induce less lateral straggle. Table 8.1 shows the comparison of the simulated lateral straggle obtained in the FePt films when N^+ and C^+ ions were used for embedment. Figure 8.1 shows the embedment profiles of the N^+ ions at 100 and 500 eV.

Embedding species	Lateral straggle at 100 eV (nm)	Lateral straggle at 500 eV (nm)
Carbon	0.7	1.5
Nitrogen	0.6	1.3

Table 8.1 TRIM simulated lateral straggle values of the C^+ and N^+ ions in the FePt films when embedment was carried out at 100 and 500 eV.

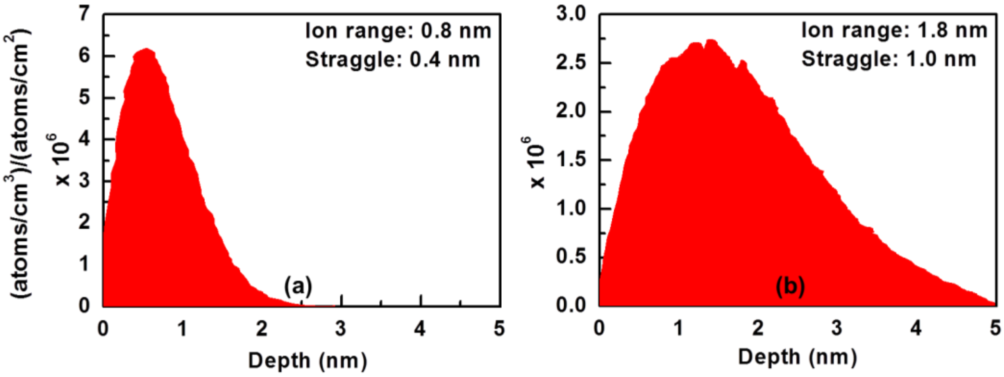

Figure 8.1 TRIM simulated embedment profiles of N^+ ions at energies (a) 100 eV and (b) 500 eV.

In short, this study on low energy ion embedment has provided an avenue to investigate the effect of different ions, combination of ions, fluences and energies on FePt to create BPM of the future.

Self-assembly studies of lower molecular weight block copolymers: The PS-*b*-PDMS block copolymer used in this study had a molecular weight of 51 kg/mol. At this molecular weight, the diameter of the self-assembled dots was ~20 nm. The pitch achieved was ~40 nm. Therefore, with this block copolymer, an areal density of 400 Gb/in^2 could be achieved. However, for implementing self-assembly in BPM at areal densities >1 Tb/in^2, the self-assembly of PS-*b*-PDMS block copolymers of lower molecular weights should be studied on surfaces with roughness varying on an angstrom scale. It can be speculated that the critical limit of surface roughness for achieving self-assembly with block copolymers having molecular weights <51 kg/mol would be <5.0 Å (R_{rms}).

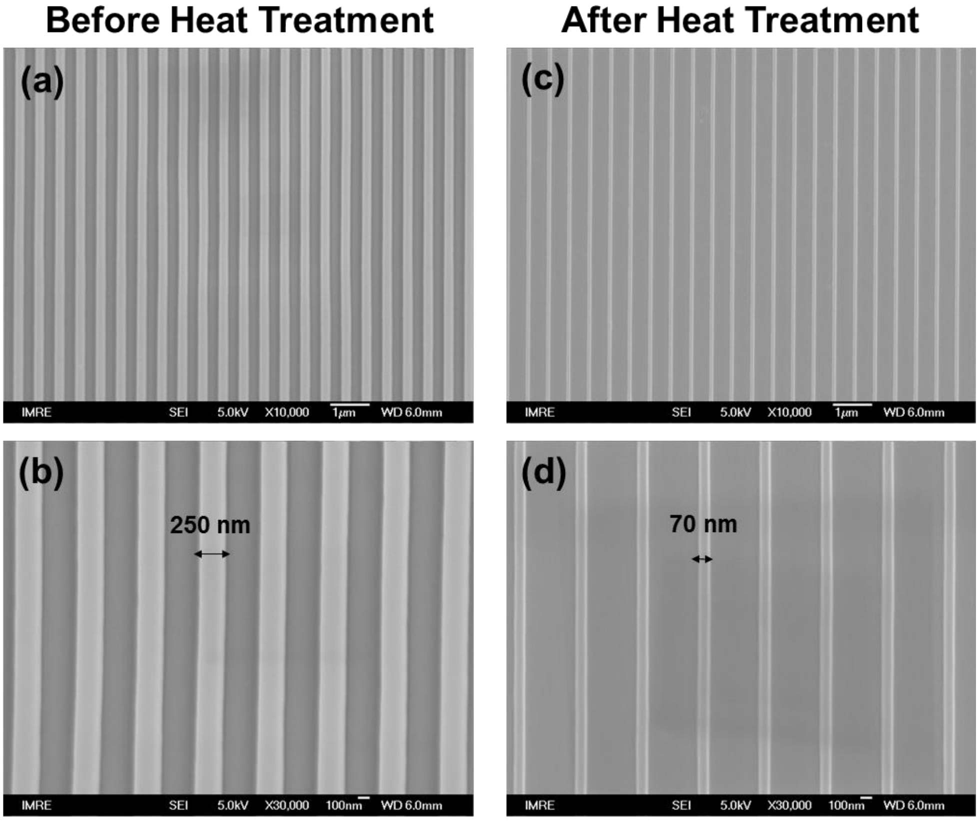

Figure 8.2 Low and high magnification SEM images of the imprinted 250 nm line/space features (a, b) before and (c, d) after heat treatment.

Guided self-assembly: Topographical patterns like arrays of circular posts and parallel lines on top of the magnetic material can be used to guide the self-assembly of the block copolymer. A combination of advantages of both self-assembly and nanoimprint lithography (NIL) may open the door for achievement of long range radial order in BPM. A silicon-based resin can be imprinted using a silicon mold with 250 nm line/space features (aspect ratio 1:1) on the media surface. Finer feature dimensions are required to dictate the periodicity of the domains over a large area on the magnetic media. Therefore, heat treatment of these imprinted structures is carried out to produce shrinkage of the resist to form SiO_2 lines with dimensions in the sub-100 nm range. The feature size is reduced to ~70 nm (aspect ratio of 1:1 being maintained). Smaller-sized features can be achieved from larger master molds without the loss of any pattern integrity. There are many bottlenecks associated with other lithography tools used for designing topographical patterns for guided self-assembly, such as optical diffraction limit in UV lithography, slow rastering and secondary electron exposure in electron beam lithography (EBL), ion scattering in a focused in beam scanning (FIB) process, and proximity issues in x-ray interference lithography. These can be circumvented using NIL. Figure 8.2 shows the preliminary results obtained in this study. More importantly, this approach promises high throughput large area assembly of block copolymers on media surfaces.